THE DEVELOPMENT AND CHARACTERIZATION OF A SURFACE ENHANCED RAMAN SPECTROSCOPY BIOSENSOR UTILIZING AN OLIGONUCLEOTIDE

A Dissertation

by

BRIAN M. WALTON

Submitted to the Office of Graduate and Professional Studies of
Texas A&M University
in partial fulfillment of the requirements for the degree of

DOCTOR OF PHILOSOPHY

Chair of Committee,	Gerard L. Cote
Committee Members,	Kristen Maitland
	Mike McShane
	Jun Kameoka
Head of Department,	Anthony Guiseppi-Elie

August 2017

Major Subject: Biomedical Engineering

ABSTRACT

Citrulline has shown potential as a biomarker. It can be used for a number of clinical applications including diagnosis in the clinic, as a research tool, to accurately indicate the amount of radiation absorbed by the body, and as a point of care device. In particular, for this last application, rapid assessment of radiation exposure is critically important at the point-of-care (POC) for the proper triage and treatment of large populations exposed to ionizing radiation. Currently, to quantify the amount of citrulline in the body, a blood sample must be sent to a central lab where it is analyzed using bulky and expensive instruments, such as high-performance liquid chromatography (HPLC) or liquid chromatography/mass spectrometry (LC/MS) and liquid chromatography-tandem mass spectrometry (LC/MS/MS). This process is very time consuming and prolongs the time until effective treatment can be administered. Therefore, a point-of-care surface enhanced Raman spectroscopy (SERS) biosensor was proposed to address the problems mentioned above and quantitatively detect citrulline. SERS is a method that uses a metallic surface or nanoparticle metal colloids to enhance the inelastic Raman scattering of photons. By providing vibrational energy information about molecules adsorbed to the metal surface, including nanoparticles, SERS can be used for trace analysis due to the substantial enhancement factor from the metallic substrate. SERS has the ability to analyze molecules in the micro- to nanomolar concentration range with some reports reaching picomolar levels in solution. SERS also has the potential for multiplexing

multiple biomarkers because of their narrow spectral line widths, making such labels a promising analytical approach for biosensing.

Moving towards a POC sensor for citrulline detection, four types of Raman reporter functionalized nanoparticles in a micro-to-nanochannel were characterized in this work. Further, a non-aggregating binding chemistry was created and characterized on silver (Ag) nanocubes for citrulline detection. Lastly, two citrulline SERS sensors were developed. The first sensor used a competitive binding approach and the second sensor used Ag nanocubes functionalized with citrulline aptamers. These sensors were then analyzed to test the feasibility of a future, quantitative, POC SERS biosensor.

DEDICATION

For my wife, my mother and father, sisters and brother, nieces and nephews, aunt, my family, my friends and our future generations. Without your constant support and motivation this wouldn't have been possible.

ACKNOWLEDGEMENTS

I would like to thank my committee chair, Dr. Gerard Cote; the guidance I received from him has impacted me personally and professionally, and I am forever indebted to him. I also extend gratitude to my committee members, Dr. Kristen Maitland, Dr. Michael McShane, Dr. Jun Kameoka, and Dr. Michael Pishko, for their guidance and support throughout the course of this research. Also, I would like to acknowledge, Maria Lyons and Barbara Slusher in the Texas A&M BMEN Department for their help and always happy disposition.

I would like to thank my wife, Kym who loved me unconditionally through this difficult journey. The stability she gave me during these years kept me from quitting and her beautiful soul gave me something to look forward to on a daily basis. I also thank my mother and father, Dr. Phillip Walton, Sr. D.D.S and Mrs. Phyllis Walton for instilling in me a belief that obtaining an education is nonnegotiable; I was only able to finish this accomplishment by standing on the solid foundation they provided. To my sisters and brother, Dr. Taisha Okafor M.D, Mrs. Soumayah Davis and Dr. Phillip Walton Jr. M.D, I can't put into words how much you mean to me. It's truly an honor to be your baby brother - also thanks for giving me my nieces and nephews! Kenechi, Cheluchi, Ethan and Zahara, my nieces and nephews, the love you've shown me has helped to keep me going during the tough times. Also, I extend gratitude to my Aunt, Mrs. Geraldine Carver, for being an inspiration to me as the first scientist I knew and for always being present in my life.

Sadly, I don't have enough space to adequately thank the following people, but I must mention them in no particular order because their presence in my life made an enormous impact. My family members, Uncle Kenneth, Keisha, Suzanne, Aunt Bessie, Aunt Eddie, Aunt Evelyn, my cousins, and those relatives who have passed on.

I need to also thank the people who treated me like family and helped me greatly. Dr. and Mrs. Arvid Mukes, Dr. Domonic Bearfield, Chad and Denise Spears, Dr. Galen Newman, Edward Tarlton, Coach William "Buck" Godfrey, Harris Hall, Calvin Leaks, Opal Nixon, Col. Dr. Adrian Wilson, Col. and Mrs. Kenneth Dollar, and Carl and Brenda Neely. The teachers at Fernbank Elementary, Shamrock Middle School, Southwest DeKalb High School, and Florida A&M University, especially the Physics professors.

I also express thanks to my close friends Anthony Alexander, Christopher Neely, Dr. Eric O'Rear, Gregory Woodall, and Kevin Robinson. I am also thankful for my fraternity Alpha Phi Alpha, the Pi Alpha Lambda chapter, and especially my line brothers Herbert Pierre and Jason Mathis.

I would also like to thank the children and possibly future scientists who took interest in biomedical engineering and encouraged me in their own way, Samantha, Audrey, Chris Jr., Aiden, Austin, and Ashton.

I would also like to acknowledge myself, in the hopes that I never forget what happens when I don't quit! I will walk across the stage as the first African-American male to earn a Ph.D. in Biomedical Engineering at TAMU.

Finally, to all the nameless people who fought and died over the years for an African-American male to have the right to attend this University…thank you!

CONTRIBUTORS AND FUNDING SOURCES

This work was supervised by a dissertation committee consisting of Professor Gerard L. Cote (Advisor), Professors Kristen Maitland and Mike McShane of the Department of Biomedical Engineering and Professor Jun Kameoka of the Department of Electrical and Computer Engineering.

The Micro-to-nanochannels provided in Chapter 2 that were used to analyze the various nanoparticles were provided by Po-Jung Huang under the guidance of Professor Jun Kameoka and was published in 2015. The citrulline aptamers used in Chapter 3 were provided by Dr. George W. Jackson of Basepair Biotechnologies. Guidance was also given from Dr. Nicolaas Duetz for the amino acid citrulline in Chapter 3. Help with the assay development in Chapter 4 was provided by Dr. Andrea Locke. All other work conducted for the dissertation was completed by the student independently.

Funding Sources

This work was made possible in part by the Alfred P. Sloan Foundation Graduate Student Fellowship, Texas A&M University Diversity Fellowship, the National Institute of Environmental Health Sciences (NIEHS) under Award no(s). 2R44ES022303 and P30ES023512; Funder ID can be found at http://dx.doi.org/10.13039/100000066. The contents herein are solely the responsibility of the author and do not necessarily represent the official views of the National Institute of Environmental Health Sciences (NIEHS).

NOMENCLATURE

AC	Alternating Current
Ag	Silver
Au	Gold
BDT	Benzenedithiol
BOE	Buffer of Etchant
CD	Celiac Disease
Cu	Copper
DCA	Dicentric Chromosome Assay
DI	Deionized
DNA	Deoxyribonucleic Acid
FTIR	Fourier Transform Infrared Spectrometry
H_3PO_4	Hot Phosphoric Acid
$HAuCl_4$	Chloroauric Acid
HEPES	4-(2-Hydroxyethyl)-1-Piperazineethanesulfonic Acid
HPLC	High Performance Liquid Chromatography
IR	Ionized Radiation
LC-MS	Liquid Chromatography-Mass Spectrometry
LC-MS/MS	Liquid Chromatography-Tandem Mass Spectroscopy
MBA	Mercaptobenzoic Acid
$MgCl_2$	Magnesium Chloride

MST	Microscale Thermophoresis
NaCl	Sodium Chloride
NaOH	Sodium Hydroxide
NHS	N-hydroxysuccinimide
NIR	Nonionized Radiation
NTA	Nanoparticle Tracking Analysis
PBS	Phosphate-Buffered Saline
PECVD	Plasma-Enhanced Chemical Vapor Deposition
PEG	Polyethylene glycol
pH	Potential of hydrogen
POC	Point of Care
PVP	Polyvinylprrolidone
RNA	Ribonucleic Acid
RRM	Raman Reporter Molecules
SELEX	Systematic Evolution of Ligands by Exponential Enrichment
SEM	Scanning Electronic Microscope
SERS	Surface Enhanced Raman Spectroscopy
Si_3N_4	Silicon Nitride
TEM	Transmission Electronic Microscope
UV	Ultraviolet
VIS	Visible

TABLE OF CONTENTS

Page

LIST OF FIGURES

Page

LIST OF TABLES

Page

LIST OF EQUATIONS

Page

CHAPTER I

INTRODUCTION AND LITERATURE REVIEW[1] [2]

This introduction is divided into three sections. The first section discusses the application areas for detection of citrulline with a focus on the point of care (POC) application of ionized radiation detection. In section 2, citrulline and the citrulline aptamer assay are introduced. Lastly, surface enhanced Raman spectroscopy (SERS), as a detection methodology, is discussed.

I.1. Application areas for citrulline

Celiac disease (CD) is one of three application areas worth mentioning with respect to citrulline because the nature of the disease affects the plasma citrulline levels. Celiac disease is an autoimmune disease that predominantly affects the small intestine. Individuals with CD usually have gastrointestinal complications, including abdominal distention, chronic diarrhea, and loss of appetite. CD is caused by a reaction to gluten causing inflammation amongst other problems in the intestines which, in turn, affects the production of citrulline. Individuals with CD have lower plasma citrulline levels.(1)

Viral enteritis is another application area of interest due to its effect of citrulline production. Viral enteritis is an inflammation of the small intestine caused by food or

---

[1]Reprinted with permission from "Use of a micro-to nanochannel for the characterization of surface-enhanced Raman spectroscopy signals from unique functionalized nanoparticles" by Brian M. Walton et. al., 2016. Vol. 9715, Copyright 2016. Society of Photo Optical Instrumentation Engineers.

[2]Reprinted with permission from "Comparing Surface Enhanced Raman Spectroscopy from Colloidal Gold Nanoparticles and Nanocages" by B. M. Walton and G.L. Cote, 2015. Vol. 9332, Copyright 2015. Optical Diagnostics and Sensing XV: Toward Point-of-Care Diagnostics.

drinks containing pathogens like salmonella or norovirus. Symptoms of enteritis can include dehydration, cramping, and abdominal pain. Due to the effect that these viruses can have on the enterocytes they can cause reduction in the production of plasma citrulline.(2)

Lastly, the major cause of intestinal graft failure is acute cellular rejection after small bowel transplantations. Small bowel transplantation has been used to help treat individuals with short bowel syndrome or irreversible intestinal failure. If not diagnosed and treated early, acute cellular rejection can lead to sepsis, graft failure, and/or death. Citrulline has been shown as an early marker of rejection for moderate to severe intestinal graft failure by monitoring the reduced production of the amino acid in plasma.(3)

In terms of using citrulline as a biomarker in a POC device, our primary application was rapid assessment of radiation exposure, which is critically important to the proper triage and treatment of large populations exposed to ionizing radiation. Radiation is considered ionizing when energy from radiation is strong enough to remove the electron from its orbit in an atom; when this happens, chemical bonds are changed and permanently damaged. Ionized radiation (IR) stems from any atom that is unstable from the protons and neutrons within the nucleus binding. When there are not enough or there are too many neutrons for the amount of protons, the nucleus is unstable and the atom is considered radioactive.(4) This is why ionized radiation is extremely dangerous in comparison to nonionized radiation (NIR), which usually doesn’t cause permanent

damage. Ionized radiation can cause various illnesses including hair loss, skin burns, birth defects, sterility, cancer, and death to name a few.(4)

When the radioactive nucleus changes its neutron to proton ratio to become more stable, radiation is emitted in one of four ways: Alpha, Beta, Gamma, and Neutrons. This is how ionized radiation is usually categorized. Alpha radiation occurs when two protons and two neutrons are emitted as the radioactive nucleus is reconfiguring. This reconfiguration enables the radioactive nucleus to become more stable and usually is a result of the decay of heavy molecules. Examples include radium, uranium, and actinium to name a few. Alpha particles can be blocked by a sheet of paper and cannot penetrate deep into the body, as most of the particles are absorbed by the skin. Due to the lack of penetration depth, alpha particles are not considered hazardous outside the body. They can, however, be hazardous at high doses to skin or to the body if inhaled.(8)

Beta radiation occurs when the neutron inside the nucleus of the radioactive molecule converts to a proton or when a proton converts to a neutron and a beta particle is produced as the molecule becomes more stable. Beta particles can penetrate deeper than alpha particles. Penetration can occur through skin into skeletal muscle and can pass through paper. Beta particles can, however, be stopped by wood or denser materials. Studies on survivors of radiation and on animals have shown that beta particles can cause epilation**,** moist desquamation (skin thinning/fluid seeps out), and acute tissue necrosis at high levels when exposed through the skin, as well as cancer when inhaled.(4)

Neutron radiation can penetrate deep into the body and come from a few different places to interact with the human body. When cosmic radiation interacts with the molecules in the air, neutrons are emitted from the nucleus of the molecule. Fusion or fission devices can similarly produce many neutrons.(5) Neutrons can be produced by nuclear explosions and release high energy neutrons. As far as exposure to humans, data is limited, with most of the information coming from the atom bomb survivors from Hiroshima and Nagasaki. It is challenging to draw definitive conclusions from data due to the body also absorbing gamma radiation as well. This makes it difficult to determine which effects come from neutron or gamma radiation. It has been estimated that only 1% of absorbed radiation was from neutron radiation.(6) In mice, neutrons have been found to cause leukemia, lung cancer, ovarian cancer, and skin cancer to name a few.(6)

Gamma radiation is the most commonly discussed radiation exposure and is produced when the radioactive nucleus splits in half. Gamma rays are the most dangerous external radiation source due to their penetration depth into the body. They also have the ability to penetrate through the skin and possible interaction with organs they come in contact with or pass completely through the body. With the numerous problems external sources of gamma rays have on the body, many studies have attempted to understand the effects they have on the body. One study looked at the effects that gamma radiation had on the development of children *in utero* after exposure through their mothers of the Hiroshima and Nagaski bombings. Mental retardation was observed at 43% for the fetuses exposed above 1 Gy.(7) Research also shows that leukemia, growth retardation, and intelligence reduction are all symptoms of fetuses

exposed to gamma radiation. Fetuses are also more sensitive to gamma radiation than their mothers who were directly exposed.(4) Multiple studies have also shown cataracts can develop in people who are exposed to 2 Gy of gamma radiation. A higher rate of cell death was also noticed in the small intestine of mice exposed to gamma radiation.(4) A significant decrease in male fertility was also observed in mice exposed to gamma radiation.(4) These are just a few examples of the devastation gamma radiation has on the body. It is important to note that x-rays are usually grouped with gamma rays, because they have the same properties and effect on the body.(4)

Currently, the "gold standard" for determining radiation biodosimetry is dicentric chromosome assay (DCA). The premise is that radiation exposure causes DNA strand breaks which causes abnormal chromosome replication, including dicentric chromosome formation. As the radiation exposure dose increases in the body, more dicentric chromosomes are formed. The amount of dicentric chromosomes is counted and compared to a calibration curve to estimate radiation dose. There are only two major US government laboratories with experience performing DCA which is very time consuming and expensive.(8). Thus, we propose a POC device that uses citrulline as the biomarker known to be correlated with radiation exposure.

I.2 Citrulline-aptamer assay

Citrulline is an amino acid that is found in free form around 40μM concentration in the blood of healthy humans. The majority of free citrulline is produced from glutamine by ornithine carbamoyltransferase (an enzyme) in the gut, specifically intestinal crypt cells, and is removed by the kidneys.(9) Due to the kidneys role in

removing citrulline, high plasma citrulline concentrations are often associated with chronic renal failure.(10, 11) The concentration of plasma citrulline is consistent with small bowel absorption capacity. Beyond radiation exposure, diseases that affect this can also cause changes in citrulline concentration, including celiac disease, viral enteritis, and acute cellular rejection following small bowel transplantation.(2, 12-18)

To detect citrulline in laboratory settings, high performance liquid chromatography (HPLC), liquid chromatography-mass spectrometry (LC-MS), and liquid chromatography-tandem mass spectroscopy (LC-MS/MS) have been used, but all are expensive and bulky.(19-23) To detect citrulline at the POC, we plan to build a citrulline POC SERS sensor utilizing competitive binding between the functionalized nanoparticles and free citrulline with thiolated fluorescently tagged citrulline aptamers bonded to a silver substrate. Thus, for our assay, DNA-based aptamers have been chosen as a molecular recognition element against the target analyte citrulline since they are uniquely suited to detect small molecules aptamers. An *in vitro* method of selection frequently referred to as Systematic Evolution of Ligands by EXponential enrichment or "SELEX" is how they are identified.(24, 25) When developing the aptamers, the process begins with a very large pool (~10^{15} unique sequences) of randomized polynucleotides, which is generally narrowed to just a few aptamer binders per molecular target. The aptamer pool is sequenced to identify candidate affinity reagents (aptamers), once multiple (typically 10-15) rounds of SELEX are completed.

Rivaling antibodies in both affinity and specificity, aptamers have been developed as ligands to important peptides and proteins.(26-29) Aptamers have also

been developed to bind cellular toxins and small organic molecules, and even targets as small as heavy metal ions.(30-36) An important advantage of aptamers is that they are developed entirely by *in vitro* methods enabling applications where it is desirable to have pure, affinity reagents that exhibit no batch-to-batch variation and are relatively inexpensive. Aptamers are also able to circumvent other challenges encountered with *in vivo* production incurred with antibodies. The immunogenicity of molecules smaller than a few thousand daltons, such as citrulline, is generally low and, therefore, usually requires the coupling of the target molecule (a hapten) to a carrier. Some hapten conjugates still do not elicit a sufficient immune response, and the coupling position of the hapten–carrier linkage may significantly affect antibody specificity.

Aptamers possess several other key advantages over their antibody counterparts, in addition to their amenability to targeting of small molecules.(37) More stable and sterically less bulky, they are smaller in size than antibodies. Oligonucleotides are made through chemical synthesis in stark contrast to antibodies. This process is well defined, highly reproducible, sequence independent and can be readily scaled up, and their production does not depend on bacteria, cell cultures or animals. Finally, yielding a considerably higher shelf life, they are much more stable at ambient temperature than antibodies, and they can tolerate transportation without any special requirements for cooling.

In order to characterize and fabricate the components of a future aptamer-SERS biosensor for citrulline, novel DNA-based citrulline aptamers were discovered by SELEX. While RNA aptamers to citrulline have been described previously by Famulok,

these aptamers' negative selection was only performed against glycine immobilized on agarose and had fairly weak affinity for the target of approximately 60μM.(38) Here, novel DNA aptamers against citrulline were developed, which are inherently more stable than RNA-based aptamers, and our aptamer selection has included counter-screening against a cocktail of the twenty essential amino acids. Functionalized nanoparticles with these novel aptamers are developed specific to citrulline to as part of the development of a POC device in which surface enhanced Raman is used as the sensing mechanism.

I.3 Raman/SERS

Raman scattering is a type of inelastic scattering in which the incident photon either loses energy (stokes) or gains energy (anti-stokes) to the vibrational and rotational motion of the analyte molecule. The Raman spectral peaks relate to the rotational or vibrational transitions specific to the molecular structure which provides the chemical "fingerprint" of the molecule. However, Raman scattering only occurs for 1 in 10^6-10^{10} non-elastically scattered photons.(39-42)

Surface enhanced Raman spectroscopy (SERS) drastically increases the Raman signal producing signals up to 10^{11} stronger.(43, 44) SERS enhancements easily allow examination of molecules in the micro-to-nanomolar concentration range in solution, explaining why SERS has the potential to become a good analytical method for biosensing.(45) SERS enhancement comes from two mechanisms: the chemical mechanism and the electromagnetic mechanism, which is the dominate factor.(46, 47) The chemical mechanism works through chemisorption of the analyte to the metallic surface, allowing the electrons from the molecule to interact with the electrons from the

metal surface. This mechanism leads to a theorized enhancement of up to 10^2.(39) The electromagnetic enhancement is wavelength dependent and comes from the interaction of the excitation wavelength with the localized surface plasmons on the metal surface. The localized surface plasmons (electrons oscillating) can occur on sharp metal tips, roughened metal surfaces, and noble metal nanoparticles.(41, 48) The SERS enhancement can vary drastically based on the metallic substrate.(41, 49, 50) Therefore, finding robust and reproducible metallic structures has been heavily researched. The most common metals used are silver (Ag) and gold (Au), and in some cases copper (Cu).(43) In our experiments we analyzed gold colloid, gold-silver nanocages, silica gold nanoshells, and silver nanocubes. Gold colloid has been a popular substrate for SERS. For our biosensing applications, its use can be problematic since aggregates must be formed typically using salt, which are time dependent, fall out of solution, and generally do not provide good reproducibility.(45, 51) However, for other biosensing purposes, gold colloid have been found to be useful. Gold nanostructures were used as SERS labels for in vivo detection of interior organelles.(51) Silver nanoparticles have been shown, in general, to produce a stronger SERS signal than gold, producing signals on the order of 10-100 fold higher.(51) Another benefit of silver is the ability to be excited over a broader spectrum then gold, particularly from the ultraviolet (UV) to the ionized radiation (IR), as opposed to gold which is typically excited in red or IR spectrum.(51)

In order to enhance the SERS signal and increase the Raman scattering event probability through creation of hot-spots, various mechanical methods have been used to

make the nanoparticles aggregate together.(52, 53) One mechanical aggregation method described by Hwang et al., utilized an optoelectrofluidic device to create plasmonic aggregates but their device was a complex system that required an alternating current (AC) voltage device to drive it.(54) Chrimes et al. used a dielectrophoresis approach to trap nanoparticles by changing the frequency and voltage to force nanoparticles to aggregate at certain locations.(55) This approach required the user to tune the frequency and voltage depending on the size and composition of the nanoparticle.(56) Zhou et al. investigated the use of microchannels with a valve system that, when closed, trapped the nanoparticles; however, the position of the aggregates were not always in the same location due to the large size of the microchannel with respect to the nanoparticle's size. Therefore, to find the aggregates the user had to move the objective around manually.(57)

Wang et al. developed micro-to-nanochannels to capture nanoparticles aggregates that form only at the micro-to-nano junction.(58) At their micro-to-nanochannel junction, they were able to produce ~10^8 SERS enhancements with detection limits down to 10pM but it was challenging to get reproducible channels that were not clogged or did not leak. In our approach, we not only present the design and manufacturing of a novel micro-to-nanochannel but use it to analyze and compare different colloidal particles in order to determine which nanoparticle has better post-functionalization utility for providing the best enhancement. Colloidal particles include spherical gold, gold-silver nanocages, silica gold nanoshells, and silver nanocubes.

CHAPTER II

USE OF AN INNOVATIVE MICRO-TO-NANOCHANNEL FOR THE CHARACTERIZATION OF SERS SIGNALS FROM UNIQUE FUNCTIONALIZED NANOPARTICLES[3] [4]

The initial aim of my dissertation and the focus of this chapter is the design and manufacturing of the novel micro-to-nanochannel and to use it to assess which nanoparticle might provide the strongest SERS enhancement using Mercaptobenzoic Acid (MBA) as a Raman reporter. This will help our ultimate application of detecting citrulline in a point-of-care (POC) device. Specifically, we compared four nanoparticles: colloidal spherical gold, gold-silver nanocages, silica gold nanoshells, and silver nanocubes.

II.1 Characterization of Nanoparticles

Nanoparticle composition, size, capping agent and morphology are the major components that affect the SERS signal. Therefore, we begin by looking at morphology using a transition electronic microscope (TEM) image for each nanoparticle. The shape and size of the four nanoparticles used in this study are shown in Fig. 1: gold colloid, gold-silver nanocages, gold-silica nanoshells, and silver nanocubes. The gold colloid

---

[3] Reprinted with permission from "Use of a micro-to nanochannel for the characterization of surface-enhanced Raman spectroscopy signals from unique functionalized nanoparticles" by Brian M. Walton et. al., 2016. Vol. 9715, Copyright 2016. Society of Photo Optical Instrumentation Engineers.

[4] Reprinted with permission from "Comparing Surface Enhanced Raman Spectroscopy from Colloidal Gold Nanoparticles and Nanocages" by B. M. Walton and G.L. Cote, 2015. Vol. 9332, Copyright 2015. Optical Diagnostics and Sensing XV: Toward Point-of-Care Diagnostics.

was purchased (Polysciences inc.) and was determined to be spherical in shape and roughly 60 nm diameter. Cube shaped and porous, the Au-Ag nanocages, supplied by Dr. Xia at the University of Washington, were determined to also be 60 nm.(59) Spherical, the gold-silica nanoshells were purchased (Nanocomposix) with a silica core and a gold shell and are 135 nm. Cubed in shape the silver nanocubes are 100 nm and were supplied by Dr. Wu at Texas A&M University in the Chemical Engineering Department.(60)

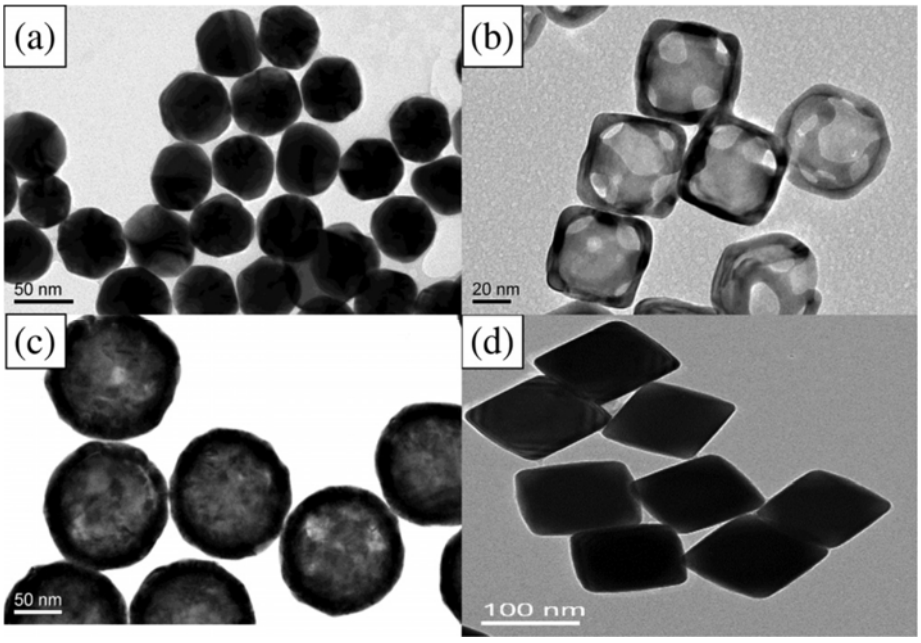

Figure 1: TEM Images of Morphology. TEM images of the four nanoparticles to illustrate the morphology. Colloidal (a) gold, (b) gold-silver nanocages, (c) gold-silica nanoshells, and (d) silver nanocubes. Reprinted with permission from Walton, et al. 2016.

II.2 MBA Binding to Nanoparticles

Mercaptobenzoic Acid (MBA) was the Raman reporter we used and is an organosulfur compound that is highly Raman active. To functionalize the nanoparticles with MBA, 5mg of MBA powder was mixed with 45 ml of 200 proof ethanol and sonicated for 30 minutes, yielding a 720 μM MBA/ethanol solution. From the initial stock solution, another dilution was performed by adding deionized water yielding a final MBA concentration of 22.3 μM. A 1:1 volumetric ratio with 30μl of 22.3μM MBA/ethanol solution for each of the four types of nanoparticles was vortexed for approximately 20 seconds. The nanoparticles were washed after one hour by adding 200 proof ethanol to the solution to fill up a 1.5ml centrifuge tube and centrifuging for 30 minutes. The supernatant was removed following the centrifugation and deionized water was added to fill up the 1.5ml centrifuge tube and centrifuged for 30 minutes. After 30 minutes the supernatant was removed again and the nanoparticles were re-suspended in 60μl of deionized water to match the initial volume of the nanoparticle MBA solution to keep the concentration the same. The previous capping agent on the nanoparticles is removed by the washing steps, citrate or polyvinylprrolidone (PVP) depending on the nanoparticle, and replaced with MBA.

II.3 Extinction spectra of nanoparticles

The four nanoparticles extinction spectra were analyzed to assess their resonance around the 780nm laser used in this study. If the nanoparticle extinction spectra were not initially in resonance with 780 nm extinction laser (such as the gold colloid), then they were shifted to the near-infrared region through mechanical aggregation in the micro-to-

nano channel junction. Previously, this shift has also been achieved by chemical aggregation using sodium chloride (NaCl) and can also be accomplished using elements that have a positive charge, which attract the negative surface charge of the citrate on the surface of the gold nanoparticle in the absence of mechanical aggregation.(61, 62) However, the SERS experiments discussed in this paper do not need NaCl due to the forced aggregation by the micro-to-nanochannel.

Some of the nanoparticles used in this study can be engineered to have their extinction spectra tuned to a particular wavelength. The nanoshells, for instance, have a dielectric core and are surrounded by a metal shell such as gold or silver, and their extinction spectra are tuned depending on the size and composition of the core/shell ratio but were purchased to have this extinction at around the 780 nm wavelength range.(63) The nanocages can also have their size and, therefore, their optical properties tuned by controlling the molar ratio between the silver template and chloroauric acid ($HAuCl_4$) when making the nanocages. They were also made by our colleagues to be resonant at near 780 nm.(59) With the silver nanocubes, the extinction spectra are tuned primarily by the edge curvature of the nanocubes and particle size by our colleague to near 780 nm.(64) Lastly, the extinction spectra of gold that do not resonate with the excitation source were chosen to illustrate how the forced aggregation at the micro-to-nanochannel shifts the extinction spectra to the desired wavelength to produce SERS signals.

Before and after the addition of MBA, the extinction spectra of each type of colloid was collected, as shown in Figure 2. The addition of the MBA at this concentration did not show a shift in the extinction spectra of the four nanoparticles, as

depicted in the data. This is due to the electrostatic affect from MBA that prevents the nanoparticles from aggregating. Nanoshells, nanocages, and nanocubes are in resonance with the 780nm extinction wavelength as depicted in Figure 2. As mentioned the gold colloid was the only nanoparticle not in resonance with the excitation wavelength, but a shift in the extinction spectra does occur when they are aggregated. For example, when NaCl is used, a shifted extinction spectra and aggregation occur for the gold, as shown in Fig. 2(b**)**.

To assess its effect on these particles, NaCl was also added to the other three nanoparticles before the addition of MBA. The salt did not shift the extinction spectra in these instances due to the steric stabilization provided by the capping agent PVP on the surface of these nanoparticles, unlike the electrostatically stabilizing citrate capping agent on gold nanospheres. For maximum intensity, it is important to note that the extinction spectra do not need to be directly over the excitation wavelength. Le Ru et al's (65) work shows that the extinction spectra is one indicator for the enhancement of the corresponding SERS signal when looking at a single nanoparticle. However, when using aggregation, the localized resonances at various locations on the nanoparticle are more effective for creating enhancements than the location of the extinction spectra maximum peak relative to the excitation wavelength because of the dimers, and so on, created.(65)

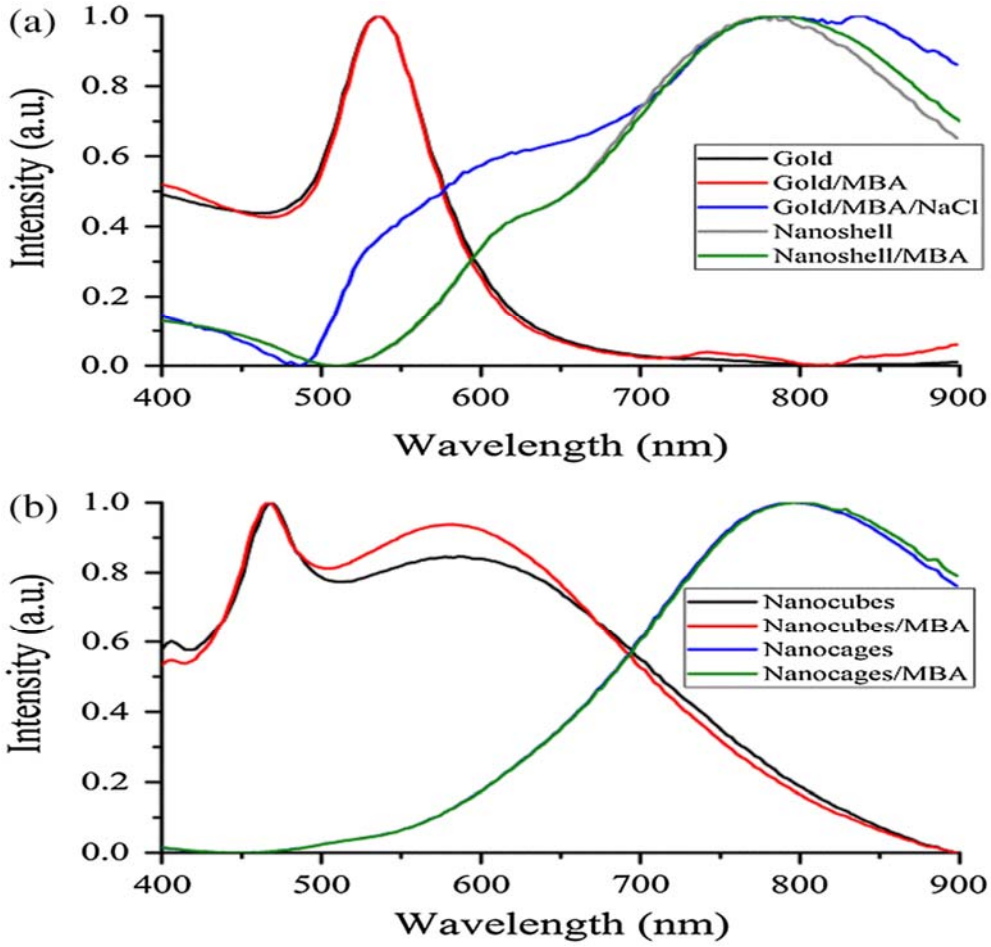

Figure 2: MBA Normalization Added to Extinction Spectra. The extinction spectra of the four nanoparticles before and after the addition of MBA normalized to 1. Also shown is gold with MBA and NaCl to show the shift NaCl causes on the extinction spectra. Reprinted with permission from B.M. Walton, et al. 2016.

II.4 Design of the micro-nano channel

The optofluidic micro-to-nanochannel nanoparticle aggregating device was fabricated using photolithography and etching as depicted in Figure 3. Fabrication was completed by our collaborator, Dr. Jun Kameoka, and his group in the Electrical and Computer Engineering Department at Texas A&M University. (52)

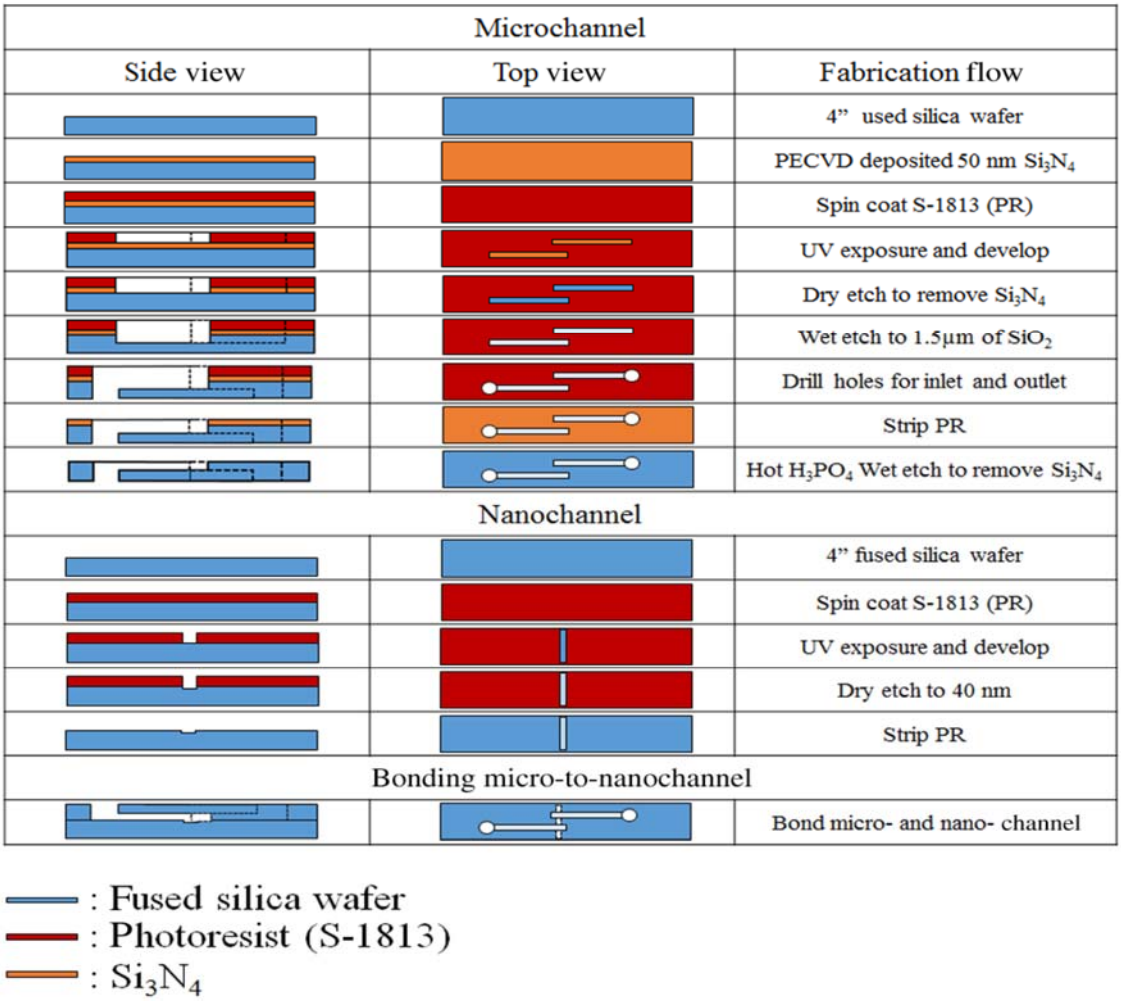

Figure 3: Fabrication Process for Optofluidic Device. Schematic diagram of the fabrication process for the optofluidic device. Reprinted with permission from B.M. Walton, et al. 2016.

As shown in Figure 3, a double-sided polished fused silica wafer substrate with a 500 μm thickness (Mark Optics Inc., Santa Ana, CA) was used to build the micro-to-nanochannel. 50nm of silicon nitride (Si_3N_4) was deposited onto the fused silica wafer using plasma-enhanced chemical vapor deposition (PECVD), for the fabrication of the microchannel. To make the 20μm wide microchannel pattern, photoresist is then spin-

coated on the Si_3N_4. To make the channels, we used a plastic mask and the smallest width for plastic masks are 20 μm. It is possible to use a metal mask, however, and the smallest width for them are typically 2μm. At the patterned area after UV exposure the Si_3N_4 is etched completely off by dry etching, leaving only the photoresist on the wafer. Etching away the exposed silica in the microchannel pattern down to 1.5μm following the previous step, the photoresist wafer is submerged into the buffer of etchant (BOE). The photoresist is stripped off by acetone and the Si_3N_4 layer is removed completely by hot phosphoric acid (H_3PO_4) (160ºC), which completes the microchannel fabrication, once the inlet and outlet holes for the microchannel are drilled. The photoresist is spin-coated directly onto a fused silica wafer and a 20 μm wide nanochannel is patterned onto the wafer for the fabrication of the nanochannel. To make a 40-nm deep nanochannel into the wafer carbon tetrafluoride (CF_4) reactive ion etching is used. The wafer with the microchannel and the wafer with the nanochannel are thoroughly cleaned via piranha solution and annealed at 1050ºC for 10 hours. This is done following the removal of the photoresist from the nanochannel wafer using acetone. The annealing process permanently bonds the microchannel and nanochannel substrates by thermal fusion bonding.

The completed optofluidic device shown in Figure 4 uses a micro-to-nanochannel junction structure to trap the Ag functionalized nanoparticles. The microfluidic channel has a depth of 1.5 μm and a width of 20 μm. The nanofluidic channel has a depth of 40 nm and width of 20 μm. Shown in Figure 4D, is the

mechanism for introducing and aggregating the nanoparticles in the micro-to-nanochannel.

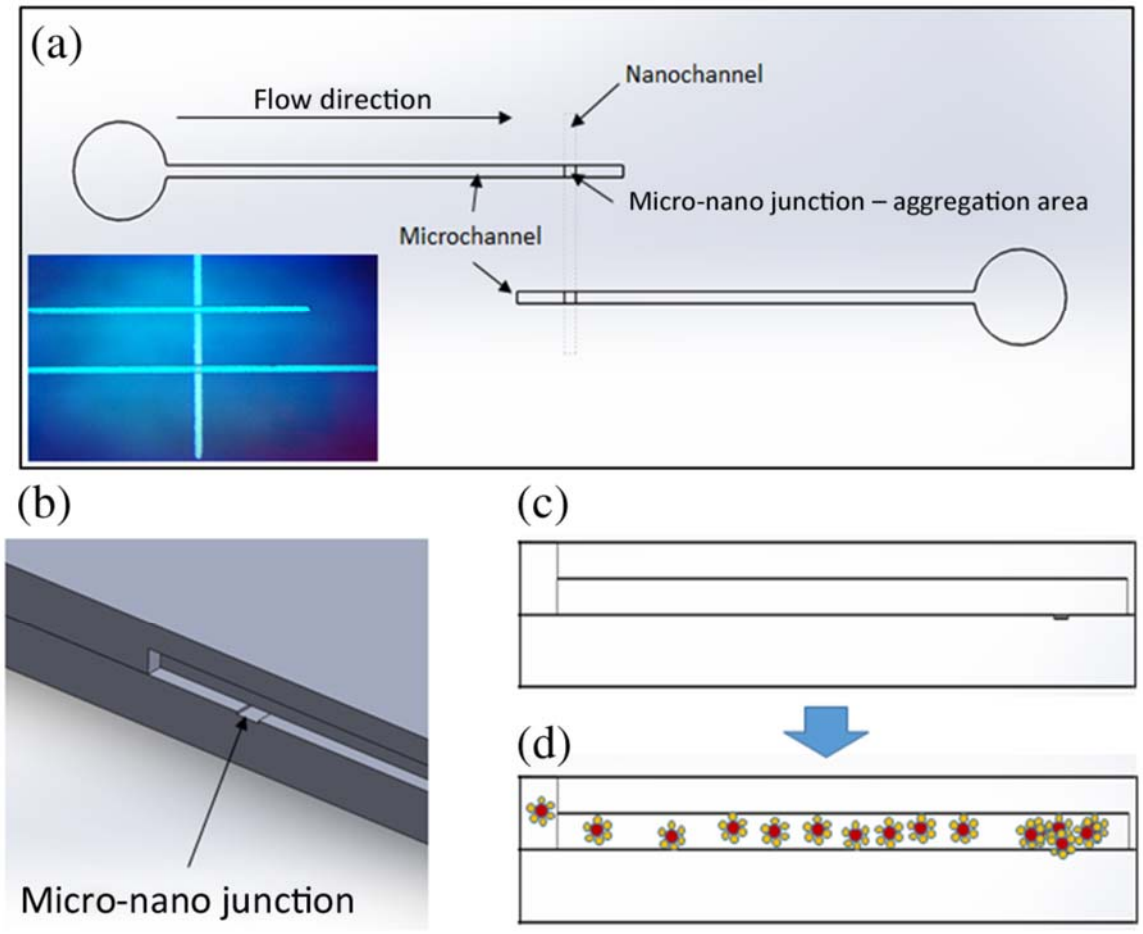

Figure 4: Fabrication Process for Optofluidic Device Part 2. Schematic diagram of the optofluidic device showing the (a) top view of the micro- to nanochannel junction, schematic, and bright field image; (b) three-dimensional side view of micro- to nanochannel; (c) side view of micro- to nanochannel; and (d) side view of micro- to nanochannel with nanoparticles aggregating. Reprinted with permission from B.M. Walton, et al. 2016.

After pipetting the sample of functionalized nanoparticle solution into the microchannel inlet, the solution is drawn into the optofluidic device by capillary force.(66) All the

nanoparticles have diameters that are larger than the 40nm micro-to-nanojunction. Therefore, they form clusters at the micro-to-nano junction, which is the SERS detection area.

II.5 Theory behind the micro-to-nanochannel device design

Capillary flow, the fluidic flow in this newly designed micro-to-nanochannel is caused by capillary force. We combine Navier-Stoke's equations with the Young-Laplace equation to describe the capillary flow in rectangular microchannels. The height of the microchannel is substantially smaller than the width. As a result, we only consider two-dimensional flow in the microchannel. Therefore, capillary flow in the microchannel is discussed in the x-direction and y-direction. From the equations, we get the time (Equation 1) and average velocity (Equation 2) the fluid takes to get to the micro-to-nanochannel junction. The detailed process is discussed further below.

$$t = \frac{12\eta L}{2\sigma\cos\theta}\left(\frac{h^2}{w}\left(\frac{1}{w}+\frac{1}{h}\right)\right)^{-1} \quad \text{Eq (1)}$$

$$u_{avg} = \frac{h^2}{12\eta w}\left(\frac{1}{L}\right)\left(2\sigma\cos\theta\left(\frac{1}{w}+\frac{1}{h}\right)\right) \quad \text{Eq (2)}$$

u_{avg}: the average velocity, x: position in $x-$direction,
t : time for fluid to arrive at micro $-$ to $-$ nano junction
h: height of microchannel, η: viscosity of fluid, w: width of microchannel,
σ: surfce tension, θ: contact angle, L: total length from inlet to micro $-$ t $-$ nano junction

The calculated capillary flow velocity was determined to be 64.9 cm/sec and the time for the fluid to arrive at the junction was 0.153 seconds, based on equation 1 and 2. The physical properties of the fluid, such as contact angle, viscosity, and surface tension, all

remain constant. Our microchannels were constructed with shallower channels that are 1.5 μm in depth and 20 μm in width to improve on Wang's design.(58) Wang's design was 6 μm in depth and 150 μm in width. The travel time and Wang's design are reduced; the velocity in our new micro-to-nanochannel is 2 times faster.

Rather than multiple etching steps, our micro-to-nanochannel is designed using an innovative one-step etching process. On a single wafer, previously a two-etching process, dry and wet etchings were required for making nanochannels and microchannels. The two channels are patterned on two different wafers in this approach. As a result, a single etching process is used to make nano and microchannels on each wafer. Specifically, hot wet etching is used to remove the Si_3N_4 layer. Multiple etching steps cause damage to the surface. Thus, one-step etching is advantageous over the previous method. Energetic plasma or active radicals damage the surface randomly because dry or wet etching would create an uneven surface. If multiple etching processes are required photoresist protection is not effective to secure the surface from these active chemicals. Once the surface is damaged, it will affect the thermal fusion bonding process which causes difficulties when trying to permanently bond two substrates. Therefore, multiple etching procedures should be avoided for bonding processes. One-step etching also produces a stronger bond between the two quartz wafers.(67) Finally, these channels are designed for one-time use only. To describe the capillary flow in rectangular microchannels, we combine the Navier-Stoke's equations (equations 1,2) with Young-Laplace equation (equation 5) using substitution. From these equations, we

get the average velocity (Equation 8) and time (Equation 9) the fluid takes to get to the micro-to-nanochannel junction. The above process is described in Figure 5 below.

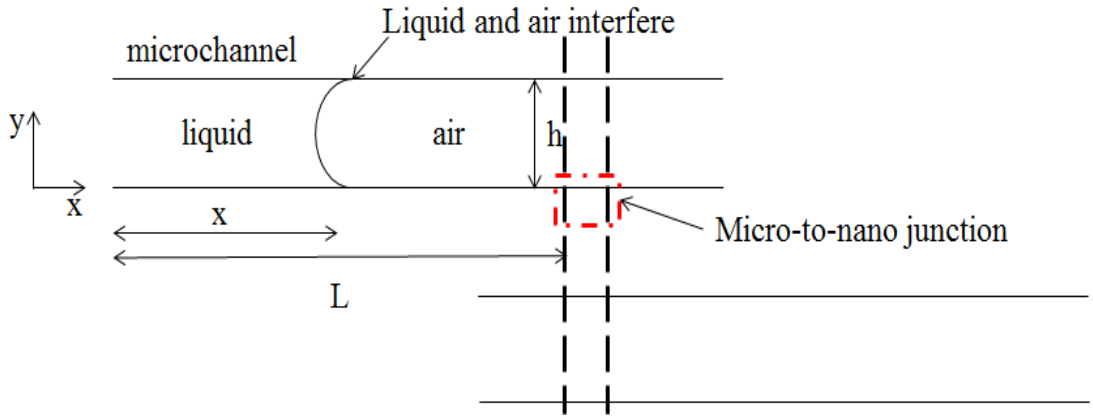

Figure 5: Schematic Diagram of Micro- to Nanochannel (Reprinted with permission from B.M. Walton, et al. 2016.)

Navier-Stokes

X-direction

$$\rho\left(\frac{\partial u}{\partial t}+u\frac{\partial u}{\partial x}+v\frac{\partial u}{\partial y}\right)=-\frac{\partial P}{\partial x}+\rho g_x+\eta\left(\frac{\partial^2 u}{\partial x^2}+\frac{\partial^2 u}{\partial y^2}\right) \quad \text{Eq (3)}$$

Y-direction

$$\rho\left(\frac{\partial v}{\partial t}+u\frac{\partial v}{\partial x}+v\frac{\partial v}{\partial y}\right)=-\frac{\partial P}{\partial y}+\rho g_y+\eta\left(\frac{\partial^2 v}{\partial x^2}+\frac{\partial^2 v}{\partial y^2}\right) \quad \text{Eq (4)}$$

where u: *fluid velocity in* $x-$ *direction,* v: *fluid velocity in* $y-$ *direction,* P: *pressure,* ρ: *density of fluid,* η: *viscosity of fluid,* g: *gravity,* t: *time*

Assumptions for simplified Navier-Stokes' Equation are as follows: (1) incompressible fluid (2) Steady state, (3) Laminar flow, and (4) Newtonian fluid. Incompressible fluid occurs when the density of fluid is constant; therefore, the divergence of flow velocity is zero from an equivalent statement: ($\nabla \cdot u \; or \; \nabla \cdot v = 0$). Steady state occurs when the fluid in the microchannel is constant. Therefore, the flow properties would not change with time, $\partial u/\partial t$ and $\partial v/\partial t$ are zero. Gravity effect and pressure distribution in y-direction can be ignored in the microchannel: g_x and g_y are zero. The y-direction velocity (v) does not have flow distribution in the y-direction due to the height being much smaller than the width. According to the flow continuity equation (equation 2), the $\partial v/\partial$y, $\partial u/\partial x$, and $\partial v/\partial x$ are zero.

$$\frac{\partial u}{\partial x}+\frac{\partial v}{\partial y}=0 \qquad \text{Eq (5)}$$

$$\frac{\partial^2 u}{\partial y^2}=\frac{1}{\eta}\left(\frac{\partial P}{\partial x}\right) \qquad \text{Eq (6)}$$

As a result, the Navier-Stokes' equation is simplified (Equation 4). The boundary conditions in the y-direction is when y=(±h)⁄2 which gives u=0, the solution to equation 3 is displayed in equation 4.

$$u(y)=\frac{1}{2\eta}\left(-\frac{\partial P}{\partial x}\right)\left(\frac{h^2}{4}-y^2\right) \qquad \text{Eq (7)}$$

According to Young-Laplace equation, the capillary pressure (ΔP) in a rectangular microchannel can be described as follows.

$$\Delta P=\sigma\left(\frac{1}{R_w}+\frac{1}{R_h}\right) \quad , \quad \text{where} \quad R_w=\left(\frac{w}{2\cos\theta}\right), R_h=\left(\frac{h}{2\cos\theta}\right) \qquad \text{Eq(8)}$$

$$\Delta P = 2\sigma \cos\theta \left(\frac{1}{w} + \frac{1}{h}\right) \quad \text{Eq (9)}$$

σ: $surface\ tension,\ R_w$: $curvature\ of\ width,\ R_h$: $curvature\ of\ height,$

w: $width\ of\ microchannel\ and\ h$: $height\ of\ microchannel, \theta$: $contact\ angle$

Substituting Young's equation (Eq. 5) into the solution of simplified Navier-Stokes' equation (Eq. 4), the capillary flow rate in the rectangular microchannel can be described as follows.

$$u(y) = \frac{1}{2\eta}\left(\frac{1}{x}\right)\left(2\sigma \cos\theta \left(\frac{1}{w} + \frac{1}{h}\right)\right)$$

The average velocity of capillary flow in microchannel can be defined by volume flow rate in microchannel.

$$u_{avg} = \frac{Q}{wh} = \frac{1}{wh}\int_{-h/2}^{h/2} \frac{1}{2\eta}\left(-\frac{\partial P}{\partial x}\right)\left(\frac{h^2}{4} - y^2\right) dy = \frac{h^2}{12\eta w}\left(\frac{1}{x}\right)\left(2\sigma\cos\theta \left(\frac{1}{w} + \frac{1}{h}\right)\right) \quad \text{Eq (10)}$$

Capillary flow can be defined by the physical meaning of velocity, speed or the average velocity.

$$u_{avg} \equiv \frac{dx}{dt} = \frac{h^2}{12\eta w}\left(\frac{1}{L}\right)\left(2\sigma\cos\theta \left(\frac{1}{w} + \frac{1}{h}\right)\right) \quad \text{Eq (11)}$$

$$t = \frac{12\eta L}{2\sigma \cos\theta}\left(\frac{h^2}{w}\left(\frac{1}{w} + \frac{1}{h}\right)\right)^{-1} \quad \text{Eq (12)}$$

u_{avg}: $the\ average\ velocity, x$: $position\ in\ x-direction,$

t : $time\ for\ fluid\ to\ arrive\ at\ micro-to-nano\ junction$

h: $height\ of\ microchannel, \eta$: $viscosity\ of\ fluid, w$: $width\ of\ microchannel,$

$\sigma: surfce\ tension, \theta: contact\ angle, L: total\ length\ from\ inlet\ to\ micro - to - nano\ junction$

Using the equations above with the constants below, we find the average velocity and time for the sample to get the micro-to-nanochannel junction. We also show the average velocity and time for Wang's paper below for comparative purposes.

Viscosity of water (η, 20oC): 1.002 N·S/m2

Contact angle (θ): 0^o (37)

Surface Tension (σ): 72.62x10-3 N/m (38)

Length (L): 1.5 x 10-3m

Width (W): 20 x 10-6 m

Height (h): 1.5 x 10-6 m

u_{avg}=64.9 cm/sec

Time=0.153 sec

The dimension of micro-to-nanochannel mentioned in Wang's paper

Viscosity of water (η, 20oC): 1.002 N·S/m2

Contact angle (θ): 0^o

Surface Tension (σ): 72.62x10-3 N/m

Length (L): 1.5 x 10-3m

Width (W): 150 x 10-6 m

Height (h): 6.0 x 10-6 m

u_{avg}=33.4 cm/sec

Time=0.298 sec

II.6 Micro-to-nanochannel surface enhanced Raman Spectroscopy analysis

The four different types of nanoparticles were analyzed in the micro-to-nanochannel. 5 µl of functionalized nanoparticles solution was pipetted into the microchannel inlet, and SERS scans were taken over time at the nanochannel junction. Each of the functionalized nanoparticles were evaluated in three different micro-to-nanochannels. The micro-to-nanochannel junction at 0 min, 5 min, and 25 min, respectively are shown in Fig. 18(a)-18(c). The microchannel is the horizontal channel, and the vertical channel is the nanochannel. No nanoparticles have been inserted into the micro inlet, at time 0, only deionized water. The micro-to-nanochannel is shown in Fig. 18(b), 5 minutes after 5 µl of the functionalized silver nanoparticles were pipetted into the micro inlet.

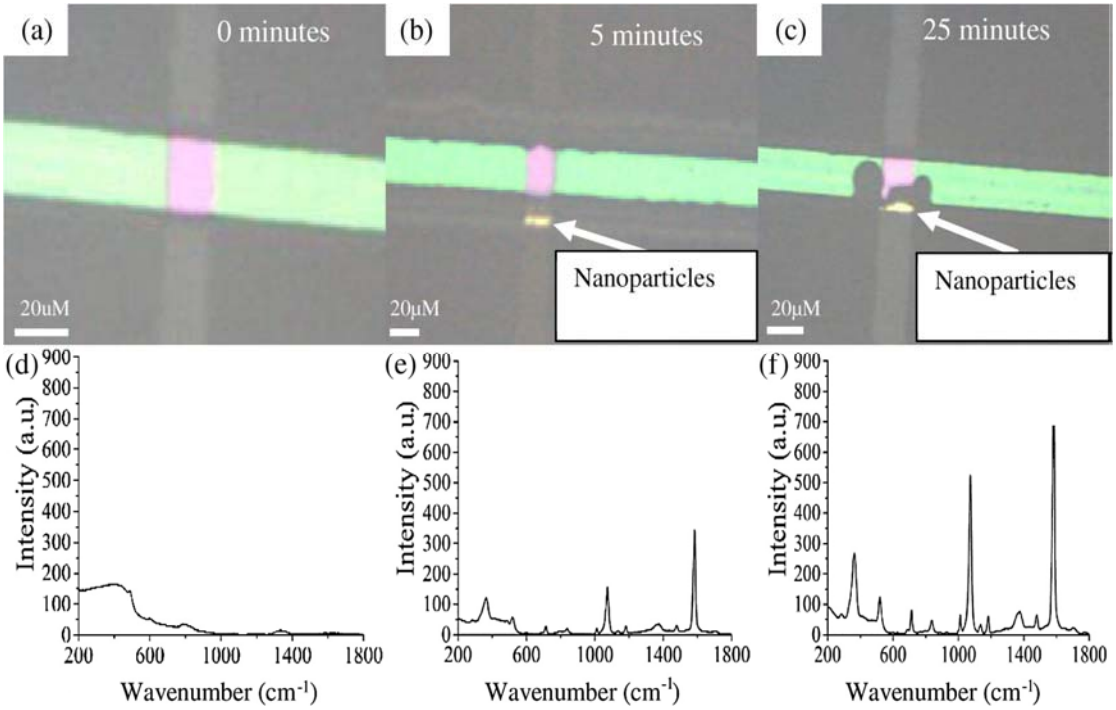

Figure 6: DXR Raman Confocal Microscope Images. Images taken with the Thermo Scientific DXR Raman confocal microscope at the micro- to nanochannel junction at various times with the respective silver nanocube SERS signal for that time directly below. Reprinted with permission from B.M. Walton, et al. 2016.

The nanoparticles are clearly seen aggregating at the micro-to-nanochannel, silver nanocubes in this example. The micro-to-nanochannel 25 minutes after the initial 5 µl solution was inserted into the micro inlet is shown in Figure 6(c), and the larger size of the aggregates formed at the junction can be visualized compared with the 5-minute aggregate size. Depicted in Figure 6(d), a Raman scan was taken to show the baseline signal of the micro-to-nanochannel. In Figure 6(e) the SERS spectra at 5 minutes, with the MBA peaks easily discernible relative to the background spectrum seen in Figure 6(d). The increase in SERS signal that is shown in Figure 6(f) that occurs after more nanoparticles have moved to the micro-to-nanochannel junction. The forced aggregation

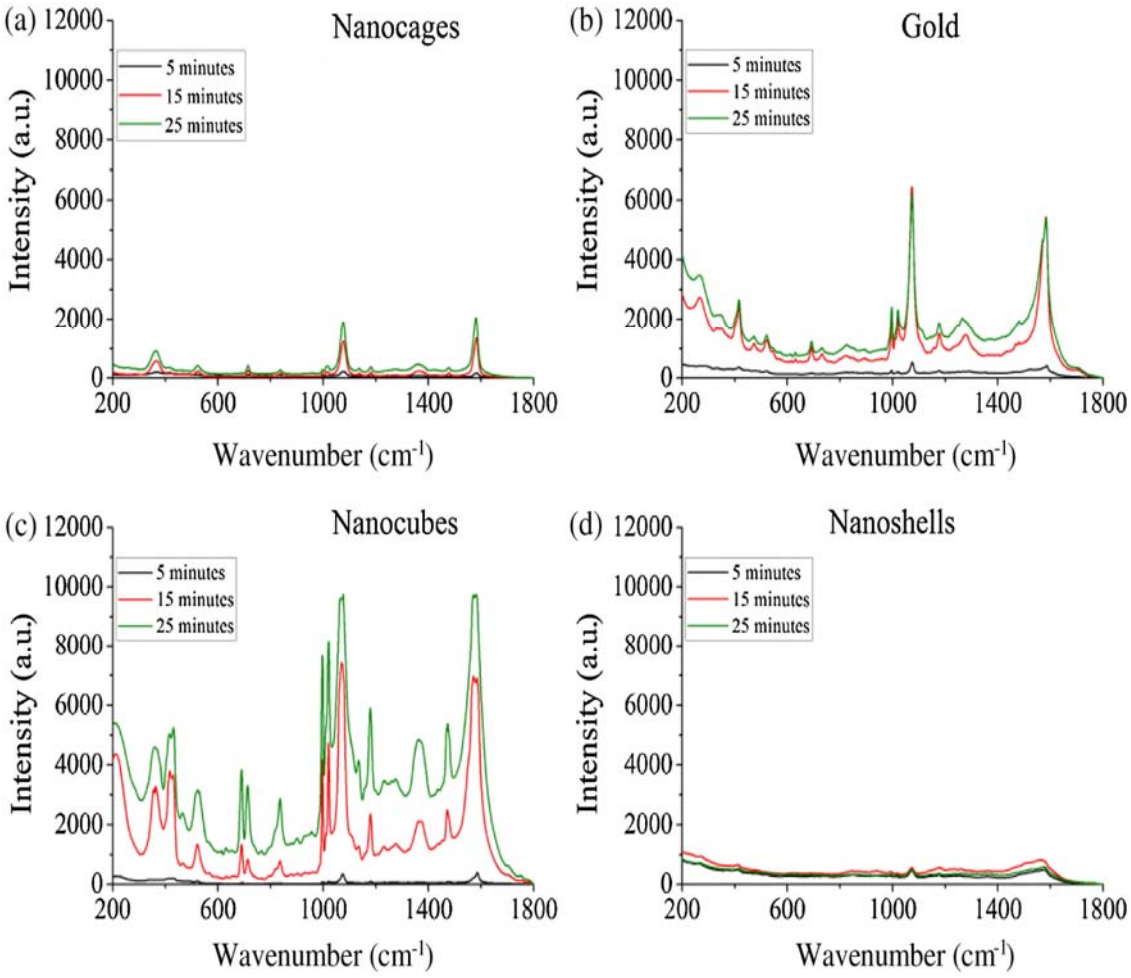

Figure 7: Functionalized Nanoparticles Over Time. The four functionalized nanoparticles over time. Data shown are an average of three SERS scans for 5, 15, and 25 min for nanocages, gold, nanocubes, and nanoshells (a)–(d), respectively. Reprinted with permission from B.M. Walton, et al. 2016.

at the micro-to-nanochannel junction is the cause of the increase, which creates many "hot spots" that form between the nanoparticles, silver nanocubes in this case, that are all in close proximity to each other.(51) The SERS spectrum of all four functionalized nanoparticles over time at the micro-to-nanochannel junction are shown in Figure 7(a)-

6(d). As depicted, the silver nanocubes had the largest signal among the four nanoparticles, which is likely due to the morphology. Lastly, to help visualize the effect of the micro-to-nanochannel over time the two main MBA peaks were plotted overtime, as shown in Figure 8.

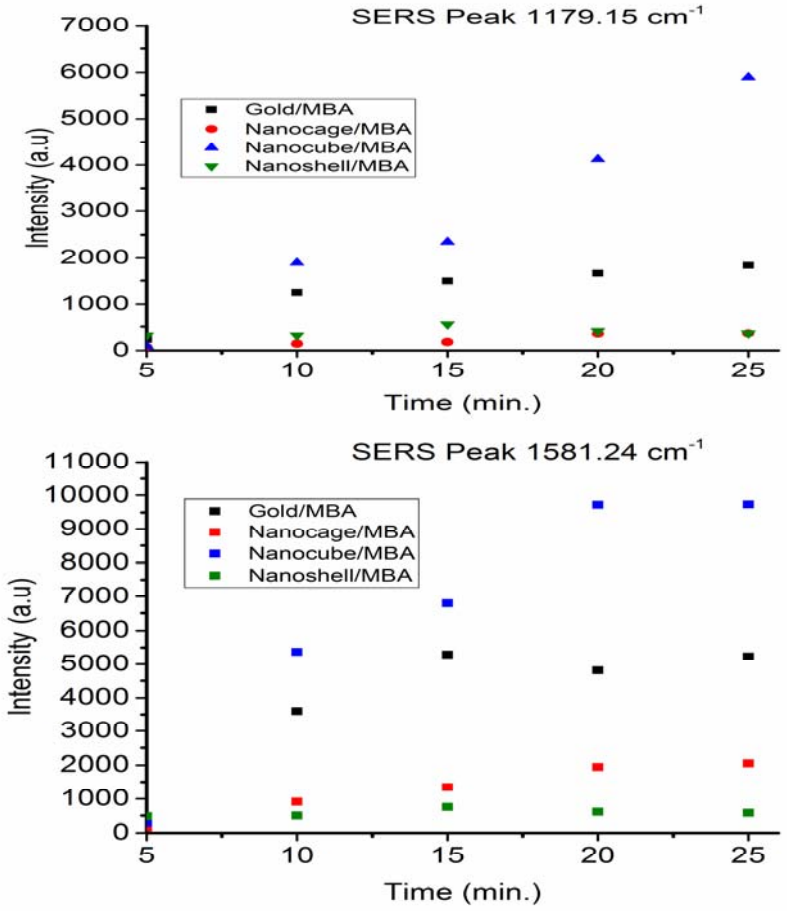

Figure 8: Average Intensities of MBA Over Time. shows the average intensities for the two main peaks of MBA over time. 1179.15cm^{-1} and 1581.24cm^{-1} both show silver nanocubes give the highest intensities overtime in the micro-to-nanochannel. Reprinted with permission from Walton, et al. 2016.

The silver nanocubes cube shape provides several corners to form hot spots, each giving a significantly increased SERS signal. The Raman spectra of 100 mM MBA dissolved in ethanol was used to compare with the intensity from 22.3 μM of MBA adsorbed to the surfaces of the various nanoparticles to calculate the enhancement factor.

The enhancement factor for the nanoparticles were calculated using Equation 13 to be 10^5, 10^5, 10^5, and 10^4 for silver nanocubes, gold nanospheres, gold-silver nanocages, and silica-gold nanoshells, respectively (68)

$$EF=\frac{I_{SERS}}{I_{NORM}}\frac{C_{NORM}}{C_{SERS}} \quad \textbf{(Eq. 13)}$$

Where I_{SERS} is the SERS intensity, I_{NORM} is the intensity of MBA at 100 mM concentration, C_{NORM} is the concentration of 100 mM MBA in moles, and C_{SERS} is the concentration 22.3 μM MBA in moles.

II.7 Additional SERS experimental data

Additional information and experiments can be found in Appendices A and B, showing the initial Raman reporter molecules (RRM) used with gold and nanocages colloid, their sample preparation, how those experiments were characterized, and finally concluding thoughts from comparing gold and nanocage nanoparticles for SERS. The experimental reason why MBA was chosen as the RRM molecule and how SERS signals can be affected, in general, can also be found in the Appendices A and B. Also, as already discussed, all four nanoparticles were put in the micro-to-nanochannel, the images of the nanoparticles at the micro-to-nanochannel entrance, as well as SERS data, can be found in the Appendices A and B. To help visualize the effect of the aggregation in the micro-to-nanochannel has on the SERS signals, SERS signals were also collected

from a microwell which does not cause any aggregation. Shown in Figure 9, the SERS signals are almost all at least factors of 1000 a.u lower than the SERS signal in the micro-to-nanochannel which further illustrates the drastic effect the micro-to-nanochannel has on the SERS signals.

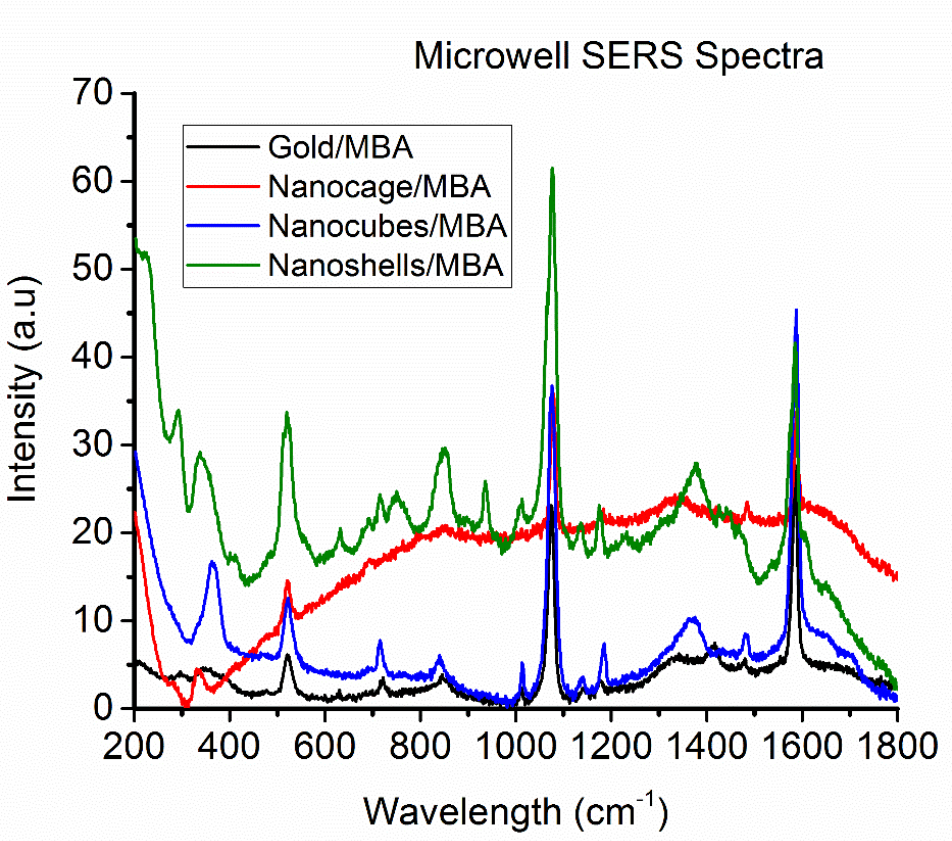

Figure 9: SERS Spectra of MBA. SERS Spectra of MBA. SERS spectra of MBA chemsorbed to gold, nanocages, nanocubes, and nanoshells respectively

II.8 Conclusions Optofluidic SERS study

In the micro-to-nanochannel, the data shows that silver nanocubes have a larger signal rather than gold nanospheres, silica-gold nanoshells, or gold-silver nanocages.

The silver nanocubes contributed to greater SERS intensities due to their size putting them in resonance with the excitation wavelength and their cubed shape which allowed for more hot spots to form than the spherical nanoshells and gold nanospheres.(51, 69) When in the vicinity of another nanoparticle, the nanocubes have several corners to form hot spots, providing more places where the hot spots can occur to yield strong SERS enhancements relative to the spherical nanoparticles. Although the nanocages have a cubed shape like the nanocubes, the nanocubes give stronger signals than the cube-shaped nanocages due to the plasmon dampening that occurs between gold and silver used to engineer the nanocages.(70) Altogether, the tuned extinction spectra, size, and many hot spots formed all contribute to the silver nanocubes having the strongest average SERS intensity when compared with the other nanoparticles.

CHAPTER III

SERS COMPETITIVE BINDING BIOSENSOR DEVELOPMENT UTILIZING SURFACE MODIFICATION OF SILVER NANOCUBES AND A NOVEL CITRULLINE APTAMER[5] [6]

The second aim of my dissertation and primary focus of this chapter is the surface modification and characterization of Ag nanocubes, specifically for citrulline detection. The other goal is to explain how the citrulline aptamers were developed and tested using backscattering interferometry. The Ag nanocubes were functionalized with a heterobifunctional PEG linker that forms an amide bond with citrulline, as well as mercaptobenzoic acid. After the nanocubes were functionalized they were characterized by zeta potential, transmission electron microscopy images, ultraviolet/visible spectroscopy, and SERS. Lastly, microscale thermophoresis (MST) was used to show that the aptamers bind to citrulline with an approximately 50 times stronger affinity than to the other amino acids.

III.1 Nanoparticle functionalization

To functionalize the silver nanocubes for the future POC sensor, four different protocols were made to determine which method was the best depicted in Table 1.

---

[5]Reprinted with permission from "Use of a micro-to nanochannel for the characterization of surface-enhanced Raman spectroscopy signals from unique functionalized nanoparticles" by Brian M. Walton et. al., 2016. Vol. 9715, Copyright 2016. Society of Photo Optical Instrumentation Engineers.

[6] Reprinted with permission from "Comparing Surface Enhanced Raman Spectroscopy from Colloidal Gold Nanoparticles and Nanocages" by B. M. Walton and G.L. Cote, 2015. Vol. 9332, Copyright 2015. Optical Diagnostics and Sensing XV: Toward Point-of-Care Diagnostics.

"Best" was defined by which protocol produced the most stable, completely functionalized nanoparticle.

1.Nanoparticle	2. Nanoparticle	3. Nanoparticle	4. Nanoparticle
RRM	RRM/PEG	RRM	RRM/PEG/Citrulline
PEG	Citrulline	PEG/citrulline	
Citrulline			

Table 1: Methods Analyzed to Determine Best Fit. Shows the four different methods that were analyzed to determine which method is best to functionalize the nanoparticles.

Functionalizing the nanoparticles and washing off the capping agent, PVP was based on a protocol by Moran, et al.(71) Protocol 1, which ultimately was the protocol which was determined to be the best for our future experiments, starts by centrifugation of the nanocubes for 30 minutes in water to remove the PVP capping agent. After centrifugation, the supernatant was removed, and the nanocubes were suspended in a 1:1 ratio of ethanol and 22.3 μM MBA. The pH of the nanocube sample was then tested and adjusted to be between 7.6 and 7.9. The nanocubes were then allowed to shake for 1 hour on a shake plate. After the shake plate, the sample was then centrifuged for 30 minutes, the supernatant was removed and replaced with a 1:1 ratio of deionized (DI) water and 22.3 μM MBA. To help dissolve the PVP capping agent, ethanol was initially added, but ethanol has been shown to weaken thiol bonds. Therefore, the second wash step was performed without ethanol.(72) The nanoparticle MBA sample was then placed

on a shake plate and left for 24 hours. A sample of citrulline bonded to PEG was made in another centrifuge tube, near the end of the 24-hour period. To make the PEG citrulline sample, PEG was first dissolved in 50 mM HEPES, making a final 5 mM PEG HEPES solution. A citrulline HEPES solution was made by gently dissolving citrulline in HEPES, making a 250mM final concentration. At a 1:1 ratio citrulline was then added dropwise to PEG. By displacing the NHS group on PEG, citrulline forms an amide bond to PEG. After the conjugation of citrulline to PEG, the PEG citrulline solution was slowly added dropwise at a 1:1 ratio to the nanocubes with MBA solution on a stir plate. Following this step, the solution was then allowed to sit 24 hours on a shake plate. Lastly, to remove any excess MBA, PEG or citrulline not bonded to the

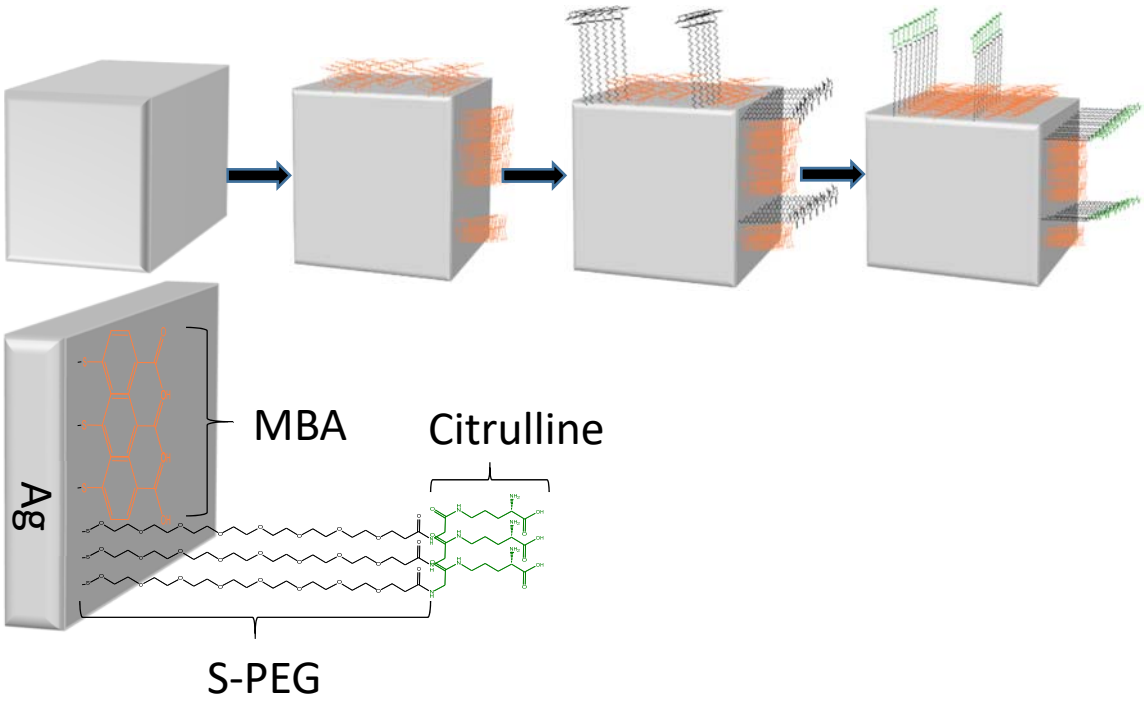

Figure 10: Surface Modification Process of Ag Nanocubes. 3D diagram of process to modify the surface of Ag nanocubes with MBA and citrulline

surface, the sample was carefully washed one last time via centrifugation at low speeds. Depicted schematically, this process is shown in Figure 10. There are a few important parameters to consider when making the protocol specific for the silver nanocubes. Having the correct pH for the various reactions to occur is one of the most important parameters. For the thiol groups on PEG and MBA, hydrogen was displaced from sulfur and binds to the silver surface in basic solutions above pH 7. The pH was approximately 3.4 when MBA was dissolved in deionized (DI) water and was raised using NaOH. The functional group on the heteriobifunctional PEG, NHS, begins to hydrolyze after 4 hours at pH 7. Within 10 minutes at pH 8.6, hydrolysis occurred. This means that the citrulline would not be able to bind to the PEG after this process. Performing the reaction before hydrolyze and choosing the correct pH is vital.

III. 2 Particle Characterization

To quantify the surface charge (ζ – charge) before and after functionalization Ag nanocubes were initially analyzed with a zetasizer. Ag nanocubes were diluted by taking 10 µl of the sample and 990 µl of HEPES buffer to machine specifications and 10 µl of Ag functionalized nanocubes were also diluted in the same manner as the nanocubes. The nanoparticles ζ-charge decreased from -24.2 mV before functionalization to -27.9 mV. Initially, PVP before functionalization then PEG after functionalization, the surface charge is similar due to the capping agents. Both prevent aggregation. To verify the extinction spectra, a Tecan UV/visible spectrophotometry was used, as depicted in Figure 10a, the functionalized nanoparticles were in resonance with the 780nm excitation wavelength. Functionalized nanoparticle samples were put into a Greiner 96

flat bottom transparent well plate and scans were recorded between 400nm – 900nm. No major shift was noticed after functionalizing the nanocubes, indicating no major aggregation occurred during the functionalizing process that would have shifter the extinction spectra (Figure 11a**)**. Shown in Figure 11b, transmission electron microscope (TEM)(JOEL JEM-2010 TEM) images of the silver nanocubes were used to show their size, 100nm and morphology; both of which are important for understanding the overall

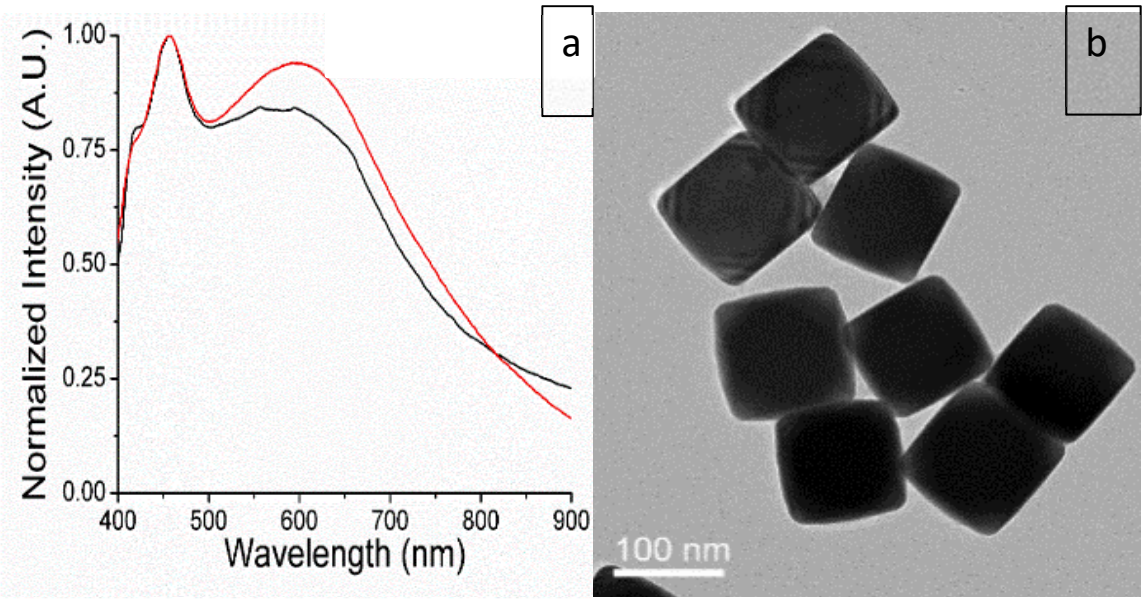

Figure 11: UV/VIS Spectrum, Functionalization, and TEM of Ag Nanocubes. a) UV/VIS spectrum of Ag nanocubes (black line) and functionalized Ag nanocubes (red line). b) TEM image of Ag nanocubes**.** Reprinted with permission from B.M. Walton, et al. 2016.

SERS intensity.(73) Multiple devices were used to further characterize surface chemistry, after proving the extinction spectra of the functionalized nanoparticles were in resonance with the excitation wavelength and did not shift after functionalized using the UV/VIS spectrometer. To characterize the silver nanoparticles size distribution, a

nanosight particle tracking system (Nanosight LM10, Salisbury, United Kingdom) was used.

A Thermo Scientific, DXR Raman microscope (Walthan, MA) was used to record the SERS spectras enhancement capabilities of the silver nanoparticles and find the limit of detection in the microwells. The functionalized nanoparticles were excited using a 24mW, 780 ± 0.2 nm, diode laser through a 10x Olympus microscope objective configured with an 1800 grooves/mm grating. The 780nm wavelength laser was chosen with the future biosensor in mind. Blood, he typical medium for biosensing, has a strong background fluorescence in the visible region confounding the SERS signal. Primarily due to water, the absorption of blood is very high beyond the mid-infrared wavelength region. Therefore, it is useful to look outside those wavelength regions in the near-infrared wavelength band in which the background signal relative to SERS in low. The integration time for the nanoparticles was 5 seconds and they were exposed 30 times. The Raman/SERS reported signal is the average of all 30 scans. Raman and SERS scans were performed to verify the Raman scan MBA was present on the nanoparticles, knowing that PEG and citrulline are present on the functionalized nanoparticles. To understand the SERS spectra, as depicted in Figure 12b, first a Raman scan of MBA powder was taken. To show where the vibrational modes are for the two main Raman and SERS MBA peaks (1099 cm^{-1} to 1075 cm^{-1} and 1075/1586 cm^{-1}, respectively) a peak analysis was done. The shift from 1099cm^{-1} to 1075cm^{-1} and 1596cm^{-1} to 1586cm^{-1} from Raman to SERS corresponds to MBA bonding to the metal surface.(74) The vibrational modes correspond to the C-H in- plane bending for the ~1075cm^{-1} peak.

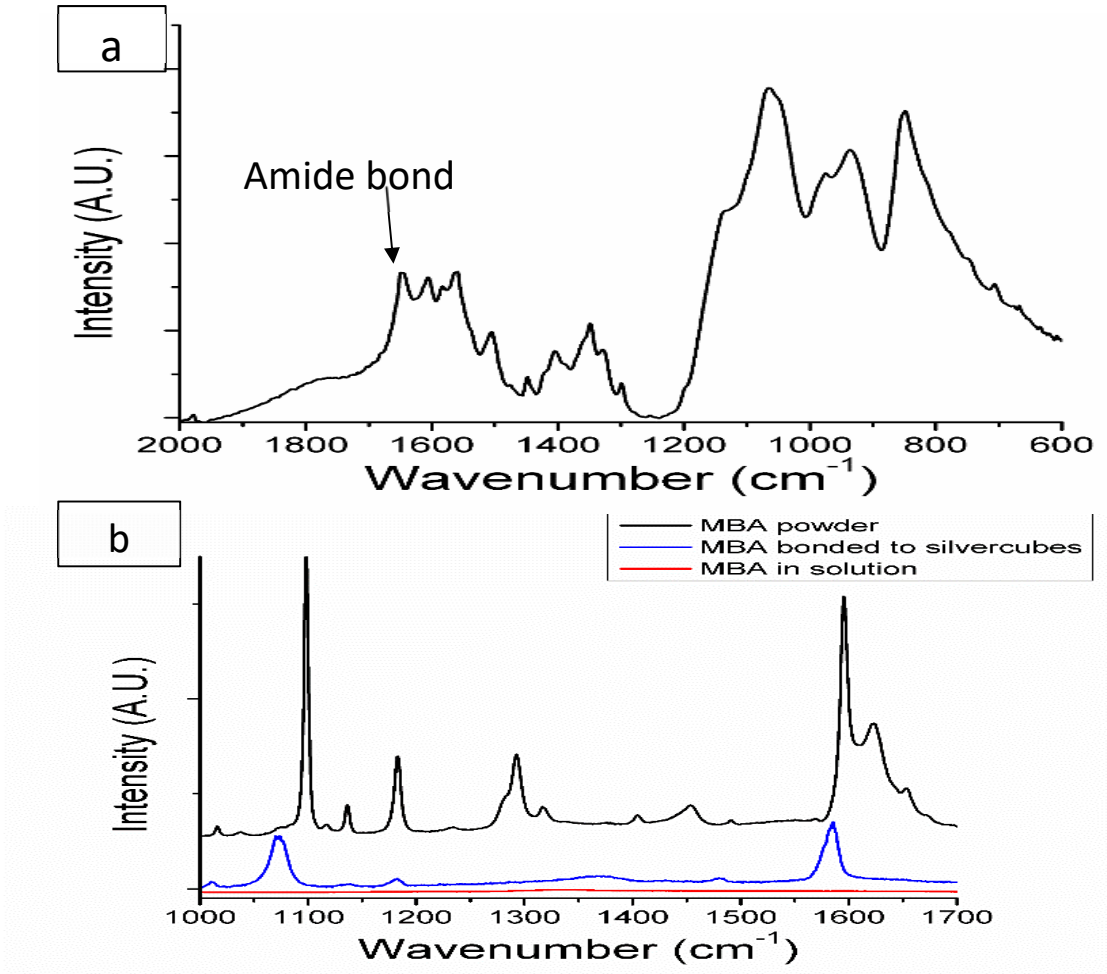

Figure 12: FTIR, Raman, and SERS Spectra. a) FTIR spectrum of functionalized Ag nanocubes, highlighting the amide bond formed between PEG and citrulline. b) Raman spectrum of MBA powder (top plot) and SERS spectrum of 22.3µM MBA bonded to Ag nanocubes (middle plot). Raman spectrum of 22.3µM MBA dissolved in PBS showing no detectable signal at this concentration as expected (bottom plot).

The C-C stretching corresponds to the ~1586cm^{-1} peak. A SERS scan of the functionalized nanoparticles with 22.3µM of MBA was taken to verify MBA did bond to the surface of the nanoparticles, using the Raman spectra of MBA powder to know where the Raman active peaks of MBA are located. To see if that concentration of MBA gives off a detectable Raman signal, a Raman scan of 22.3µM of MBA dissolved in PBS

was then taken. No detectable signal from 22.3μM of MBA dissolved in PBS as shown in Figure 12b. This verifies that the MBA peaks detectable when bonded to the Ag nanocubes can only come from the Ag surface enhancement. The enhancement of the nanoparticles was calculated to be 10^5. Raman spectra of 100 mM MBA dissolved in ethanol was used to compare with the intensity from 22.3μM of MBA adsorbed to the surfaces of the nanoparticles, to calculate the enhancement factor. The enhancement factor for the nanoparticles were calculated using Equation (13)(52) to be

$$EF=\frac{I_{sers}}{I_{norm}}\frac{C_{norm}}{C_{sers}} \qquad \text{Eq (13)}$$

I_{sers}: $12{,}940.65\ a.u, SERS\ intensity$; I_{norm}: $89.76\ a.u, The\ intensity\ of\ MBA\ at\ 100mM\ concentration$

C_{norm}: $Concentration\ of\ 100mM\ MBA\ in\ moles$, C_{sers}: $Concentration\ of\ 22.3\mu M\ MBA\ in\ moles$

A serial dilution was performed of the functionalized nanoparticles to find the limit of detection. An initial SERS scan was performed of the functionalized nanoparticles by first pipetting them into the microwell.

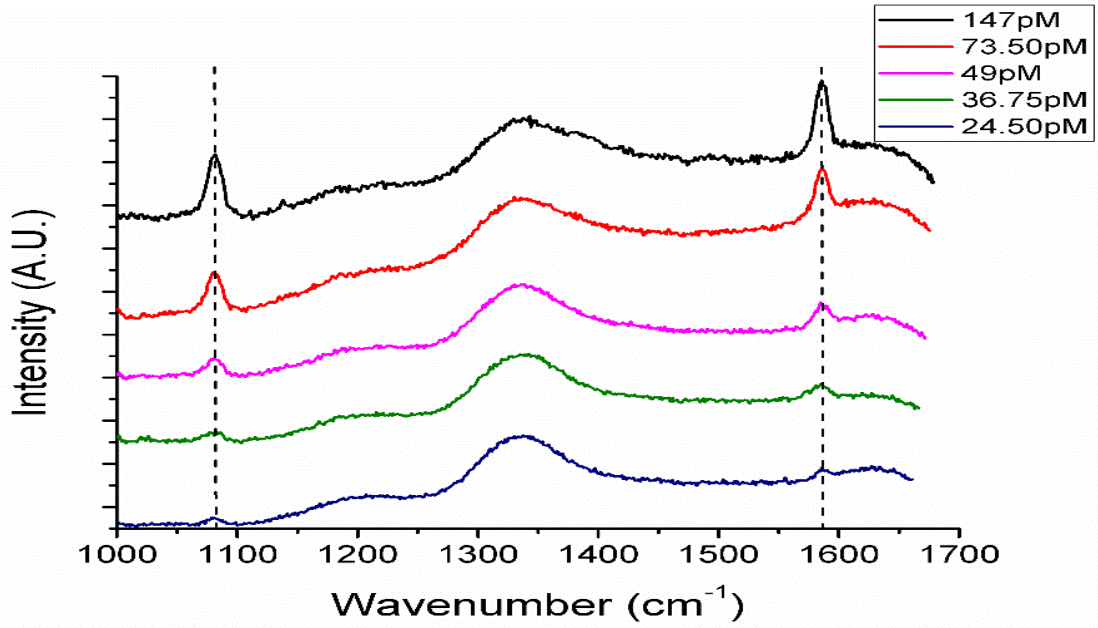

Figure 13: Serial Dilution of Functionalized Nanocubes. Serial dilution of functionalized nanocubes.

The solution was then pipetted in the microwell. Following the initial scan, the nanoparticles were diluted by mixing them with PBS at a 1:1 ratio and a SERS scan performed. Depicted in Figure 13, the surface modified nanoparticles were found to have a 24.50pM limit of detection, which was defined as where the 1075cm^{-1} and 1586cm^{-1} MBA peaks were no longer easily discernible after multiple dilution steps.

A fourier transform infrared spectrometry (FTIR)(Moore analytical, Houston, Tx) spectroscopy device was used to verify the amide bond was formed between citrulline and PEG. An important step was to confirm the citrulline did bond to PEG to insure the NHS group on the heterobifunctional PEG did not prevent the amine group on citrulline from bonding to PEG. From the FTIR spectra in Fig. 12(a) a peak analysis was

performed that revealed that an amide bond did form, which was depicted in the spectrum by the peak between 1630 cm^{-1}- 1670 cm^{-1}.

Data for microscale thermophoresis (MST) was collected from 2Bind molecular interactions. Using a Monolith NT.115 (Pico) MST instrument (NanoTemper Technologies GmbH, Germany) each test was repeated in triplicate, and read twice via thermophoresis + temperature jump at 80% laser power, 10% LED power at 25ºC. After finding the limit of detection for the nanoparticles, the aptamers were tested with a MST instrument. To perform the MST experiments, a Cy5-labeled version of the natural DNA citrulline aptamer (100μM stock in 1X PBS, 1mM MgCl2) was folded by incubating at 95ºC for 5 minutes, then allowed to slowly cool to room temperature (~25ºC). The aptamer was diluted in a solution of 1X PBS, 1mM MgCl2, and 0.05% Tween-20. This was then added to an equal volume of a two-fold dilution series of citrulline in a solution of 1X PBS, 1mM MgCl2, and 0.05% Tween-20. The final concentration of Cy5-citrulline aptamer was 5nM. The final concentration of citrulline ranged from 50μM down to 1.526nM depicted in Figure 14b. For the tests against the cocktail of 20 essential amino acids (EA), EA1, EA2, and EA3 are technical replicates of the same solution of 5 nM Cy5-labeled aptamer in a mixture of all 20 essential amino acids (Arginine, Lysine, Aspartic acid, Glutamic acid, Glutamine, Asparagine, Histidine, Serine, Threonine, Tyrosine, Cysteine, Methionine, Tryptophan, Alanine, Isoleucine, Leucine, Phenylalanine, Valine, Proline and Glycine). There is a dilution series of the mixture in 1x PBS pH 7.4, 1 mM MgCl2, 0.05% Tween-20, such that at the highest concentration the amino acids are each 500 μM, with a 2-fold serial dilution down from

there, to a final concentration of 15.26 nM. The aptamer was held constant at 5 nM. Lastly, T1, T2, and T3 are technical replicates of the amino acid citrulline with 5 nM Cy5-labeled aptamer, where T stands for test. The highest final concentration of citrulline is 50 uM, with a 2-fold serial dilution down from there in 1x PBS pH 7.4, 1 mM MgCl2, 0.05% Tween-20, to a final concentration of 1.526 nM citrulline. The aptamer was held constant at 5 nM. The dissociation constant, K_D for the citrulline aptamer binding to citrulline was calculated to be 4.96μM (the vertical dashed line in Figure 14b), with a 95% confidence interval of 3.325 – 7.378μM. To find the K_D, three technical replicates were collected for each concentration. Technical replicates two and three were baseline corrected toward the technical replicate one. This was done by computing the average fluorescence for each replicate then subtracting that value from replicate one's average fluorescence. Based on the MST-based affinity data, the K_D for citrulline aptamer was determined to be approximately 5μM. The aptamer does appear to have some minor affinity for the other 20 amino acids, but the affinity is weak, ~250μM. Thus, the aptamer is at least 50-fold more selective for citrulline than the other 20 amino acids.

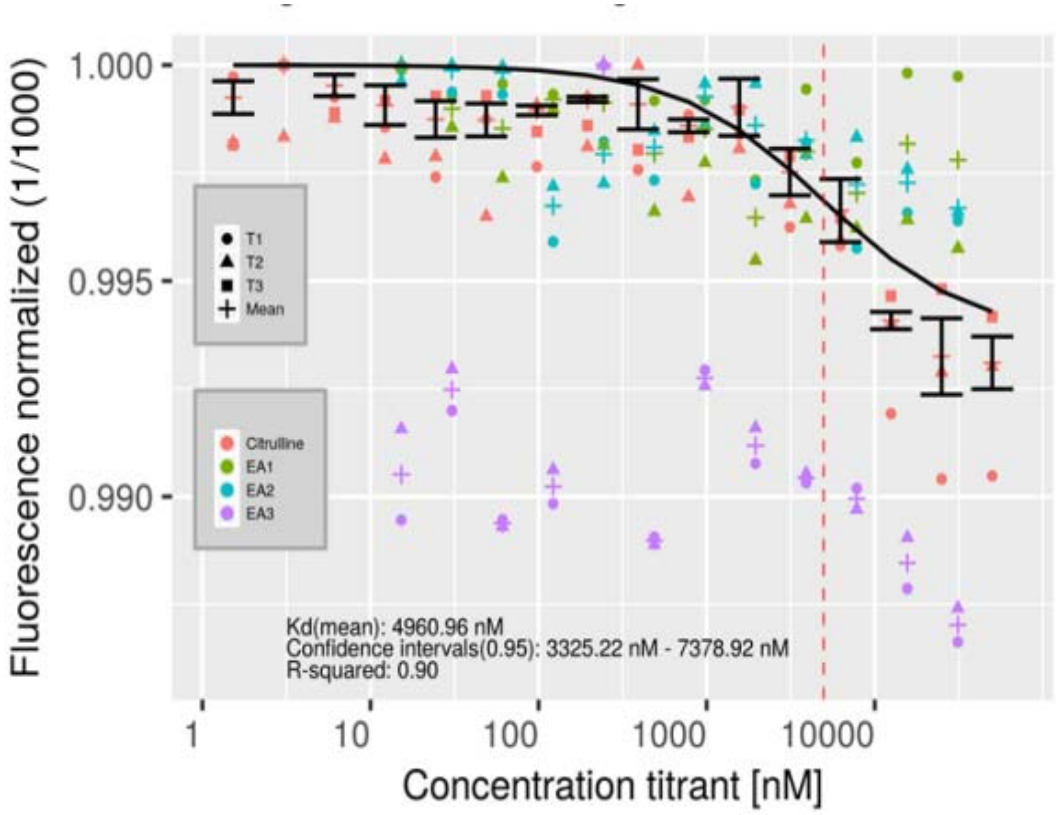

Figure 14: MST Binding Curve for Citrulline Aptamers. MST binding curve for citrulline aptamers. T1, T2, and T3 represent each test run on the MST. The 20 amino acids were separated into EA1, EA2, and EA3.

III.3 Additional MST data for initial citrulline aptamers

The initial citrulline aptamers developed for the future biosensor were tested with MST against citrulline are shown in the Appendices C and D. Briefly, they were tested against amino acids, as above and although they did bind to citrulline they also binded to the other amino acids found in plasma. Therefore, additional aptamers had to be developed using a new Basepair proprietary selection method.

III.4 Concluding Thoughts on SERS Competitive Binding Biosensor Development Utilizing Surface Modification of Silver Nanocubes and a Novel Citrulline Aptamer

For a future SERS citrulline competitive binding assay, Ag nanocubes successfully functionalized were presented for the first time. An UV/VIS spectrometer was used to verify that the extinction spectra was in resonance with the excitation wavelength, characterizing the functionalized nanoparticles. To ascertain the length of the nanocubes and visualize the morphology, TEM images were used. To prove citrulline did bind to the PEG on the surface of the nanocubes, an FTIR was used and SERS scans were used to verify MBA binding to the surface of the nanoparticles. Lastly, MST was used to prove the novel citrulline aptamers do bind to citrulline with a strong affinity in comparison to the other amino acids. SERS scans were also used to show a potential limit of detection to 24.5pM.

CHAPTER IV

BUILDING SERS BIOSENSORS[7] [8]

The emphasis of this chapter and final aim of this dissertation is to build a citrulline SERS biosensor. Two different approaches to build the citrulline sensor are discussed and analyzed. The first approach involves using competitive binding between the free citrulline and functionalized nanoparticles with citrulline aptamers that are on silver SERS active substrates. The second approach involves binding the citrulline aptamers to the nanoparticles and watching the SERS signal change in a microwell as free citrulline is introduced.

IV.1 PDMS mold for SERS substrate

The first step in making the competitive binding SERS sensor involves functionalizing the silver substrate with aptamers. To make sure aptamers only binded to the SERS active region of the Ag substrates, an aluminum mold was machined to produce a thin piece of polydimethylsiloxane (PDMS). The PDMS piece, shown in fig. 15, is designed to be in contact with the chip on either side of the active site. Initially, in order to create space between the lens of the fluorescent microscope and the aptamer-coated surface, different molds were created to create different spaces.

---

[7]Reprinted with permission from "Use of a micro-to nanochannel for the characterization of surface-enhanced Raman spectroscopy signals from unique functionalized nanoparticles" by Brian M. Walton et. al., 2016. Vol. 9715, Copyright 2016. Society of Photo Optical Instrumentation Engineers.

[8] Reprinted with permission from "Comparing Surface Enhanced Raman Spectroscopy from Colloidal Gold Nanoparticles and Nanocages" by B. M. Walton and G.L. Cote, 2015. Vol. 9332, Copyright 2015. Optical Diagnostics and Sensing XV: Toward Point-of-Care Diagnostics.

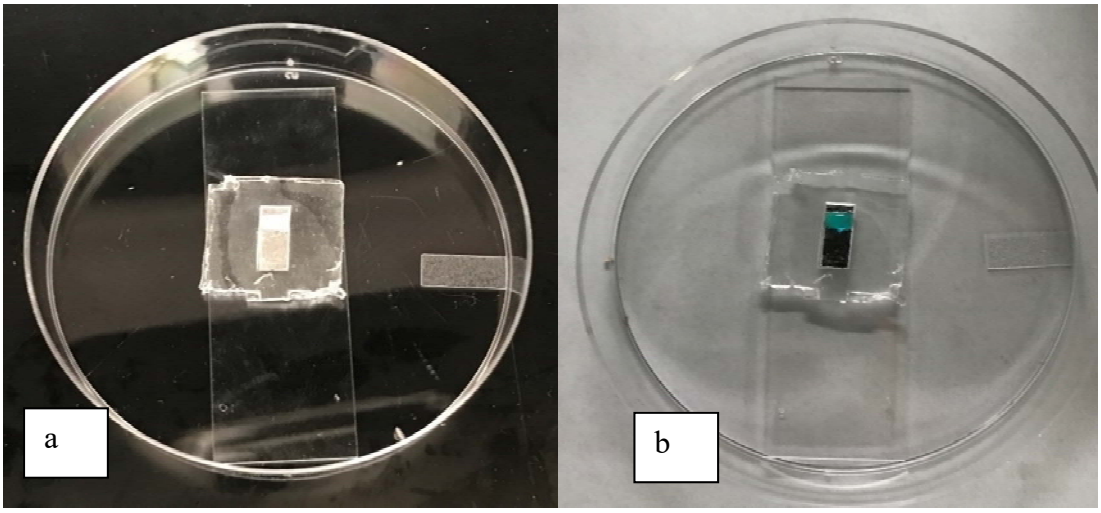

Figure 15: PDMS Mold for SERS Substrate. a) Shows the PDMS mold over the substrate on top of a glass microscope slide in a petri dish. b) Shows aptamers (in green) only at the SERS active site inside the PDMS mold

Molds to produce spaces of .1, .25, and .5mm were developed and are shown in figure 16, but it was quickly determined that the microscope objective needed to sit directly on a coverslip that touched the aptamers. However, to form the PDMS molds/spacer, PDMS was mixed in a 10:1 ratio with the curing agent and poured over the bottom part of the mold until filled. The PDMS inside the mold was degassed for approximately 20 minutes to remove excess air bubbles. Then, the top part of the mold was pressed onto the bottom. The mold was placed into a preheated oven at 85^{o}C to bake for 30 minutes to cure. The mold was then removed and allowed to cool overnight to complete curing. The top piece of the mold was pried off using a metal spatula. Then, the spatula was used to peel and remove the cured PDMS from the bottom piece of the mold. Any remaining,

very thin PDMS over the active site was carefully trimmed away.

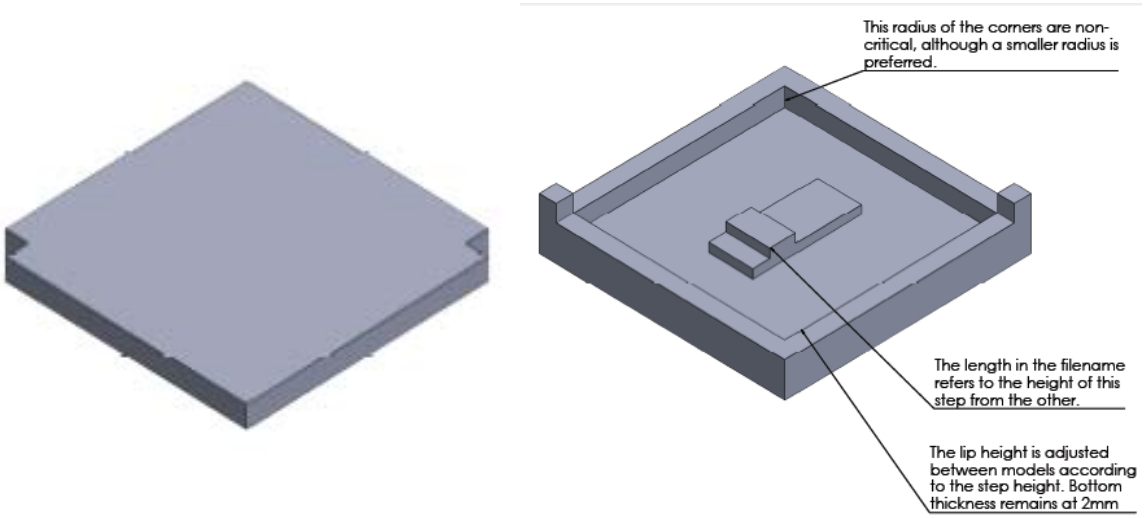

Figure 16: Aluminum Mold Used to Make the PDMS Molds. The aluminum mold used to make the PDMS molds. On the left is the top and on the right is the bottom.

IV.2 Aptamer binding to silver substrate

After finding the correct nanoparticle (Ag nanocube), functionalizing the nanoparticle, and developing the citrulline aptamer we begin the process of putting together the citrulline sensor. We start by binding the aptamer to the substrate by pipetting them into the PDMS mold discussed above. Initial tests were done trying to bind the aptamer to maleimide slides, but those yielded no positive results. We then tried Ag substrates with active SERS regions on them. Images were taken of the silver substrates without aptamers on them to see if any fluorescent signal could be detected; none were. Next, the slide with the aptamers were tested. As mentioned above we had to take the PDMS mold off the slide due to the short working distance of the oil immersion

microscope objective. However, this did not cause any major problems because the aptamers that had already been given time to bond to the active region via the thiol group to the substrate and a coverslip was placed over the aptamers to prevent the objective from directly touching the aptamers. The fluorescence microscope did verify the aptamers binded to the substrate by detecting the Cy5 tag on the aptamers shown in figure 17.

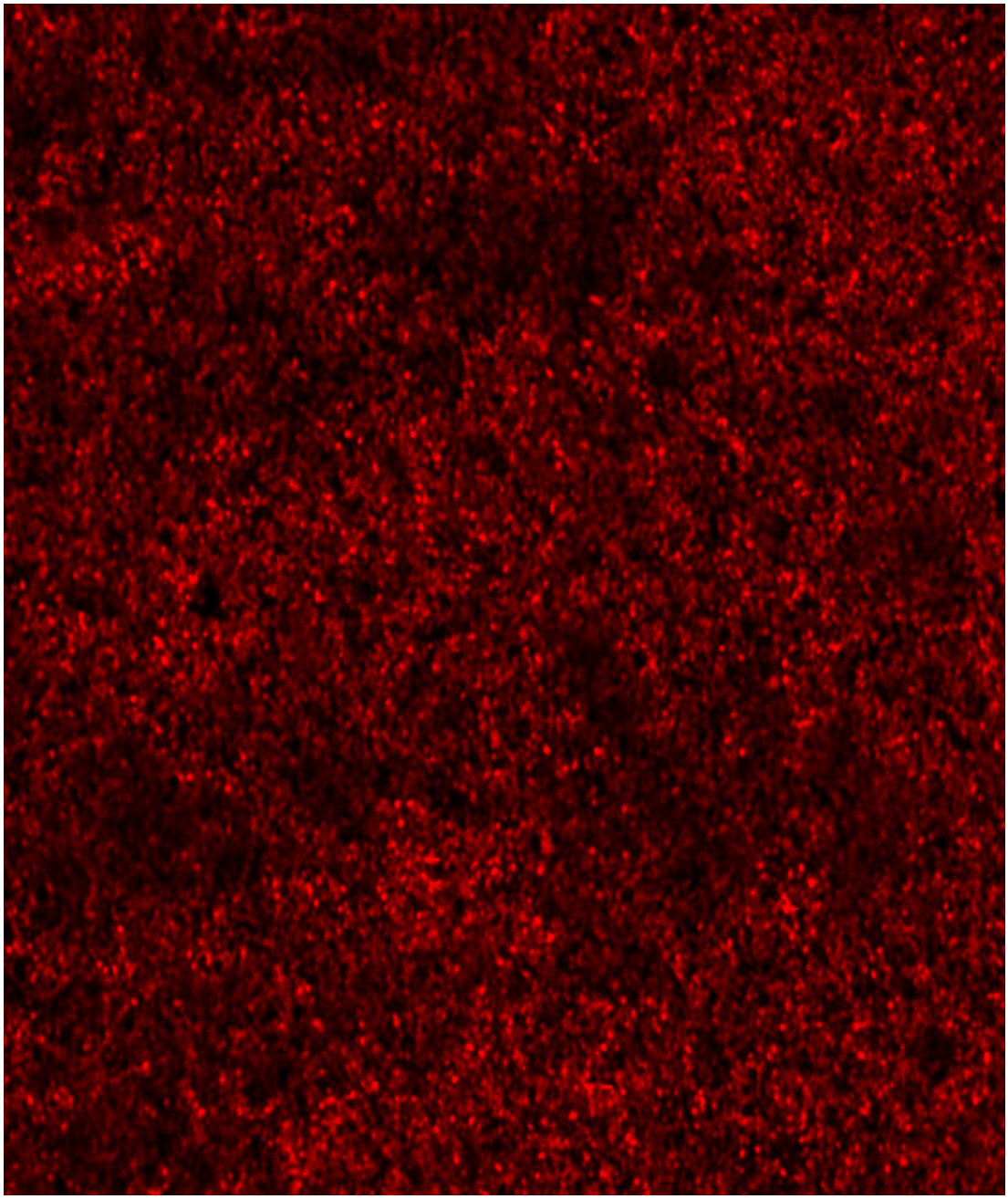

Figure 17: Aptamers Bonded to Silver Substrate with Fluorescent Microscope.

IV.3 Competitive binding SERS

The first sensor made was a competitive binding SERS sensor. In theory, the competitive binding sensor works by first adding the citrulline aptamers on the silver substrate, then allowing the functionalized nanoparticles with citrulline on them to bind. A SERS scan is then collected. Lastly, free citrulline is introduced to the assay and a correlation is made between the free citrulline introduced and the amount of nanoparticles displaced, depicted in figure 18. A SERS scan is then taken of the substrate again, which should result in a lower SERS signal. After proving the aptamers

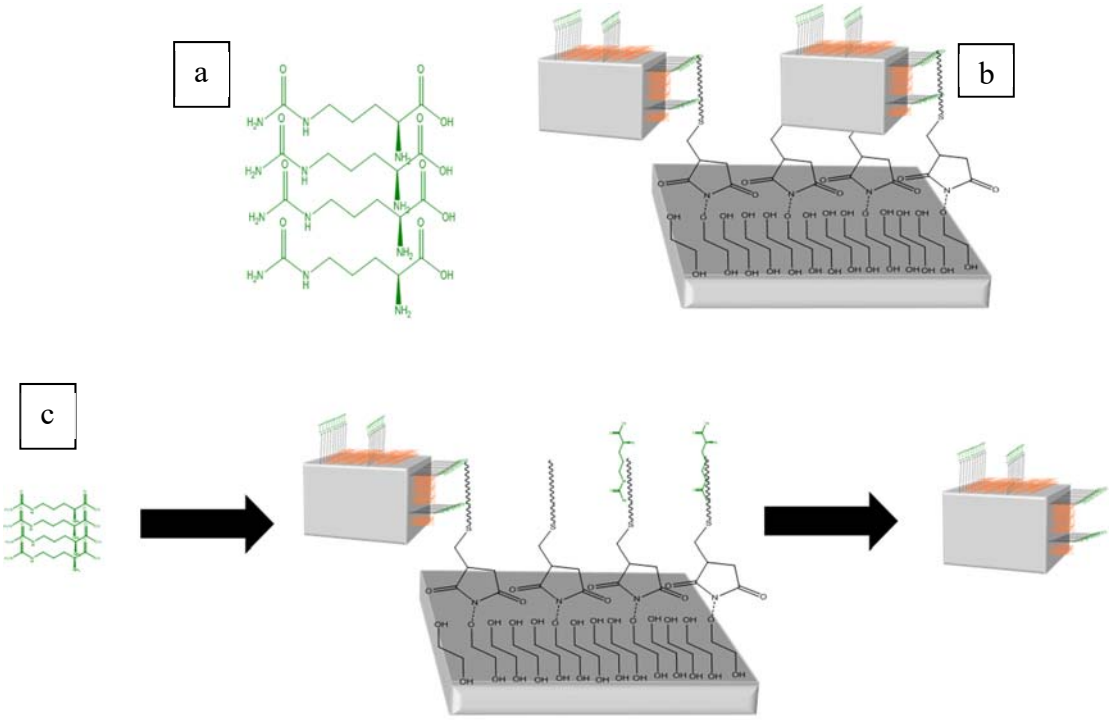

Figure 18: Schematic Diagram of Competitive Binding SERS Sensor.
a) Shows free citrulline b) Shows aptamers binded to maleimide slides with the functionalized nanoparticles binding to the aptamers. c) Shows free citrulline competitively binding to the aptamers and displacing the nanoparticles.

did bind to the substrate, we used SERS to test the sensor, shown in figure 19. After verifying the silver slide before functionalization does not have any Raman signals, the aptamers were added and a MAP of the SERS active region was taken, as depicted in figure 20**.** The MAPS also show the 104 locations SERS scans were taken over the

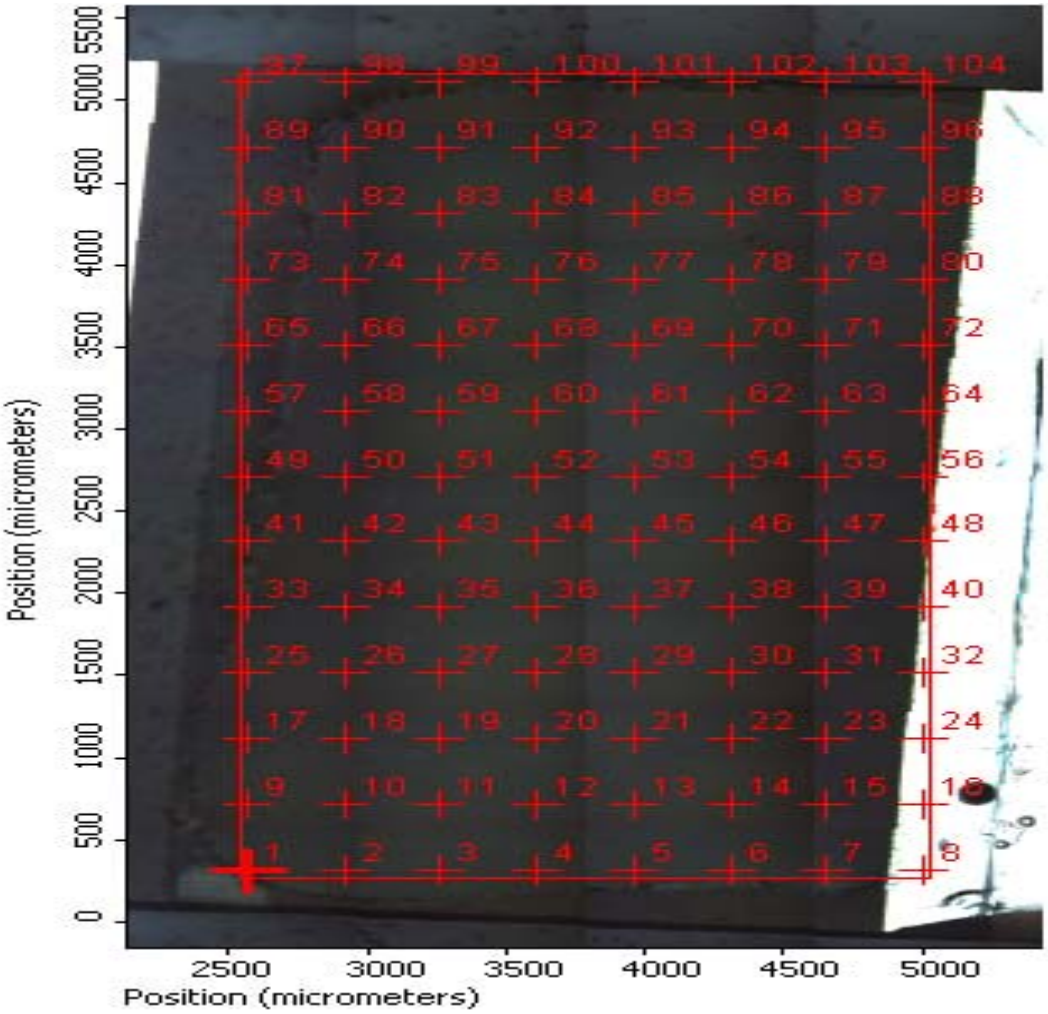

Figure 19: Brightfield Image of SERS Active Region. Image of active region of SERS slide and locations of the SERS scans.

SERS active region. SERS scans were taken before any aptamers were added to the

silver substrate, after the aptamers were added, after the functionalized nanoparticles were added, and after the free citrulline was added. The MAPS were also taken of the active region with aptamers with functionalized nanoparticles and aptamers with nanoparticles and 100μM of free citrulline. Preliminary test of the sensor seems to suggest that the sensor does work. Monitoring the MBA peak at approximately 1089 cm^{-1}, it was used to show that the sensor does work. PBS doesn't have a strong SERS signal at that location. After the probes (functionalized nanoparticles) are added, we see a large increase in SERS intensity. After multiple wash steps were performed to remove any probe not bond to the aptamers a SERS scan was performed, the MAP of the SERS active region is shown in figure 20. Lastly, 40μM of free citrulline was then added to the sensor and the excess solution was pipetted out. The SERS signal does, in fact, drop after the free citrulline was added and illustrated in figure 21a. Figure 21b also shows error bars of the previous experiment; the same experiment was performed three times on different silver substrates and compiled together.

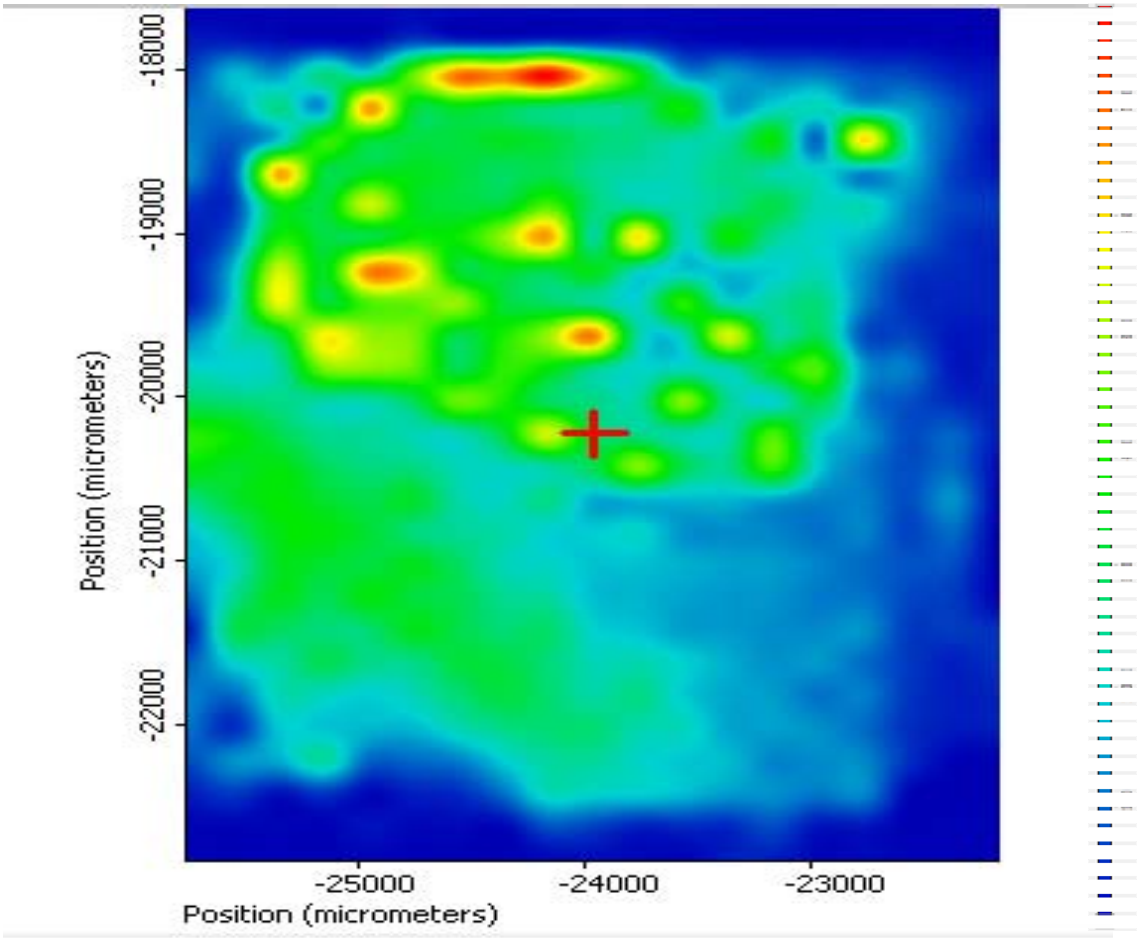

Figure 20: MAP of SERS Active Region.

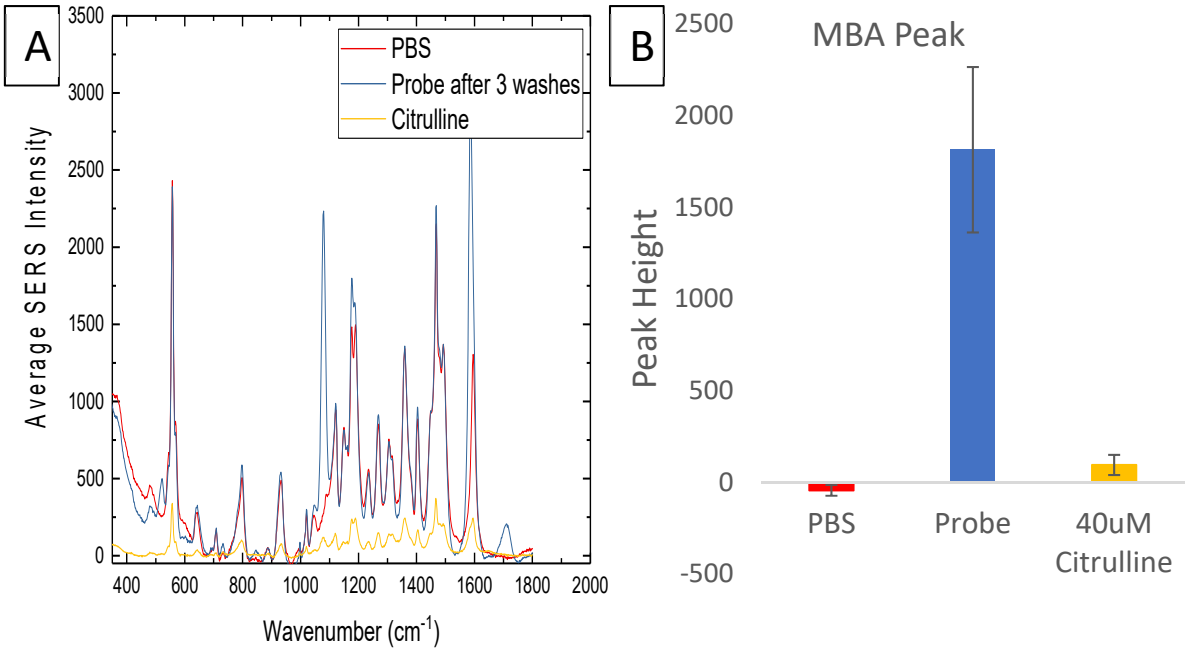

Figure 21: Competitive Binding SERS Data and Bar Graph with Error Bars of Competitive Binding Experiments. a) Shows the SERS signal with just PBS, then after the probe was added and washed 3 times, then the SERS signal after free citrulline was introduced. b) Shows a bar graph with error bars of the SERS signal with just PBS, probe, and after 40µM of citrulline was added

IV.4 Citrulline aptamer SERRS sensor

Another citrulline sensor was developed that uses surface enhanced resonant Raman spectroscopy (SERRS) in a microwell. This approach puts the aptamers directly on the nanocubes via the thiol group on them. The Cy5 on the other end of the aptamers acted as a RRM. As the free citrulline is introduced, the aptamers unwind to bind to the free citrulline. As this occurs, the Cy5 signal decreases due to the further distance the fluorophore is from the metallic surface, as shown in figure 23.

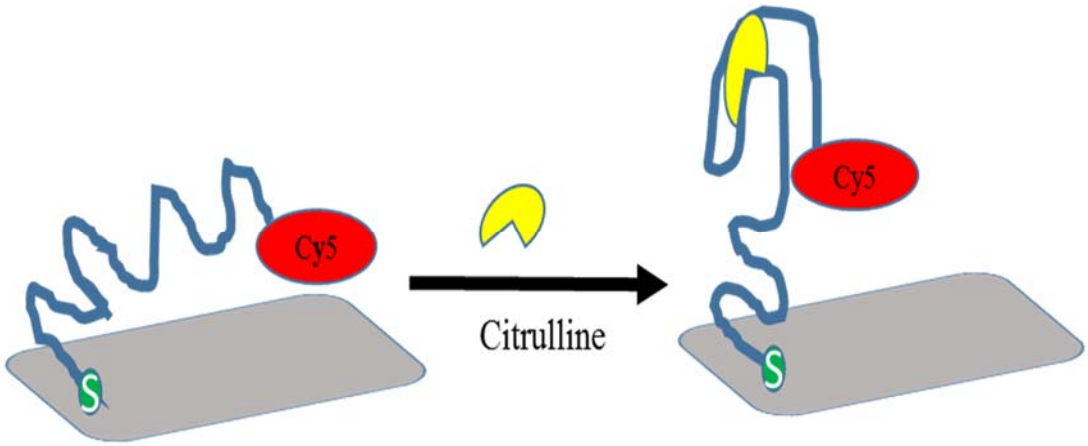

Figure 22: Schematic Diagram of SERRS Sensor. Shows a schematic diagram of the functionalized nanoparticles for the SERRS sensor. As free citrulline is introduced the aptamer unfolds and the Cy5 moves away from the surface of the nanocube.

Although fluorescence data was not taken, it is expected that as the SERRS signal decreases and as free citrulline is introduced to the fluorescent signal from the Cy5, it will increase due to the distance the fluorophore is from the broad absorption from the nanocubes. Preliminary data looks good as shown in figure 23. As the concentration of free citrulline increases, the SERRS signal starts to decrease.

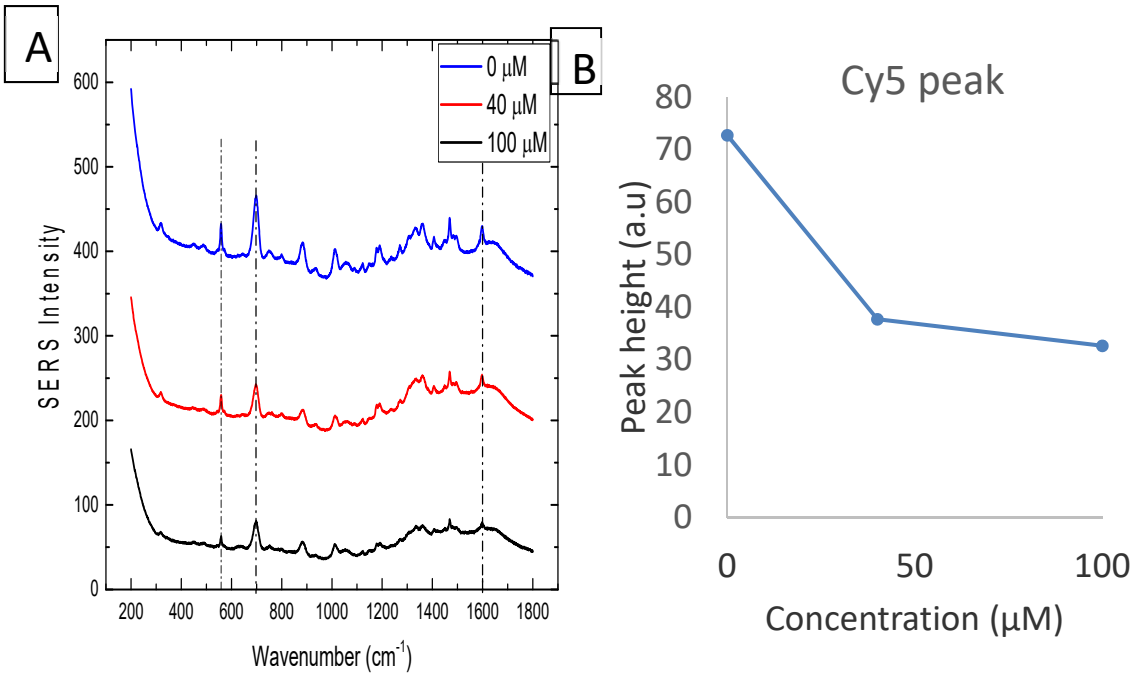

Figure 23: SERRS Data with Respect to Concentration. a) Shows the SERRS signal from the nanocubes with different concentrations of free citrulline introduced into the microwell b) Shows the sensitivity of the system by monitoring a Cy5 peak with

CHAPTER V

CONCLUSION

To make a POC SERS sensor, we started by finding the nanoparticle that would be the best for our future experiments. After determining the correct nanoparticle, ag nanocubes, we then functionalized the nanoparticle with a RRM and citrulline via a PEG linker. At the same time citrulline specific aptamers were developed. Lastly, we made two sensors, a competitive binding sensor using an Ag substrate and also aptamer based Ag nanocube SERRS sensor. Both sensors show promise and should be analyzed further in various mediums.

REFERENCES

1. H. P. Ioannou et al., "Plasma citrulline levels in paediatric patients with celiac disease and the effect of a gluten-free diet," *European journal of gastroenterology & hepatology* **23**(3), 245-249 (2011).
2. G. Gondolesi et al., "The value of plasma citrulline to predict mucosal injury in intestinal allografts," *American journal of transplantation* **6**(11), 2786-2790 (2006).
3. E. Honsova et al., "Plasma citrulline levels and acute cellular rejection early after small bowel transplantation in pigs," *Veterinarni Medicina* **54**(5), 215-222 (2009).
4. S. Keith, E. Murray, and W. Spoo, "Toxicological profile for ionizing radiation," *Atlanta, GA: Agency for Toxic Substances and Disease Registry. US Public Health Service, Department of Health and Human Services* 1-396 (1999).
5. I. A. f. R. o. Cancer, "Volume 75: Ionizing Radiation, Part 1: X-and Gamma (g)-Radiation, and Neutrons," *IARC Monographs on the Evaluation of Carcinogenic Risks to Humans* (2000).
6. F. El Ghissassi et al., "A review of human carcinogens—part D: radiation," *The lancet oncology* **10**(8), 751-752 (2009).
7. N. R. Council, *Health Effects of Exposure to Low Levels of Ionizing Radiation: BEIR V*, The National Academies Press, Washington, DC (1990).

8. W. F. Blakely, C. A. Salter, and P. G. Prasanna, "Early-response biological dosimetry--recommended countermeasure enhancements for mass-casualty radiological incidents and terrorism," *Health physics* **89**(5), 494-504 (2005).

9. E. Curis et al., "Almost all about citrulline in mammals," *Amino acids* **29**(3), 177 (2005).

10. G. Piton et al., "Acute intestinal failure in critically ill patients: is plasma citrulline the right marker?," *Intensive care medicine* **37**(6), 911-917 (2011).

11. A. Tizianello et al., "Renal metabolism of amino acids and ammonia in subjects with normal renal function and in patients with chronic renal insufficiency," *Journal of Clinical Investigation* **65**(5), 1162 (1980).

12. L. Lutgens, "Biomarkers for radiation-induced small bowel epithelial damage: An emerging role for plasma Citrulline," *World Journal of Gastroenterology* **13**(22), 3033-3042 (2007).

13. P. Crenn et al., "Plasma citrulline is a biomarker of enterocyte mass and an indicator of parenteral nutrition in HIV-infected patients," *Am J Clin Nutr* **90**(3), 587-594 (2009).

14. G. Gondolesi et al., "Serum citrulline is a potential marker for rejection of intestinal allografts," *Transplantation proceedings* 918-920 (2002).

15. G. E. Gondolesi et al., "Defining normal plasma citrulline in intestinal transplant recipients," *American Journal of Transplantation* **4**(3), 414-418 (2004).

16. P. A. Pappas et al., "An analysis of the association between serum citrulline and acute rejection among 26 recipients of intestinal transplant," *American Journal of Transplantation* **4**(7), 1124-1132 (2004).

17. P. A. Pappas et al., "Serum citrulline and rejection in small bowel transplantation: a preliminary report," *Transplantation* **72**(7), 1212-1216 (2001).

18. A. David et al., "An association of lower serum citrulline levels within 30 days of acute rejection in patients following small intestine transplantation," *Transplantation proceedings* 1731-1732 (2006).

19. H. M. van Eijk, D. R. Rooyakkers, and N. E. Deutz, "Rapid routine determination of amino acids in plasma by high-performance liquid chromatography with a 2-3 microns Spherisorb ODS II column," *Journal of chromatography* **620**(1), 143-148 (1993).

20. H. Van Eijk et al., "Influence of storage conditions on normal plasma amino-acid concentrations," *Clinical Nutrition* **13**(6), 374-380 (1994).

21. H. M. van Eijk et al., "Determination of amino acid isotope enrichment using liquid chromatography-mass spectrometry," *Analytical biochemistry* **271**(1), 8-17 (1999).

22. H. M. van Eijk et al., "Measurement of amino acid isotope enrichment by liquid chromatography mass spectroscopy after derivatization with 9-fluorenylmethylchloroformate," *Journal of chromatography. B, Analytical technologies in the biomedical and life sciences* **856**(1-2), 48-56 (2007).

23. M. P. Engelen et al., "Stimulated nitric oxide production and arginine deficiency in children with cystic fibrosis with nutritional failure," *The Journal of pediatrics* **163**(2), 369-375 (2013).

24. C. Tuerk, and L. Gold, "Systematic evolution of ligands by exponential enrichment: RNA ligands to bacteriophage T4 DNA polymerase," *Science* **249**(4968), 505-510 (1990).

25. A. D. Ellington, and J. W. Szostak, "In vitro selection of RNA molecules that bind specific ligands," *nature* **346**(6287), 818-822 (1990).

26. J. F. Lee et al., "Aptamer database," *Nucleic acids research* **32**(suppl 1), D95-D100 (2004).

27. C. Srisawat, and D. R. Engelke, "Streptavidin aptamers: affinity tags for the study of RNAs and ribonucleoproteins," *Rna* **7**(4), 632-641 (2001).

28. J. Ruckman et al., "2′-Fluoropyrimidine RNA-based aptamers to the 165-amino acid form of vascular endothelial growth factor (VEGF165) Inhibition of receptor binding and VEGF-induced vascular permeability through interactions requiring the exon 7-encoded domain," *Journal of Biological Chemistry* **273**(32), 20556-20567 (1998).

29. S. D. Jayasena, "Aptamers: An emerging class of molecules that rival antibodies in diagnostics," *Clinical Chemistry* **45**(9), 1628-1650 (1999).

30. P. L. Sazani, R. Larralde, and J. W. Szostak, "A small aptamer with strong and specific recognition of the triphosphate of ATP," *Journal of the American Chemical Society* **126**(27), 8370-8371 (2004).

31. J. R. Babendure, S. R. Adams, and R. Y. Tsien, "Aptamers switch on fluorescence of triphenylmethane dyes," *Journal of the American Chemical Society* **125**(48), 14716-14717 (2003).

32. I. Hirao et al., "In vitro selection of aptamers that bind to ribosome-inactivating toxins," *Nucleic acids symposium series* 283-284 (1996).

33. J. Liu, and Y. Lu, "Fast colorimetric sensing of adenosine and cocaine based on a general sensor design involving aptamers and nanoparticles," *Angewandte Chemie* **118**(1), 96-100 (2006).

34. T. C. Chu et al., "Aptamer: toxin conjugates that specifically target prostate tumor cells," *Cancer research* **66**(12), 5989-5992 (2006).

35. D. P. Wernette, "Functional-DNA-based nanoscale materials and devices for sensing trace contaminants in water," *MRS bulletin* **33**(1), 34-41 (2008).

36. C. B. Swearingen et al., "Immobilization of a catalytic DNA molecular beacon on Au for Pb (II) detection," *Analytical chemistry* **77**(2), 442-448 (2005).

37. R. Stoltenburg, C. Reinemann, and B. Strehlitz, "SELEX—a (r) evolutionary method to generate high-affinity nucleic acid ligands," *Biomolecular engineering* **24**(4), 381-403 (2007).

38. M. Famulok, "Molecular recognition of amino acids by RNA-aptamers: an L-citrulline binding RNA motif and its evolution into an L-arginine binder," *Journal of the American Chemical Society* **116**(5), 1698-1706 (1994).

39. K. C. Bantz et al., "Recent progress in SERS biosensing," *Phys Chem Chem Phys* **13**(24), 11551-11567 (2011).

40. C. Raman, and K. Krishnan, "hν o hν," *Nature* **121**(501 (1928).

41. R. L. McCreery, *Raman spectroscopy for chemical analysis*, John Wiley & Sons (2005).

42. R. Singh, "CV Raman and the Discovery of the Raman Effect," *Physics in Perspective* **4**(4), 399-420 (2002).

43. B. Sharma et al., "SERS: Materials, applications, and the future," *Materials today* **15**(1-2), 16-25 (2012).

44. J. P. Camden et al., "Probing the structure of single-molecule surface-enhanced Raman scattering hot spots," *Journal of the American Chemical Society* **130**(38), 12616 (2008).

45. B. Walton, and G. Coté, "Comparing surface enhanced Raman spectroscopy from colloidal gold nanoparticles and nanocages," *SPIE BiOS* 93320C-93320C-93310 (2015).

46. G. C. Schatz, M. A. Young, and R. P. Van Duyne, "Electromagnetic mechanism of SERS," in *Surface-enhanced Raman scattering*, pp. 19-45, Springer (2006).

47. P. Kambhampati, M. C. Foster, and A. Campion, "Two-dimensional localization of adsorbate/substrate charge-transfer excited states of molecules adsorbed on metal surfaces," *The Journal of chemical physics* **110**(1), 551-558 (1999).

48. A. J. Haes et al., "Plasmonic materials for surface-enhanced sensing and spectroscopy," *MRS bulletin* **30**(05), 368-375 (2005).

49. D. L. Jeanmaire, and R. P. Van Duyne, "Surface Raman spectroelectrochemistry: Part I. Heterocyclic, aromatic, and aliphatic amines adsorbed on the anodized

silver electrode," *Journal of Electroanalytical Chemistry and Interfacial Electrochemistry* **84**(1), 1-20 (1977).

50. R. Aroca, *Surface-enhanced vibrational spectroscopy*, John Wiley & Sons (2006).

51. S. Abalde-Cela et al., "Surface-enhanced Raman scattering biomedical applications of plasmonic colloidal particles," *J R Soc Interface* **7**(SUPPL. 4), S435-450 (2010).

52. B. Walton et al., "Use of a micro- to nanochannel for the characterization of surface-enhanced Raman spectroscopy signals from unique functionalized nanoparticles," *Journal of biomedical optics* **21**(8), 085006 (2016).

53. M. Li et al., "Plasmonic nanorice antenna on triangle nanoarray for surface-enhanced Raman scattering detection of hepatitis B virus DNA," *Analytical chemistry* **85**(4), 2072-2078 (2013).

54. H. Hwang et al., "In situ dynamic measurements of the enhanced SERS signal using an optoelectrofluidic SERS platform," *Lab on a Chip* **11**(15), 2518-2525 (2011).

55. H. Hwang et al., "In situ dynamic measurements of the enhanced SERS signal using an optoelectrofluidic SERS platform," *Lab Chip* **11**(15), 2518-2525 (2011).

56. A. F. Chrimes et al., "Dielectrophoresis–Raman spectroscopy system for analysing suspended nanoparticles," *Lab on a Chip* **11**(5), 921-928 (2011).

57. J. Zhou et al., "Convenient formation of nanoparticle aggregates on microfluidic chips for highly sensitive SERS detection of biomolecules," *Analytical and bioanalytical chemistry* **402**(4), 1601-1609 (2012).

58. M. Wang et al., "Optofluidic device for ultra-sensitive detection of proteins using surface-enhanced Raman spectroscopy," *Microfluidics and Nanofluidics* **6**(3), 411-417 (2009).

59. J. Chen et al., "Gold Nanocages: Engineering Their Structure for Biomedical Applications," *Advanced materials* **17**(18), 2255-2261 (2005).

60. J. D. Weatherston, N. C. Worstell, and H. J. Wu, "Quantitative surface-enhanced Raman spectroscopy for kinetic analysis of aldol condensation using Ag-Au core-shell nanocubes," *Analyst* **141**(21), 6051-6060 (2016).

61. S. Abdali et al., "Resonance surface enhanced Raman optical activity of myoglobin as a result of optimized resonance surface enhanced Raman scattering conditions," *Journal of Physics: Condensed Matter* **19**(28), 285205 (2007).

62. F. Liu et al., "Surface-enhanced Raman scattering study of riboflavin on borohydride-reduced silver colloids: Dependence of concentration, halide anions and pH values," *Spectrochimica Acta Part A: Molecular and Biomolecular Spectroscopy* **85**(1), 111-119 (2012).

63. N. Halas, "Playing with plasmons: tuning the optical resonant properties of metallic nanoshells," *Mrs Bulletin* **30**(05), 362-367 (2005).

64. N. C. Worstell et al., "Binding Cooperativity Matters: A GM1-Like Ganglioside-Cholera Toxin B Subunit Binding Study Using a Nanocube-Based Lipid Bilayer Array," *PLoS One* **11**(4), e0153265 (2016).

65. E. Le Ru, C. Galloway, and P. Etchegoin, "On the connection between optical absorption/extinction and SERS enhancements," *Physical Chemistry Chemical Physics* **8**(26), 3083-3087 (2006).

66. B. Walton et al., "Use of a micro- to nanochannel for the characterization of surface-enhanced Raman spectroscopy signals from unique functionalized nanoparticles," *Journal of biomedical optics* **21**(8), 085006 (2016).

67. M. N. Hamblin et al., "Selective trapping and concentration of nanoparticles and viruses in dual-height nanofluidic channels," *Lab on a Chip* **10**(2), 173-178 (2010).

68. M. Wang et al., "Optofluidic device for ultra-sensitive detection of proteins using surface-enhanced Raman spectroscopy," *Microfluidics and Nanofluidics* **6**(3), 411-417 (2009).

69. B. S. C. Schmiege, CA, US), Ingle, Nitin K. (Santa Clara, CA, US), Nemani, Srinivas D. (Sunnyvale, CA, US), Anthis, Jeffrey W. (San Jose, CA, US), Wang, Xikun (Sunnyvale, CA, US), Liu, Jie (Sunnyvale, CA, US), Benjaminson, David (Santa Clara, CA, US), "Methods Of Etching Films With Reduced Surface Roughness," Applied Materials, Inc., United States (2016).

70. S. Abalde-Cela et al., "Surface-enhanced Raman scattering biomedical applications of plasmonic colloidal particles," *J R Soc Interface* **7**(SUPPL. 4), S435-450 (2010).

71. D. Radziuk, and H. Moehwald, "Highly effective hot spots for SERS signatures of live fibroblasts," *Nanoscale* **6**(11), 6115-6126 (2014).

72. N. D. Israelsen, C. Hanson, and E. Vargis, "Nanoparticle properties and synthesis effects on surface-enhanced Raman scattering enhancement factor: an introduction," *The Scientific World Journal* **2015**((2015).

73. L. Tian, N. Gandra, and S. Singamaneni, "Monitoring controlled release of payload from gold nanocages using surface enhanced Raman scattering," *ACS nano* **7**(5), 4252-4260 (2013).

74. B. Walton, and G. Coté, "Comparing surface enhanced Raman spectroscopy from colloidal gold nanoparticles and nanocages," *SPIE BiOS* 93320C-93320C-93310 (2015).

75. C. B. J. Creighton, M. Albrecht, "Plasma resonance enhancement of raman scattering by pyridine adsorbed on silver or gold sol particles of size comparable to the excitation wavelength," *Journal of the Chemical Society, Faraday Transactions 2: Molecular and Chemical Physics* 12), (1978).

76. N. R. Jana, and T. Pal, "Anisotropic Metal Nanoparticles for Use as Surface-Enhanced Raman Substrates," *Advanced Materials* **19**(13), 1761-1765 (2007).

77. C. M. Cobley et al., "Shape-controlled synthesis of silver nanoparticles for plasmonic and sensing applications," *Plasmonics* **4**(2), 171-179 (2009).

78. C. L. Nehl, H. Liao, and J. H. Hafner, "Optical properties of star-shaped gold nanoparticles," *Nano letters* **6**(4), 683-688 (2006).

79. A. Kandakkathara, I. Utkin, and R. Fedosejevs, "Surface-enhanced raman scattering (SERS) detection of low concentrations of tryptophan amino acid in silver colloid," *Applied spectroscopy* **65**(5), 507-513 (2011).

80. I. Larmour, K. Faulds, and D. Graham, "SERS activity and stability of the most frequently used silver colloids," *Journal of Raman Spectroscopy* **43**(2), 202-206 (2012).

81. T. Makiabadi et al., "Preparation, Optimization, and Characterization of SERS Sensor Substrates Based on Two-Dimensional Structures of Gold Colloid," *Plasmonics* **5**(1), 21-29 (2009).

82. R. Stiufiuc et al., "SERS-active silver colloids prepared by reduction of silver nitrate with short-chain polyethylene glycol," *Nanoscale research letters* **8**(1), 1-5 (2013).

83. E. Tourwé, K. Baert, and A. Hubin, "Surface-enhanced Raman scattering (SERS) of phthalic acid and 4-methyl phthalic acid on silver colloids as a function of pH," *Vibrational spectroscopy* **40**(1), 25-32 (2006).

84. N. R. Yaffe, and E. W. Blanch, "Effects and anomalies that can occur in SERS spectra of biological molecules when using a wide range of aggregating agents for hydroxylamine-reduced and citrate-reduced silver colloids," *Vibrational Spectroscopy* **48**(2), 196-201 (2008).

85. C.-H. T. Hong Xu, Thomas Vickers, Charles Mann, Joseph Schlenoff, "Near-Infrared surface-enhanced Raman spectroscopy of chemisorbed compounds on gold colloids " *Surface Science* **311**(3), L707-L711 (1994).

86. S. Zong et al., "A multiplex and straightforward aqueous phase immunoassay protocol through the combination of SERS-fluorescence dual mode nanoprobes and magnetic nanobeads," *Biosensors & bioelectronics* **41**(745-751 (2013).

87. D. Wu, and Y. Fang, "The adsorption behavior of p-hydroxybenzoic acid on a silver-coated filter paper by surface enhanced Raman scattering," *Journal of Colloid and Interface Science* **265**(2), 234-238 (2003).

88. L. Tong et al., "Optical aggregation of metal nanoparticles in a microfluidic channel for surface-enhanced Raman scattering analysis," *Lab Chip* **9**(2), 193-195 (2009).

89. M. Wang et al., "An optofluidic device for surface enhanced Raman spectroscopy," *Lab Chip* **7**(5), 630-632 (2007).

90. S. S. G. Pavan Kumar, B. Vibha, B. Ashok Reddy, Tapas Kundu, Chandrabhas Narayana, "Hot Spots in Ag Core−Au Shell Nanoparticles Potent for Surface-Enhanced Raman Scattering Studies of Biomolecules," *journal of physical chemistry. C* **111**(11), 4388-4392 (2007).

91. L. R. Hirsch et al., "Metal nanoshells," *Annals of biomedical engineering* **34**(1), 15-22 (2006).

92. Y. X. Ke Zhang, Xiaochun Wu, Lili Feng, Weiwei He, Jianbo Liu, Weiya Zhou, Sishen Xie, "Enhanced Optical Responses of Au@Pd Core/Shell Nanobars," *Langmuir* **25**(2), 1162-1168 (2009).

93. P. G.-S. Mingzhao Liu, "Synthesis and Optical Characterization of Au/Ag Core/Shell Nanorods," *J. Phys. Chem. B* **108**(19), 5882-5888 (2004).

94. S. W. Steven Oldenburg, Richard Averitt, Naomi Halas, "Surface enhanced Raman scattering in the near infrared using metal nanoshell substrates " *Journal of chemical physics* **111**(10), 4729-4735 (1999).

95. U. Tamer et al., "Fabrication of magnetic gold nanorod particles for immunomagnetic separation and SERS application," *Journal of Nanoparticle Research* **13**(8), 3167-3176 (2011).

96. B. R. Yan Cui, Jian-Lin Yao, Ren-Ao Gu, Zhong-Qun Tian, "Synthesis of AgcoreAushellBimetallic Nanoparticles for Immunoassay Based on Surface-Enhanced Raman Spectroscopy," *Journal of physical chemistry B* **110**(9), 4002-4006 (2006).

97. C. M. Cobley, and Y. Xia, "Engineering the Properties of Metal Nanostructures via Galvanic Replacement Reactions," *Materials science & engineering. R, Reports : a review journal* **70**(3-6), 44-62 (2010).

98. Y. Xia et al., "Galvanic replacement reaction: a simple and powerful route to hollow and porous metal nanostructures," *Proceedings of the Institution of Mechanical Engineers, Part N: Journal of Nanoengineering and Nanosystems* **221**(1), 1-16 (2007).

99. F. S. Jingyi Chen, Benjamin Wiley, Hu Chang, Michael Cobb, Zhi-Yuan Li, Lesli Au, Hui Zhang, Michael Kimmey, Xingde Li, Younan Xia, "Gold Nanocages: Bioconjugation and Their Potential Use as Optical Imaging Contrast Agents," *Nano Letters* **5**(3), 473-477 (2005).

100. B. S. M. A. Mahmoud, M. A. El-Sayed, "Surface Plasmon Fields and Coupling in the Hollow Gold Nanoparticles and Surface-Enhanced Raman Spectroscopy. Theory and Experiment," *J. Phys. Chem. C* **114**(7436-7443 (2010).

APPENDIX A

COMPARISON OF NANOPARTICLE MORPHOLOGIES[9][10]

A.1 Various Ways to Affect SERS Signal

Size, composition, and morphology of the materials used for SERS can be tuned and optimized.(45, 51, 75, 76) For example, nanostars, nanocubes, nanosphers, and nanobars have been engineered to have a unique effect on the Raman scattered light.(77, 78) Gold and silver colloids have been analyzed using different preparation methods, concentration, and sizes of analyte attached to the nanoparticle.(79-83) For 60nm gold colloid, the absorption band is around 520nm; therefore, the laser choice needs to be around 520nm to maximally enhance the signal, which is not an ideal wavelength for future experiments using blood. For gold, the extinction coefficient can be shifted, however, to the near infrared region by aggregation. As mentioned above, this can be achieved using NaCl via chemical aggregation, and it can also be accomplished using elements that have a negative charge which attracts the positive surface charge on gold nanoparticles.(61, 62, 84) Using NaCl, however, is not a repeatable method due to various size aggregates that can form causing variations in the SERS signal, and aggregation only lasts for a small period of time before the aggregates are so large that

---

[9]Reprinted with permission from "Use of a micro-to nanochannel for the characterization of surface-enhanced Raman spectroscopy signals from unique functionalized nanoparticles" by Brian M. Walton et. al., 2016. Vol. 9715, Copyright 2016. Society of Photo Optical Instrumentation Engineers.

[10]Reprinted with permission from "Comparing Surface Enhanced Raman Spectroscopy from Colloidal Gold Nanoparticles and Nanocages" by B. M. Walton and G.L. Cote, 2015. Vol. 9332, Copyright 2015. Optical Diagnostics and Sensing XV: Toward Point-of-Care Diagnostics.

they fall out of solution.(84, 85) Also mentioned above, other methods make the nanoparticles aggregate include nanochannels, filters, or magnets causing the particles to mechanically aggregate together.(86-89) An alternative to aggregation involves colloidal systems that do not require chemical or mechanical aggregation to achieve maximum SERS enhancement, because they can be engineered to have their extinction coefficients in tune with the excitation wavelength. Nanorods and nanoshells have dielectric cores and are surrounded by a metal shell like gold or silver. Those nanoparticles optical properties are tuned depending on the composition and size of the core/shell ratio.(63, 90-96) Another nanoparticle that can be tuned is nanocages; their optical properties are controlled by the molar ratio between the silver template and chloroauric acid ($HAuCl_4$) when making the nanocages.(59, 97, 98)

The tunable colloidal systems, such as the engineered nanocages, have the potential to produce a repeatable SERS signal without the reproducibility issues that occur from the chemical aggregation utilized traditionally with gold colloid. The following presents the first analysis and comparison of the nanocages to the standard spherical gold colloid in an effort to assess their potential for a repeatable SERS POC device.

A.2 Nanocage/Gold colloid and BDT sample preparation

Using a galvanic reduction method, the 60nm nanocages were prepared and obtained from the Xia group at Washington University. A detailed description of how to prepare the nanocages can be found here.(59) To summarize, the nanocages are formed using an Ag nanoparticle template. $HAuCl_4$ is added to a solution of Ag nanoparticles

which causes the galvanic reduction to occur. The shape of the nanoparticle comes from the shape of the Ag template; the templates can be engineered to be various shapes.(99) The extinction wavelength can be for nanocages can be tuned from 500nm to 1200nm based on the molar ratio of the $HAuCl_4$ to Ag. The 10nM stock concentration of nanocages were diluted to 147pM concentration to match the stock gold colloid concentration. 35ml of 200 proof ethanol was mixed with 5mg of BDT powder and sonicated for 5 minutes, yielding a 1mM BDT/ethanol solution. From the initial stock solution, another dilution was performed by adding deionized water yielding a final BDT concentration of 231µM. 30µl of nanocages was mixed with 30µl of BDT/ethanol and vortexed for approximately 20 seconds. SERS spectra were collected immediately following the vortex. 231µM BDT/ethanol solution is mixed with 60nm, 147pm, gold colloid (Polysciences Inc.) 30µl of gold colloid was vortexed with 30µl of 231µM BDT/ethanol solution for approximately 20 seconds. Following vortexing, SERS experiments were performed immediately.

A.3 Raman system and sample preparation

All Raman and SERS spectra were collected using a Thermo Scientific DXR Raman confocal microscope. The samples were excited with a 780 ± 0.2nm diode laser with a 24mW laser power through an Olympus 10x microscope objective configured with an 1800 grooves/mm grating. A 35µl-384 low volume sample holder was used from Corning. The samples were exposed with an integration time of 5 seconds 60 times for a total of 300 seconds.

A.4 Scanning electronic microscope (SEM) and transmission electronic microscope (TEM) morphological imaging

To show the morphology of the nanoparticles SEM and TEM images were taken as depicted in Figure 24. Gold colloid SEM images are depicted in Figure 24(a); they are spherical in shape and are 60nm in diameter with a TEM image inset showing a higher resolution blown up of the particles. The higher density of each of the nanoparticles compared to the hollow nanocages is illustrated in the inset. Figure 24(b) shows TEM images of the nanocages in high resolution in the inset and SEM image of them. The 60nm diameter nanocages are hollow nanoparticles. In addition to being hollow, the nanocages have the shape of a cube, unlike the spherical gold. To help illustrate the hollowness and porosity of the nanocages we used TEM images. The sharp edges and hollowness on the nanocages also are known to create hot spots which generate large SERS signals inside the nanocage and on the corners.(100)

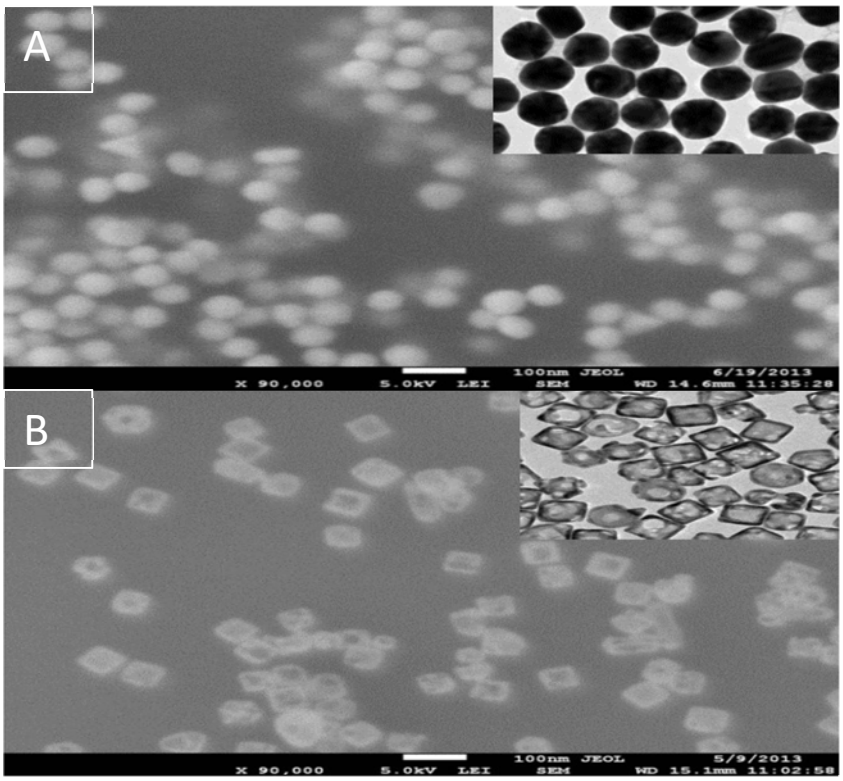

Figure 24: SEM Images of Gold Colloid and Nanocages. (a) SEM image of gold colloid with blown up TEM image (inset) (b) SEM image of nanocages with a blown up TEM image (inset). Reprinted with permission from B.M. Walton and G. L. Cote 2015.

A.5 Particle sizing

A nanosight system was used to show the average particle size, concentration, and particle distribution for gold and nanocages in colloid without the benzenedithiol (BDT) and with the BDT. Figure 25 shows that the nanoparticles used have the same concentration and size. Analyzing the figure also illustrates that with the addition of BDT, some minor aggregation begins to occur. This was found to be due to the two thiol groups BDT has, which form bonds to the nanoparticles; hydrogen is displaced and the sulfur has a strong binding affinity to the metal surface creating the strong bond. The average particle sizes of nanocages and gold colloid range from 72nm to 63nm and

62nm, respectively. For gold, the particles/ml decreases because as more nanoparticles attach to form small aggregates, the number of free particles in solution decreases. Some of the difference in size is due to inhomogeneity in the sample.

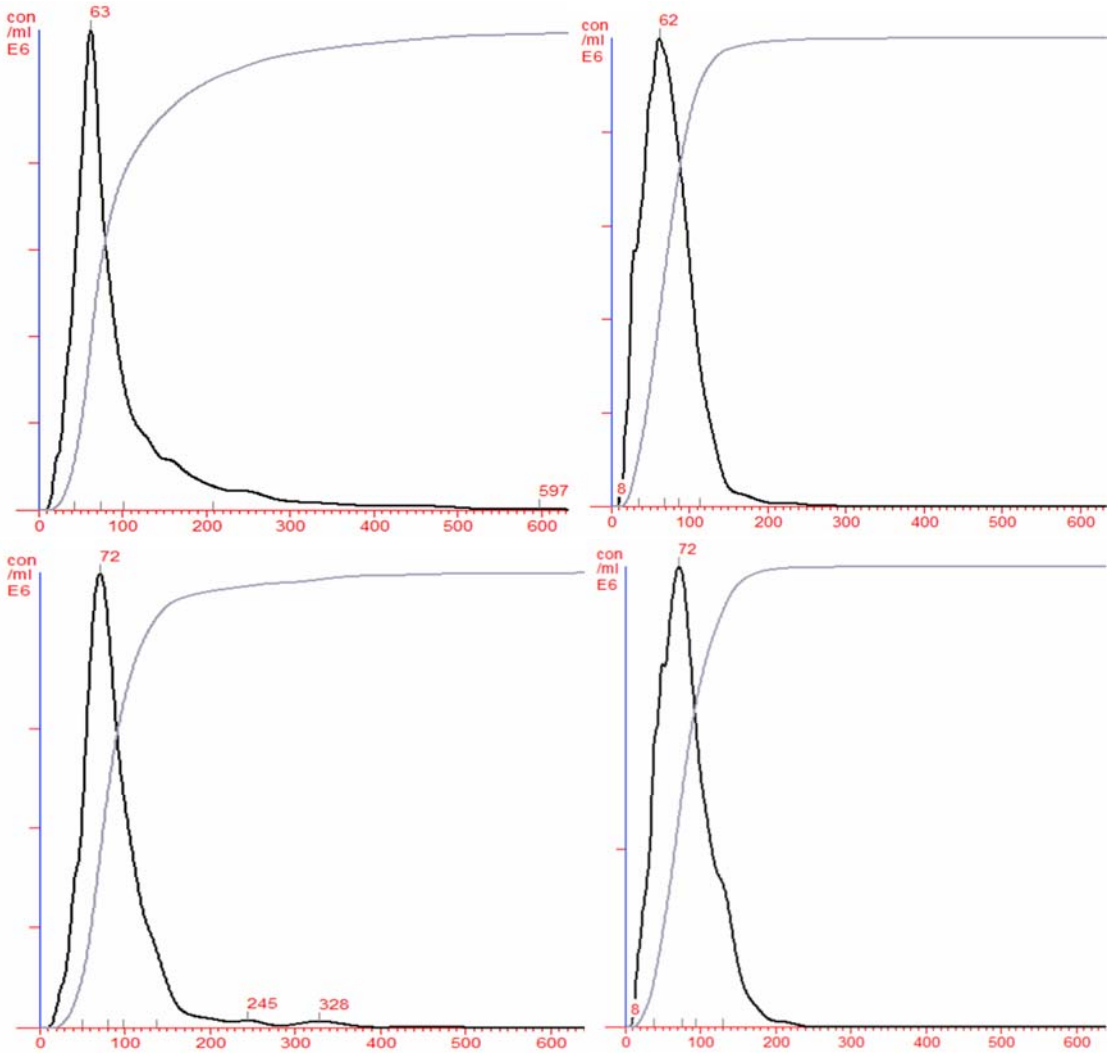

Figure 25: Particle Distributions and Concentrations of Particles/ml. It shows the particle distributions and concentrations of the particles/ml using the Nanosight. (a) shows a gold colloid concentration of 3.46E8 particles/ml and the size distribution with average particle size of 63nm. (b) shows the nanocage concentration of 3.68E8 particles/ml and the size distribution with an average particle size of 62nm (c) shows the gold colloid with 115µM BDT covalently bonded to the surface had a concentration of 2.89E8 particles/ml and average particle size of 72nm (d) shows the nanocages with 115µM BDT covalently bonded to the surface had a concentration of 2.02E8 particles/ml and average particle size of 72nm. Reprinted with permission from B.M. Walton and G.L. Cote 2015.

A.6 UV-VIS Spectrometer

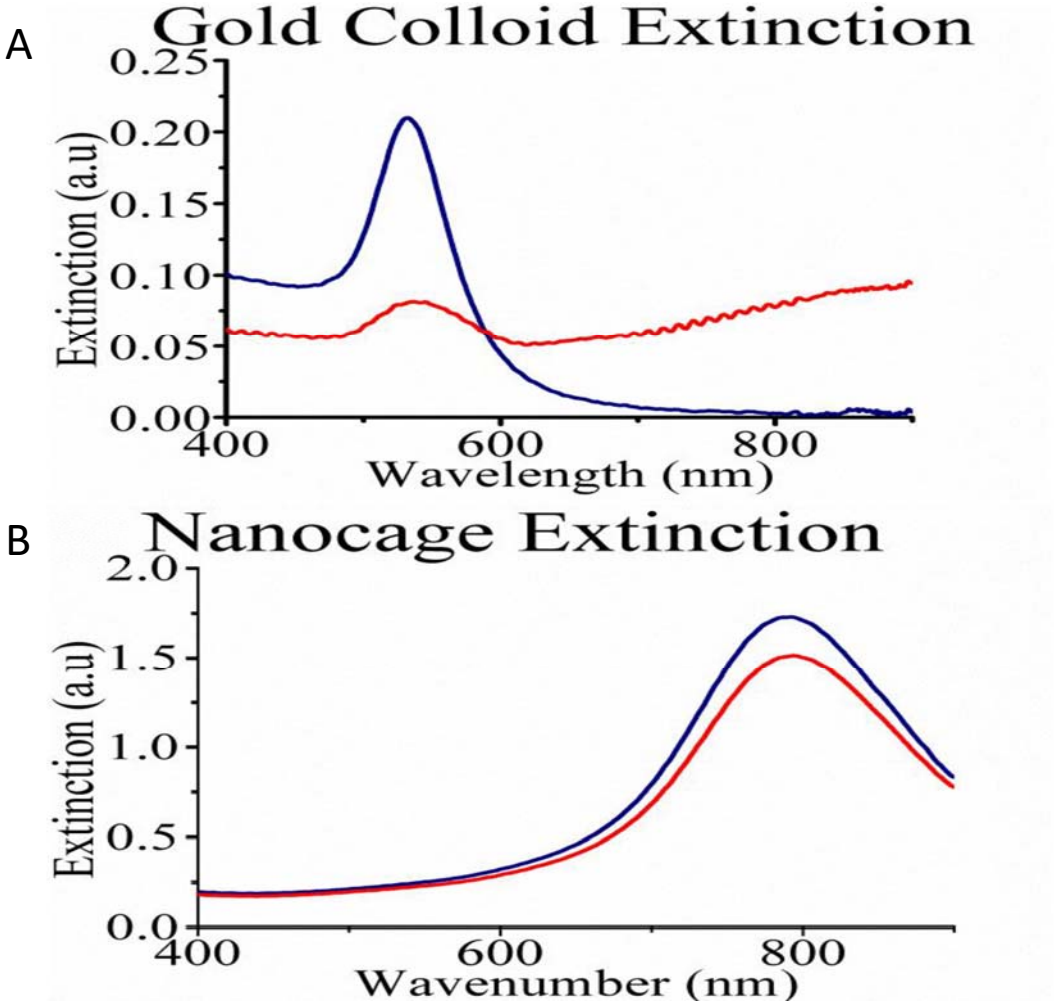

Figure 26: Gold Colloid and Nanocage Extinctions. (a) shows the extinction spectra of gold colloid (blue line) and the extinction spectra after the addition of 0.5M NaCl (red line). (b) shows the extinction spectra of nanocages (blue line) and the extinction spectra after the addition of 0.5M NaCl (red line) shift the wavelength peak. Reprinted with permission from B.M. Walton and G.L. Cote 2015.

The extinction spectra of nanocages and gold colloid before and after the addition of NaCl is depicted in Figure 26. The blue line shown in Figure 26a shows the extinction spectra of gold colloid with a maximum peak around 532nm, followed by a

sharp decline, as expected. The shifted extinction spectrum that occurs after NaCl is added is shown by the red line. Figure 26b illustrates the extinction spectra of the nanocages. The nanocages are engineered and tuned to 785nm which is in resonance with the excitation laser and the addition of NaCl doesn't shift the wavelength peak.

A.7 Raman/SERS

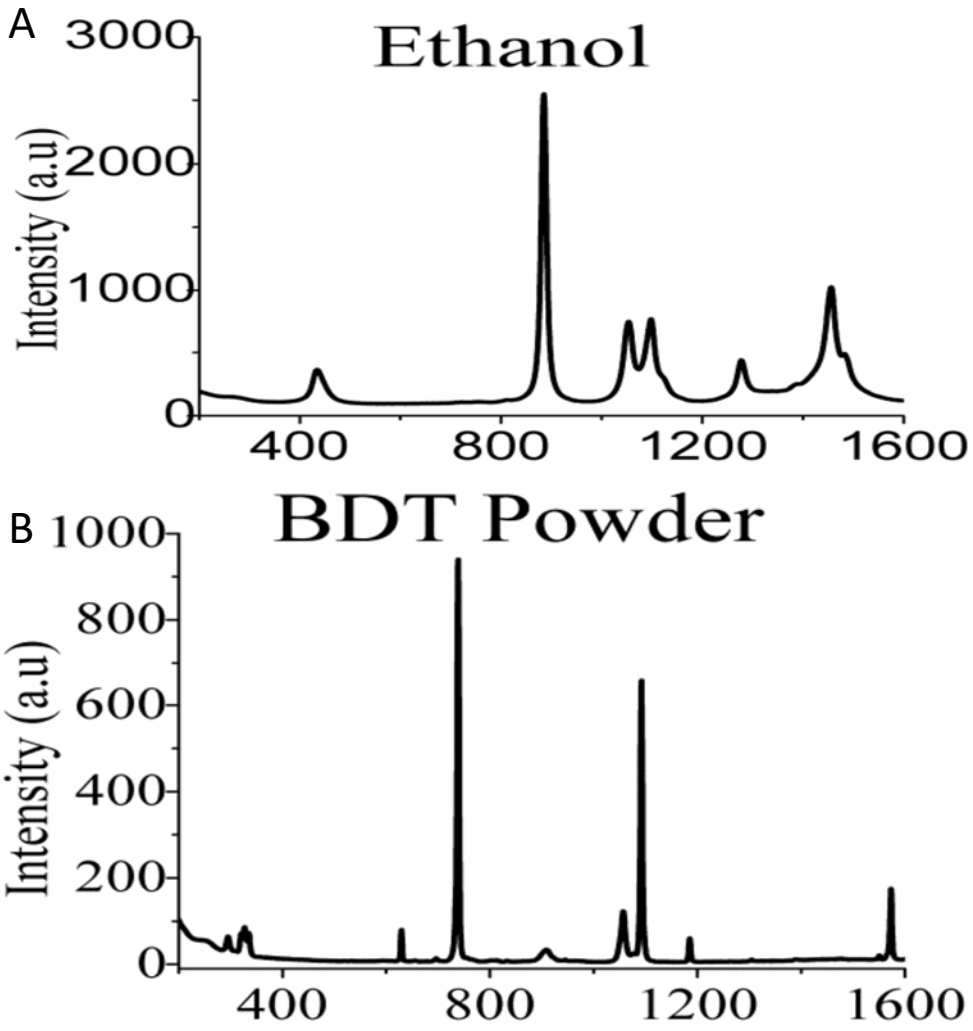

Figure 27: Raman Spectra of Ethanol and BDT Powder. (a) shows Raman spectra of BDT powder (b) shows Raman spectra of ethanol for comparison purposes. Reprinted with permission from B.M. Walton and G.L. Cote 2015.

Raman spectra were collected from a solution of ethanol and BDT powder (a strong Raman active molecule) which is depicted in Figure 27a and b, respectively. The data show that both ethanol and BDT are Raman active. The data were then used to determine if any overlap between BDT and the ethanol peaks are present when the two are combined. Figure 27 specifically shows multiple BDT peaks are influenced by ethanol, and, thus, only the BDT peaks that are independent of ethanol were used in the study. SERS spectra of gold bonded to 115µM BDT via the thiol groups at time zero and the spectra with respect to time after the addition of 7µl of 0.5M NaCl is shown in Figure 28.

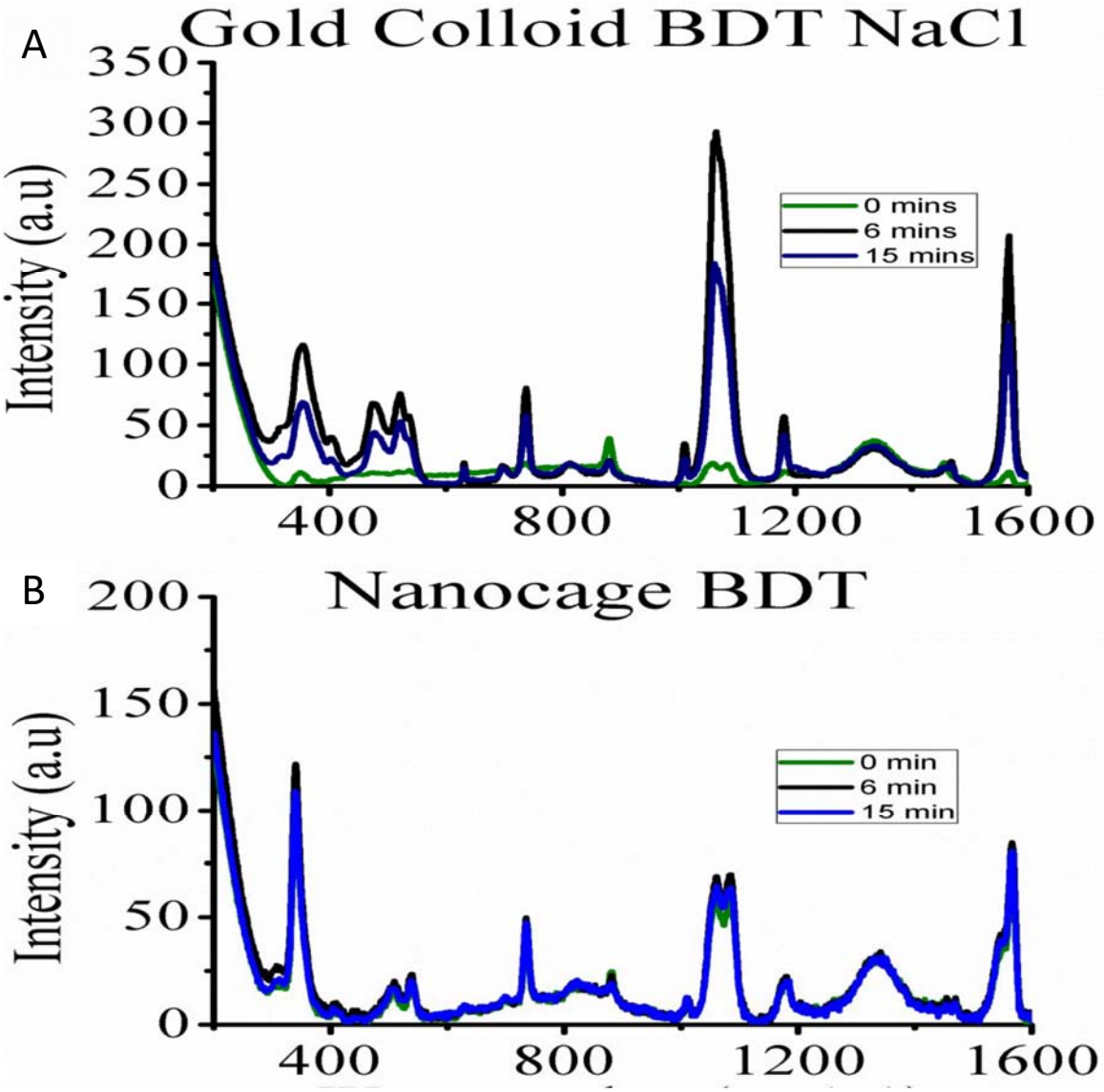

Figure 28: Gold Colloid BDT NaCl and Nanocage BDT. (a) shows SERS spectra of 147pM Gold Colloid covalently bonded to 115µM BDT with the addition of 0.5M NaCl over time (b) shows the 147pM nanocages covalently bonded to 115µM BDT over time. Reprinted with permission from B.M. Walton and G.L. Cote 2015.

No SERS signal can be detected at time zero, meaning no NaCl is present. NaCl is needed to cause aggregation to allow the shift in the extinction spectra as shown in Figure 26 and, with time, the expected BDT SERS signal peaks at 629.14 cm^{-1}, 735.20

cm^{-1}, and 1180.68 cm^{-1} begin to be seen. The peaks continue to increase in intensity over time until the signal starts to decrease due to the aggregates formed from the addition of NaCl become too large and begin to fall out of solution. The SERS spectra of nanocages bonded to 115μM BDT is shown in Figure 28. Without the NaCl, the nanocages show a signal since they are already tuned to the appropriate extinction peak and produce a relatively stable SERS signal. The aforementioned three peaks, which are independent of ethanol effects, are analyzed to help understand the SERS spectra. The three peaks monitored over time are depicted in Figure 29. For each graph, the data were normalized to the first data point. The nanocages' repeatability is easily discernable over the various time scales. In each graph, the experiments were performed three times and error bars were calculated for each data point. In comparison, the nanocages have very small error bars in comparison to the large error bars from gold. 147pM gold bonded to 115μM BDT over 15 minutes is shown in Figure 29. No SERS signals are detectable at time 0; there is no NaCl in the solution which indicates no aggregation occurs. 7μl of 0.5M NaCl is added at 2 minutes into the solution and agitated with the pipet tip for a few seconds to help mi the NaCl with the solution. SERS signals are detectable and aggregation occurs quickly. The SERS signal increasing over time is shown in Figure 29 as the aggregates formed by the introduction of NaCl continue to increase in size. The same concentration of gold, BDT, and NaCl as reported above is shown in Figure 29(b), but this time over a 60-minute time scale. Aggregates start to become too large and begin to fall out of solution after the first 15 minutes, which causes the signal to start to decrease. The same concentration of gold, BDT and NaCl is shown in Figure 29(c) over

360 minutes and illustrates how the large aggregates have fallen out of solution resulting in very low SERS intensity. 147pM of nanocages bonded with 115µM BDT is shown in Figure 29(d-f). The robustness and repeatability of the nanocages is easily displayed in comparison to the gold as the time scale changes from 15 minutes, 60 minutes, and 360 minutes, respectively. After 15 minutes, it should be noted that the signal from the nanocages does begin to decrease, likely because BDT can cause some aggregation. The gold and nanocages percentage change for each peak reported in Figure 29 are also calculated. For gold (Figure 29a), the percentage changes calculated were 36.3%, 319% and 307%, for peaks 629.14 cm^{-1}, 735.20 cm^{-1} and 1180.68 cm^{-1}, respectively. Figure 29(d) shows the same time range as Figure 29(a) for nanocages. For the nanocages, the percent change is slightly less to significantly less at 31.9%, 3.22%, 12.67% for the same three peaks respectively. For the gold, the sizeable percent changes are due to the aggregates forming and particles falling out of solution. The aggregates increase in size over time as the intensity initially increases as we theorized earlier. However, the nanocages are already tuned and do not need the addition of NaCl to see the Raman peaks. A small percentage change is seen for the nanocages. It should be noted that the gold starts to drastically fall out of solution in Figures 29(b) and (e). For peaks 629.14 cm^{-1}, 735.20 cm^{-1}, and 1180.68 cm^{-1} the percentage change is 55.8 %, 176.6 %, and 387.4 %, respectively. For the nanocages, the percent change is again less at 27.6 %, 60.8%, and 48.6%, respectively. The higher percentage change over this time period is likely indicating the nanocages are also starting to fall out of solution due to the aggregation induced by the Raman reporter BDT, although much lower than the gold.

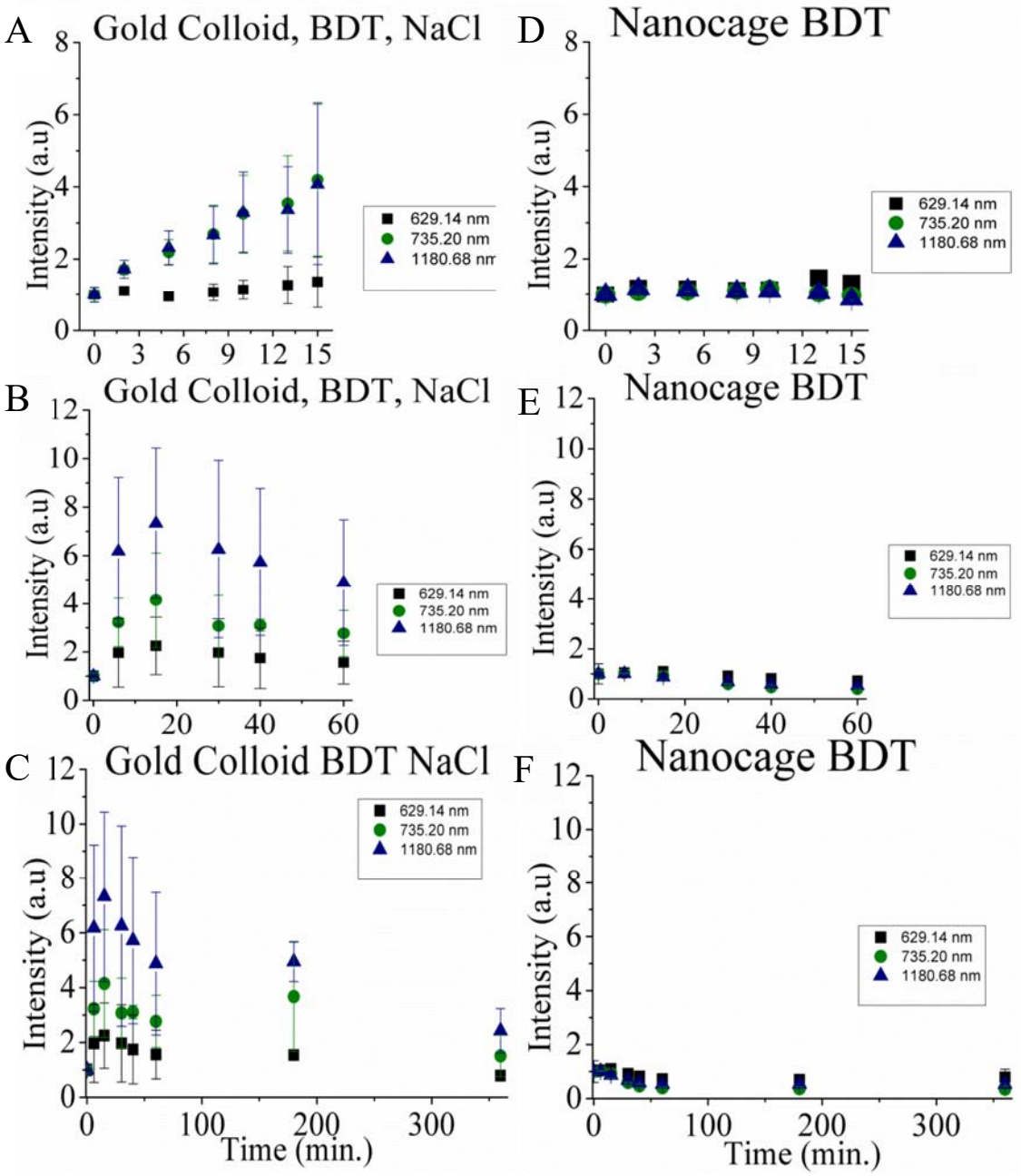

Figure 29: Gold Colloid BDT NaCl and Nanocage BDT Covalently Bonded. (a-c) shows 147pM Gold Colloid covalently bonded to 115µM BDT with 7µl of 0.5M NaCl over 15, 60, and 360 minutes (respectively) (d-f) shows147pM nanocages covalently bonded to 115µM BDT over 15, 60, and 360 minutes (respectively). Reprinted with permission from B.M. Walton and G.L. Cote 2015.

The percentage changes overall show the nanocages give better results because their SERS signal is more stable than the gold, especially in the first 15 minutes as shown in Figure 29a**.** For gold, the error bars are quite large in comparison to the nanocages because of the sporadic formation of gold aggregates.

A.8 Additional SERS experiments with various RRM

While comparing gold and nanocages, other experiments were performed to try to determine which nanoparticles should be used going forward. Additional SERS experiments were performed with other RRM including adenine and mercaptopyrridine. Initially, adenine was used to test the nanoparticles, shown in figures 30 and 31; since adenine does not have a thiol group, I looked for other RRM to test. Without the thiol group, adenine does not bond securely to the surface of the nanoparticles which makes it difficult to determine if the small SERS signal is due to the concentration of adenine used or adenine not close enough to the surface of the nanoparticles to give an enhancement. Next, mercaptopyrridine was used, which did give larger enhancements in comparison to the adenine and is probably due to the thiol group securing the molecule close enough to the surface of the nanoparticles to undergo the surface enhancement effect shown in figures 32, 33, and 34a. The last RRM I tested was BDT; this molecule was chosen due to the two thiol groups on the molecule shown in Figs. 14b and 15. At that time, I wanted to see large SERS enhancements and knew a good way was to increase the probability of the molecules binding to the surface and possible causing small aggregates due to the two thiol on opposite sides of the molecule. Below are some the Raman/SERS experiments.

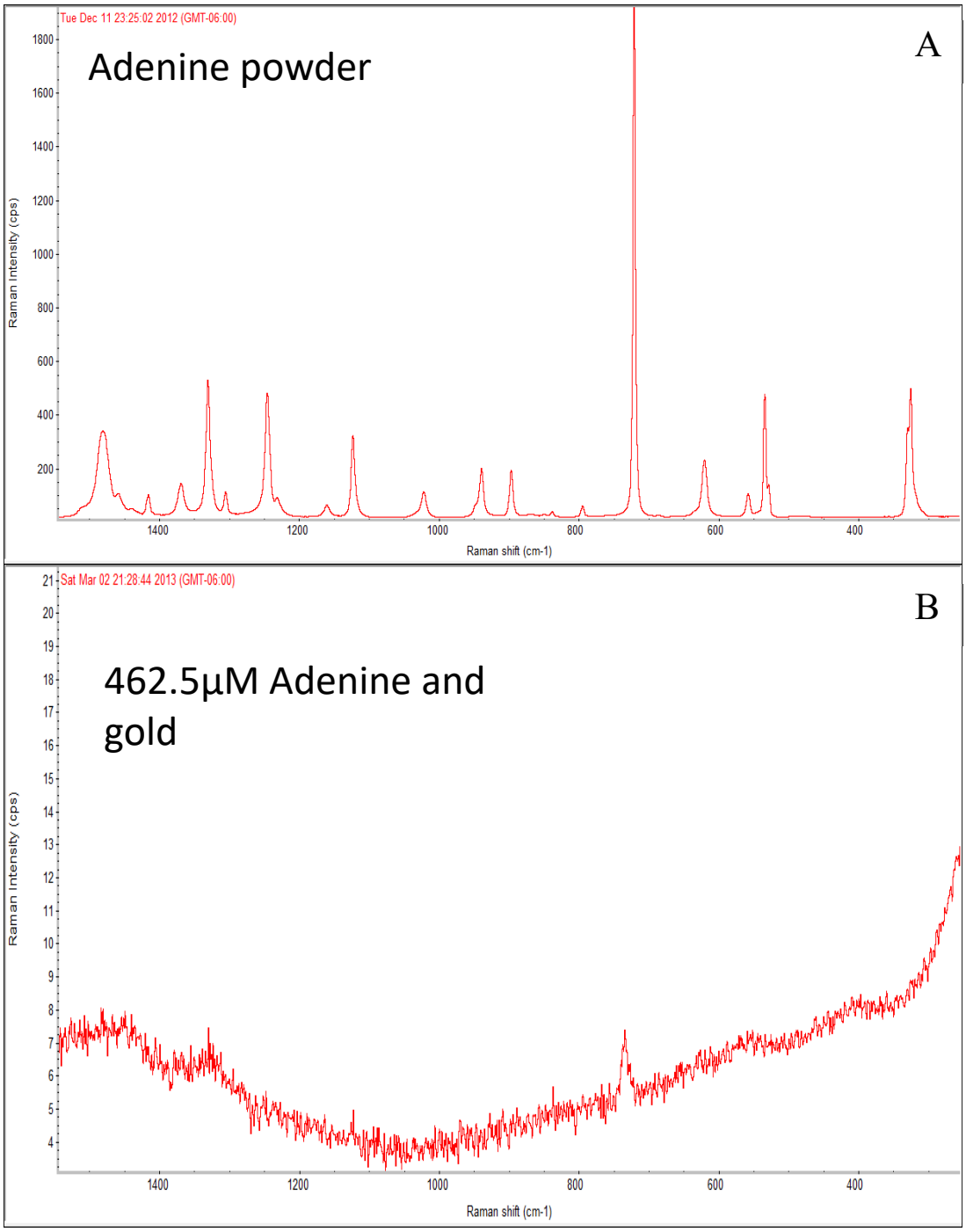

Figure 30: Spectra of Adenine Powder and SERS Spectra of Adenine and Au. a) Raman spectra of adenine powder. b) SERS spectra of 462.5µM Adenine chemsorbed to gold colloid.

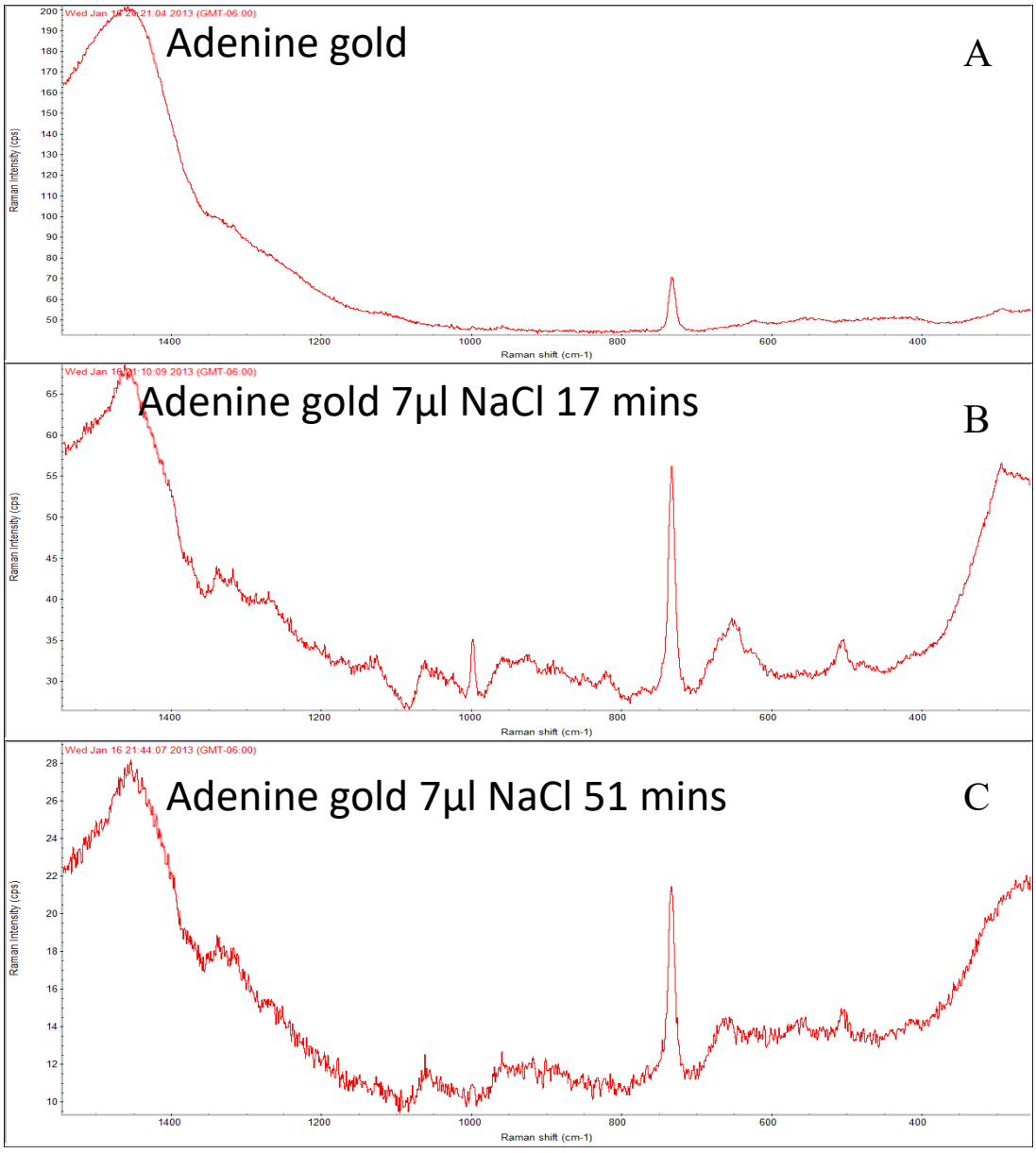

Figure 31: SERS Spectra of Adenine to Gold and NaCl. a) SERS spectra of adenine chemsorbed to gold colloid. b and c) SERS spectra of adenine with 7µl of NaCl at 17mins and 51 mins respectively

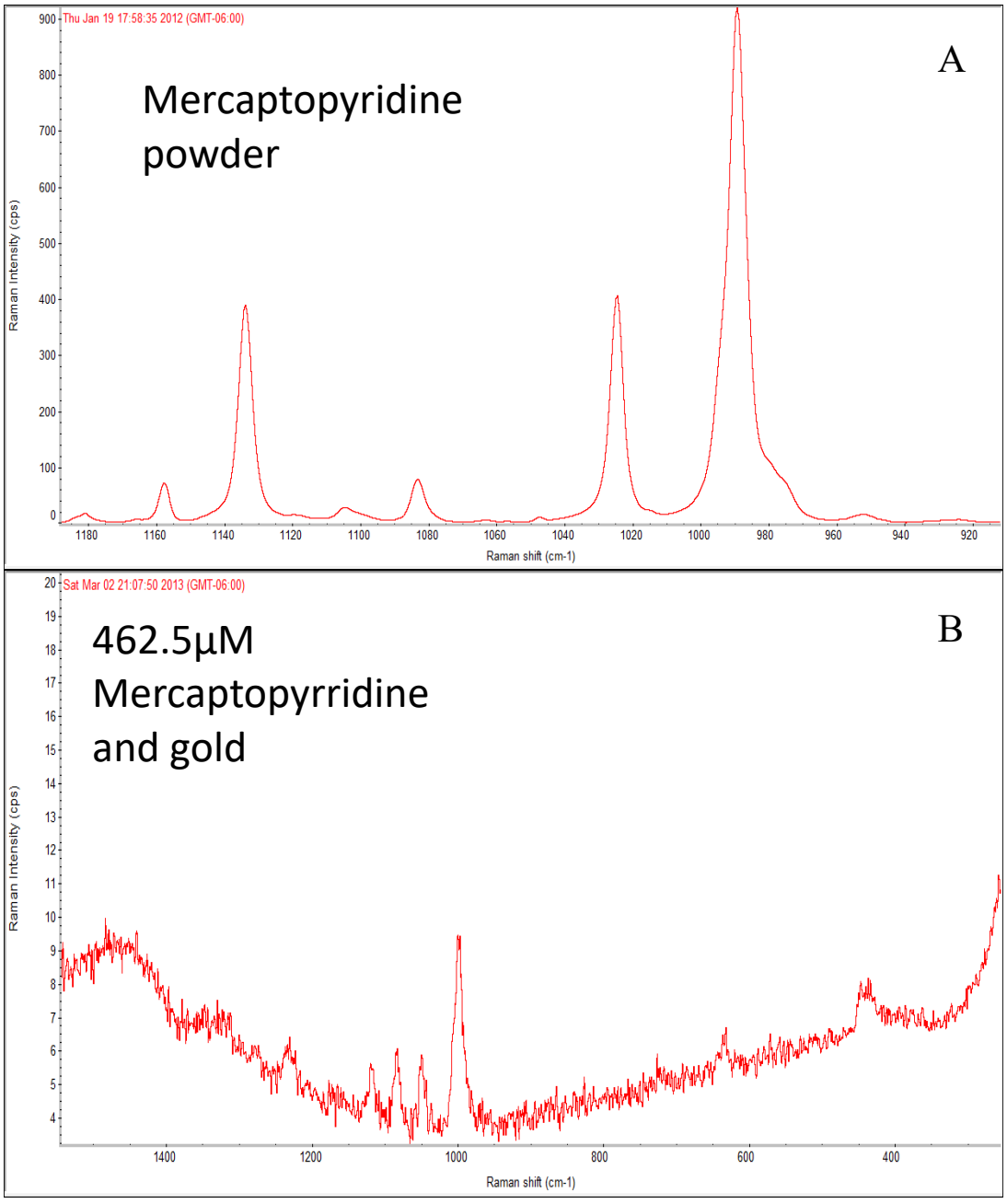

Figure 32: Raman and SERS Spectra of Mercaptopyrridine. a) Raman spectra of mercaptopyrridine powder. b) SERS spectra of 462.5µM mercaptopyrridine chemsorbed to gold colloid

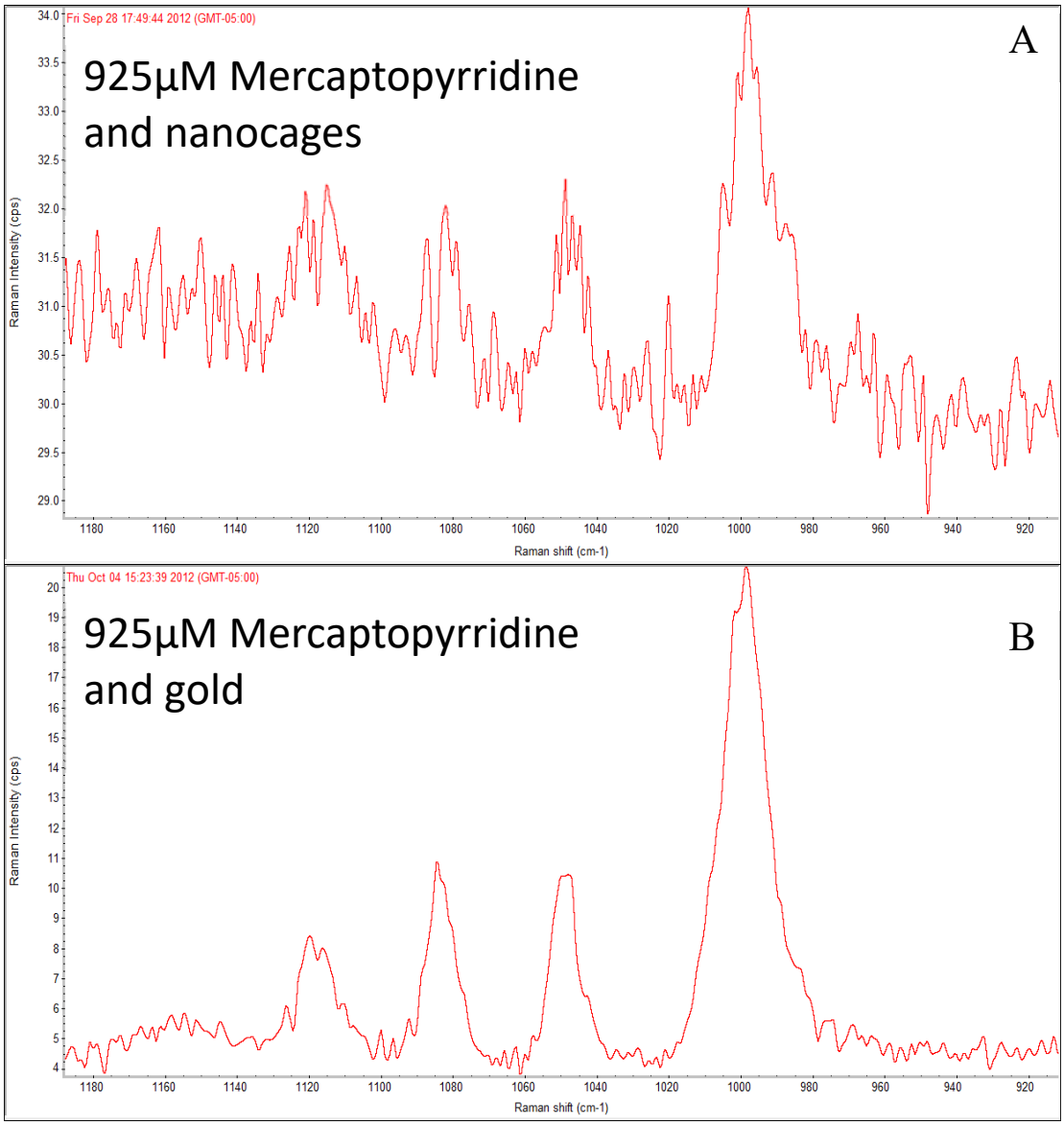

Figure 33: SERS Spectra of Mercaptopyrridine to Nanocages and Au. a and b) SERS spectra of 925µM mercaptopyrrindine chemsorbed to nanocages and gold respectively.

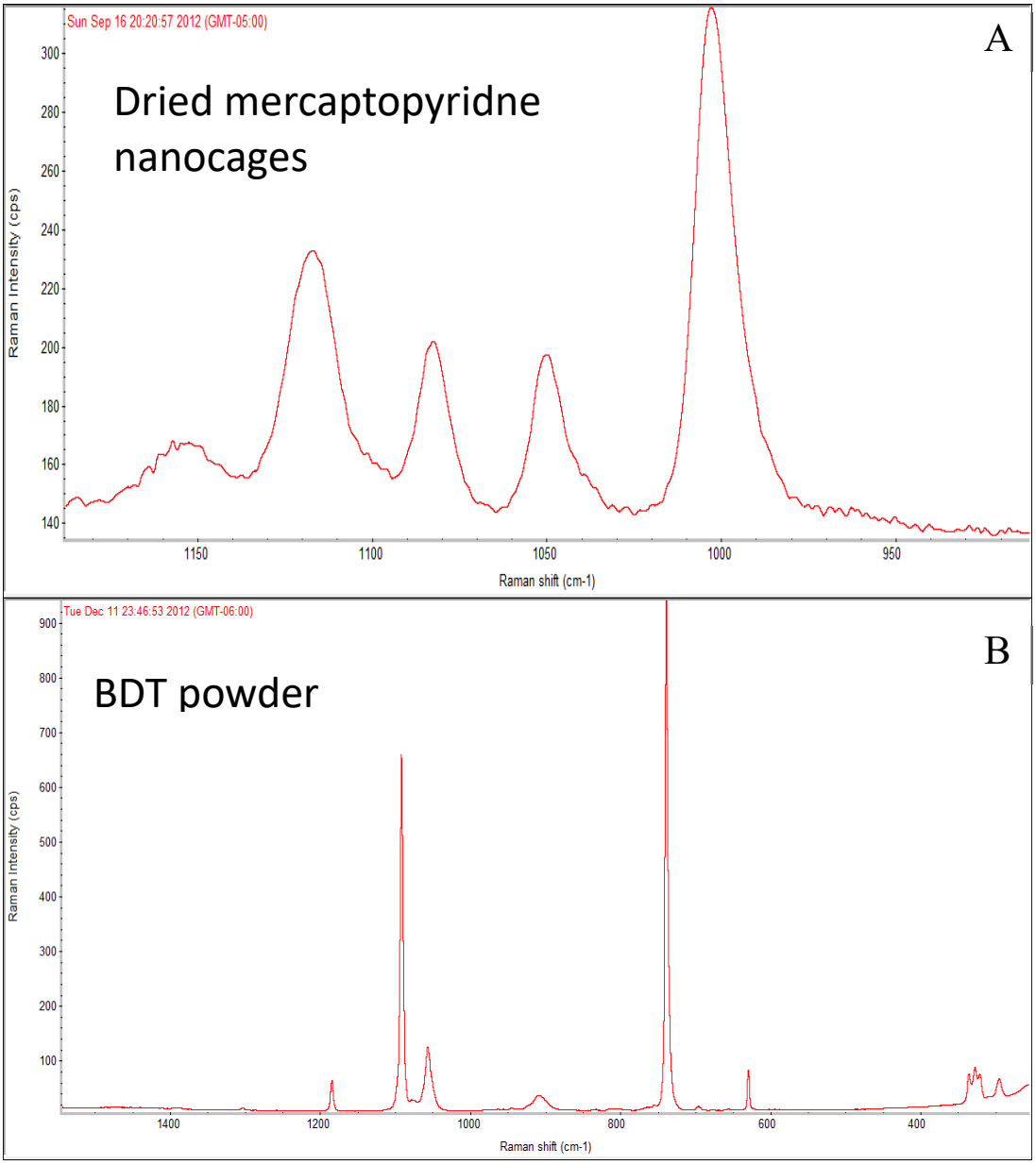

Figure 34: SERS Spectra of Dried Mercaptopyrridine to Nanocages and Raman Spectra of BDT Powder. a) SERS spectra of dried mercaptopyrridine chemsorbed to nanocages. b) Raman spectra of BDT powder

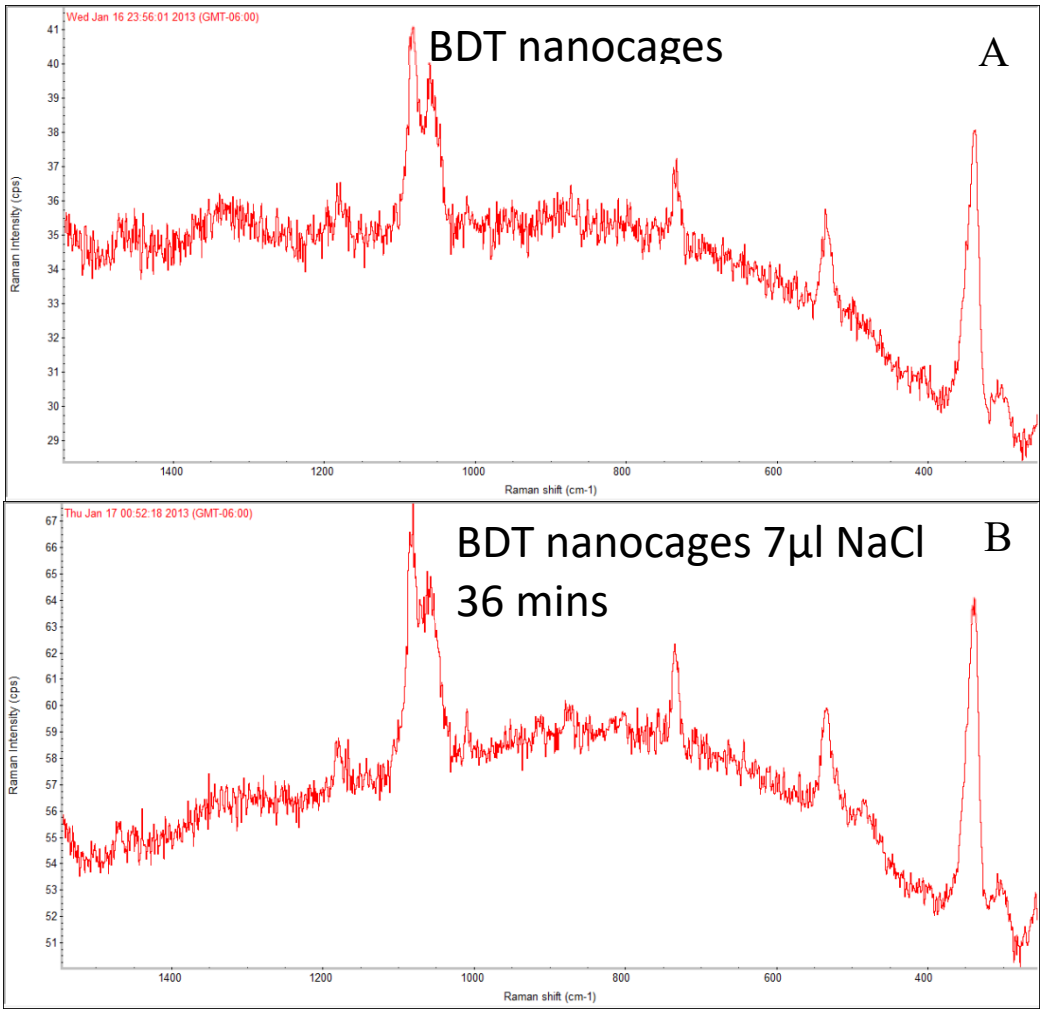

Figure 35: BDT Nanocages and Nanocages with NaCl. a) SERS spectra of BDT chemsorbed to nanocages. b) SERS spectra of BDT chemsorbed to nanocages and 7µl NaCl after 36 mins.

A.9 Concluding Thoughts from comparing Gold and Nanocage Nanoparticles for SERS

The possibility to fabricate a robust SERS spectra of a Raman reporter BDT was assessed for two substrates, nanocages and gold colloid. For gold, it is known that aggregation is required with NaCl to shift the extinction spectra to the desired NIR wavelength and produce a strong SERS signal. The system is inherently unstable as the

aggregation causes a rise and then a fall in the peaks with time as the aggregates get very large and eventually fall out of solution, although this allows for strong SERS signals. However, the nanocages, are engineered to have their extinction spectra in the NIR at 785nm and a more robust SERS signal is shown with the nanocages that is not present with the Gold. A source of error for the nanocages is eliminated by removing the need to aggregate the solution and, thus, have the potential to be more effective for a future POC sensor. Lastly, BDT is a strong Raman reporter; due to the two thiol groups, which can cause aggregation, another Raman reporter should be used to remove the aggregation effect that occurs from the Raman reporter.

APPENDIX B

MICRO-TO-NANOCHANNEL ENTRANCE WITH VARIOUS NANOPARTICLES

AND CORRESPONDING SERS SIGNALS[11] [12]

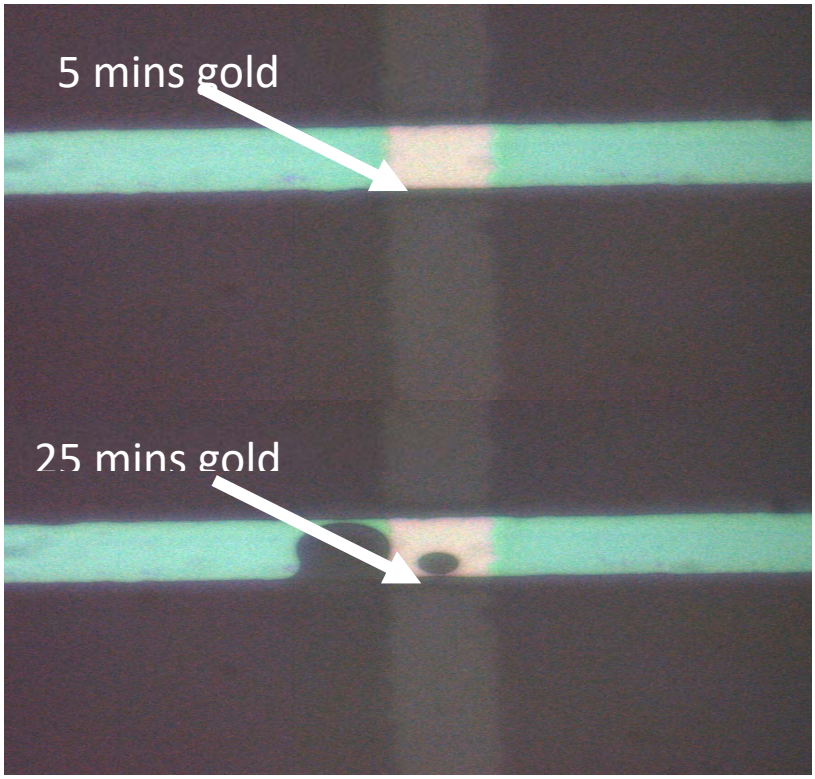

Figure 36: Au at the Entrance to Micro-to-Nanochannel. Pictures of gold at the entrance to the micro-to-nanochannel at 5mins and 25mins.

[11]Reprinted with permission from "Use of a micro-to nanochannel for the characterization of surface-enhanced Raman spectroscopy signals from unique functionalized nanoparticles" by Brian M. Walton et. al., 2016. Vol. 9715, Copyright 2016. Society of Photo Optical Instrumentation Engineers.

[12]Reprinted with permission from "Comparing Surface Enhanced Raman Spectroscopy from Colloidal Gold Nanoparticles and Nanocages" by B. M. Walton and G.L. Cote, 2015. Vol. 9332, Copyright 2015. Optical Diagnostics and Sensing XV: Toward Point-of-Care Diagnostics.

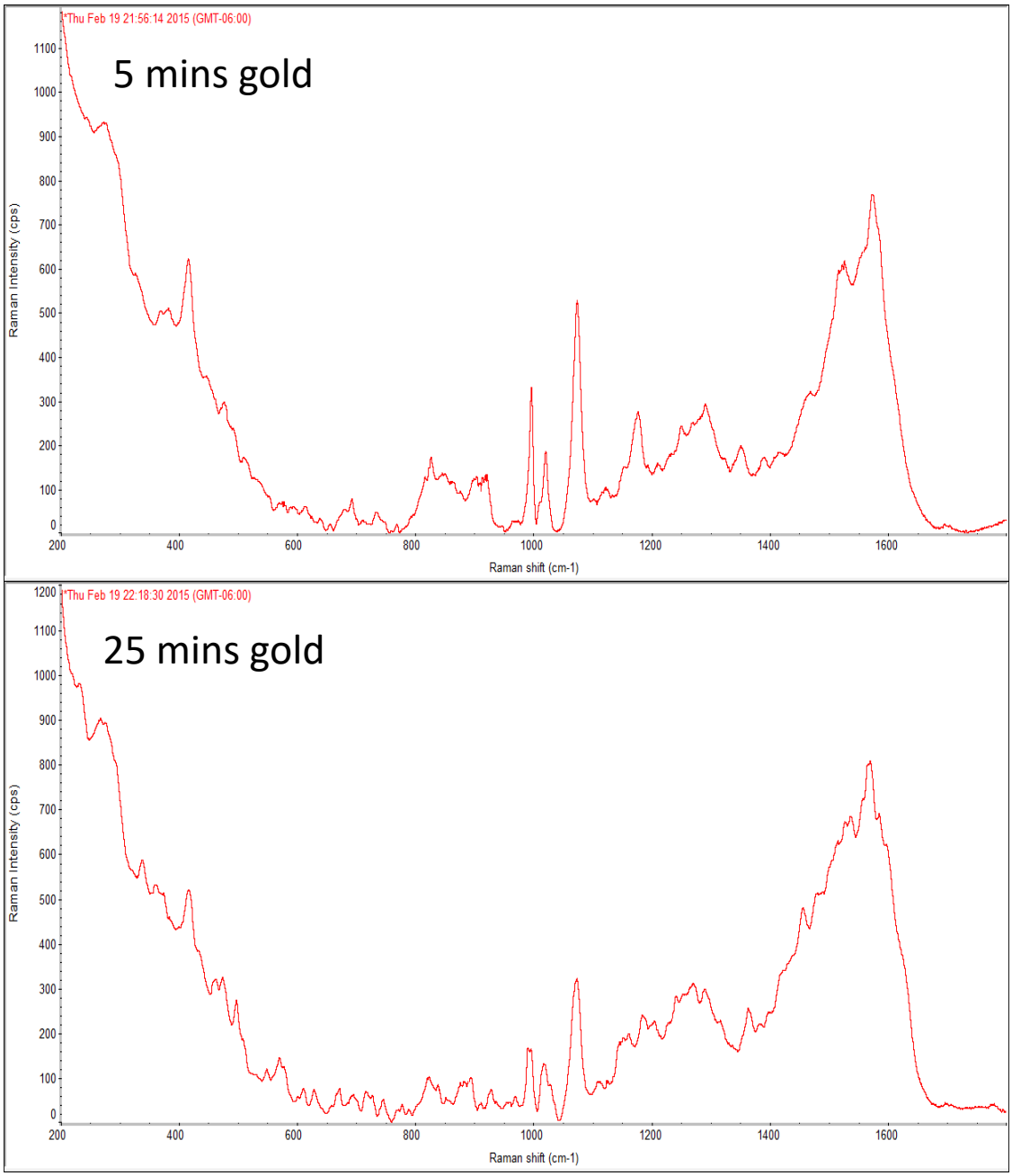

Figure 37: SERS Spectra of Gold in the Micro-to-Nanochannel. SERS spectra of gold in the micro-to-nanochannel at 5mins and 25mins

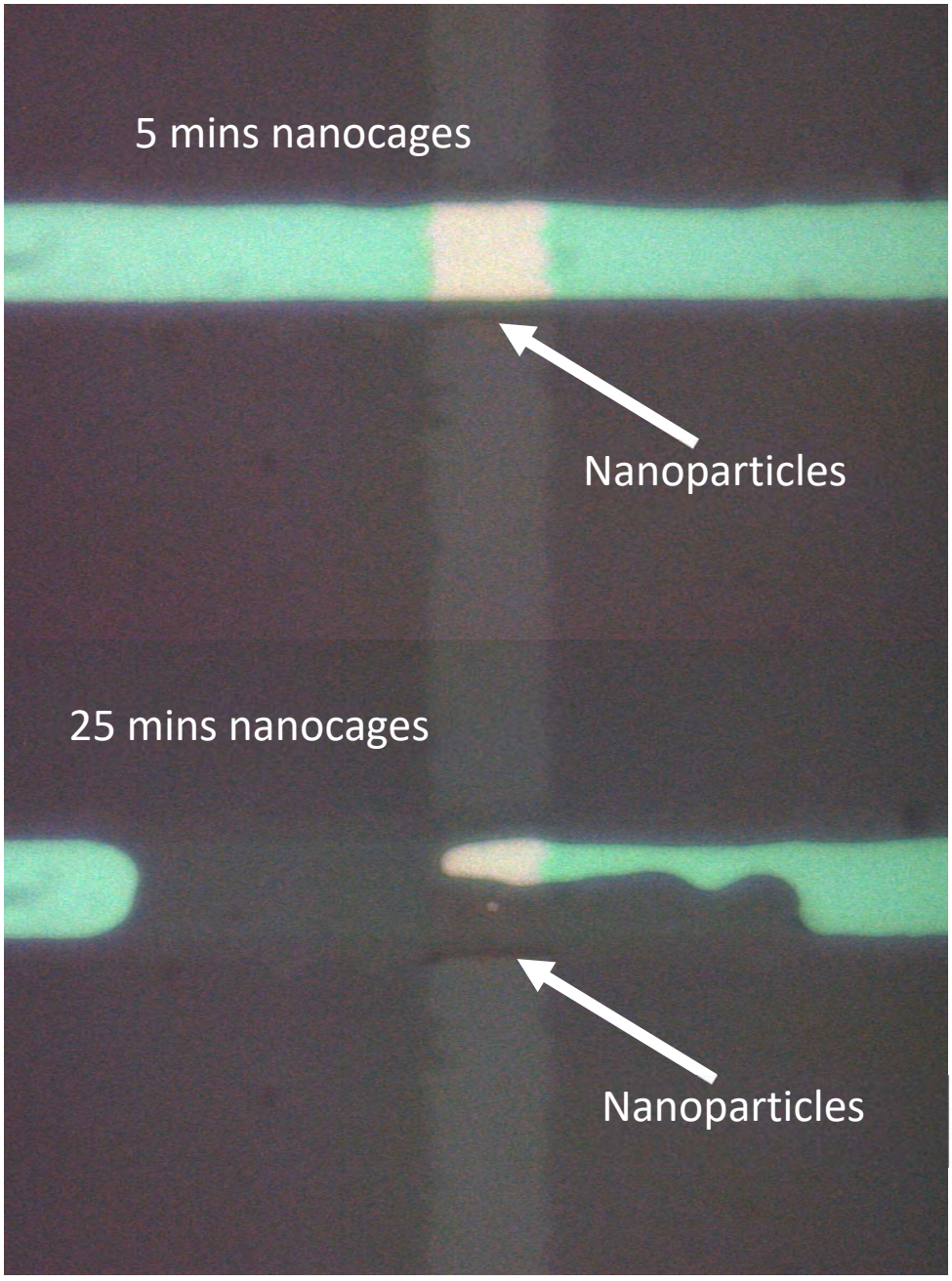

Figure 38: Nanocages at the Entrance of Micro-to-Nanochannel. Pictures of nanocages at the entrance to the micro-to-nanochannel at 5mins and 25mins. Reprinted with permission from B.M. Walton, et al. 2016.

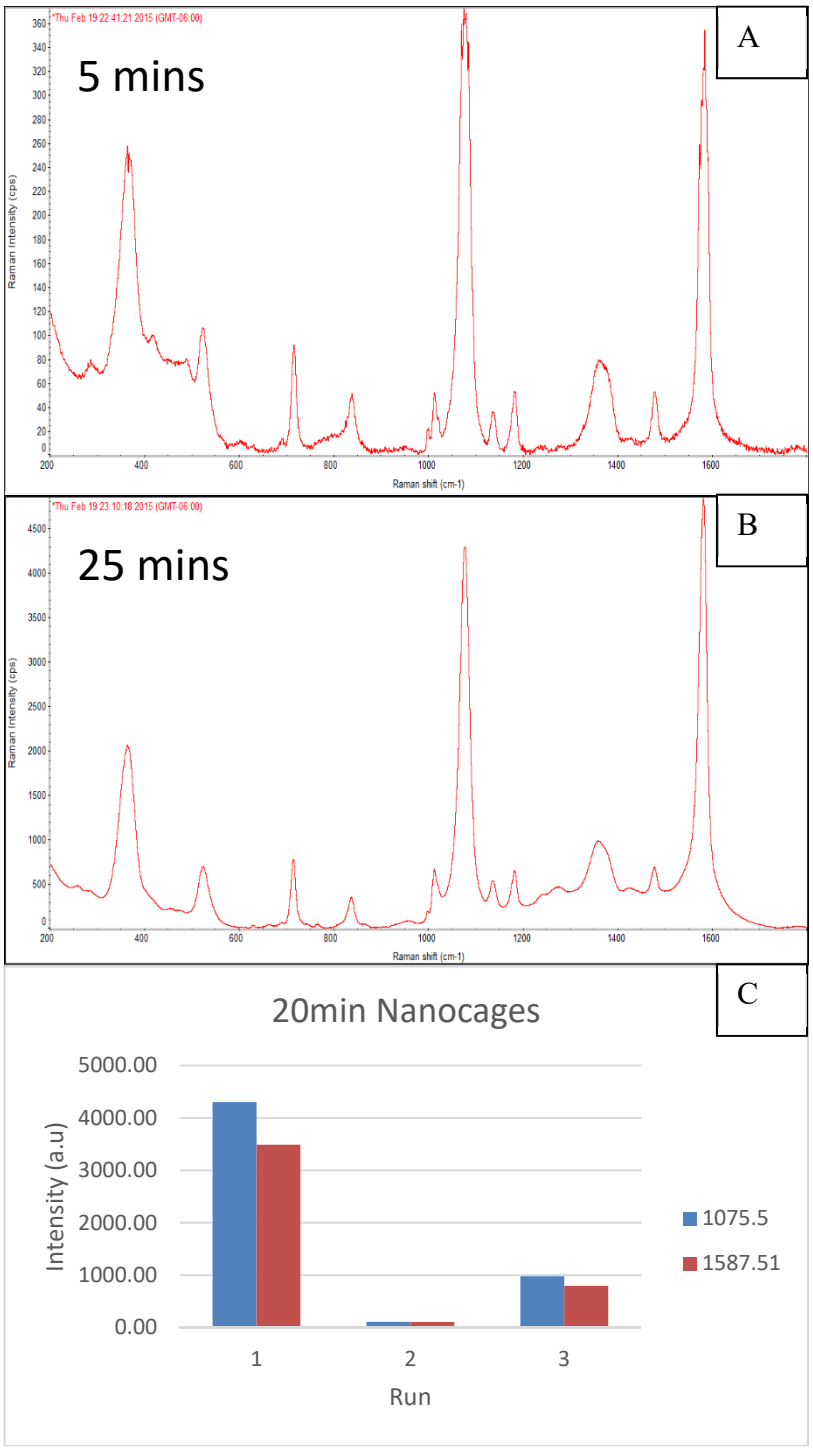

Figure 39: Nanocages in Micro-to-Nanochannel Over Time. a and b) Shows SERS spectra of nanocages in the micro-to-nanochannel at 5mins and 25mins respectively. c) Shows the 3 separate SERS scans intensities for the 2 main MBA peaks run in the micro-to-nanochannel

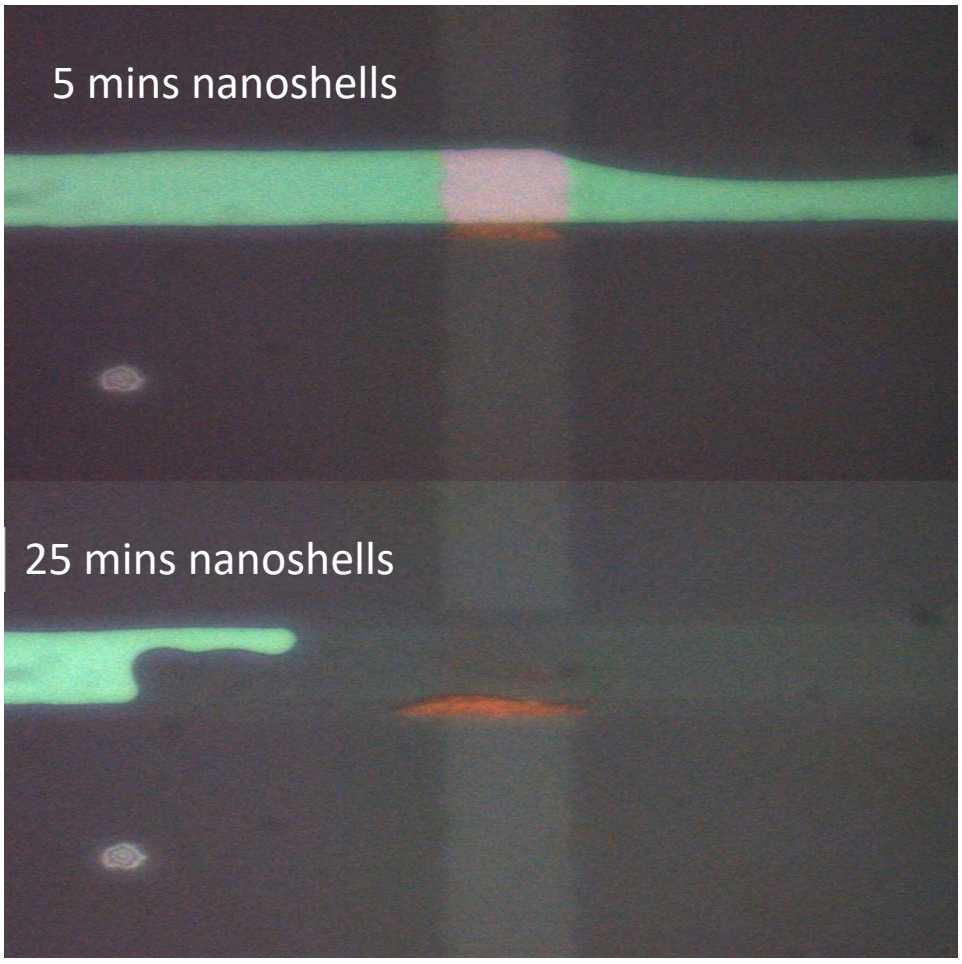

Figure 40: Nanoshells at the Entrance of Micro-to-Nanochannel Over Time. Pictures of nanoshells at the entrance to the micro-to-nanochannel at 5mins and 25mins

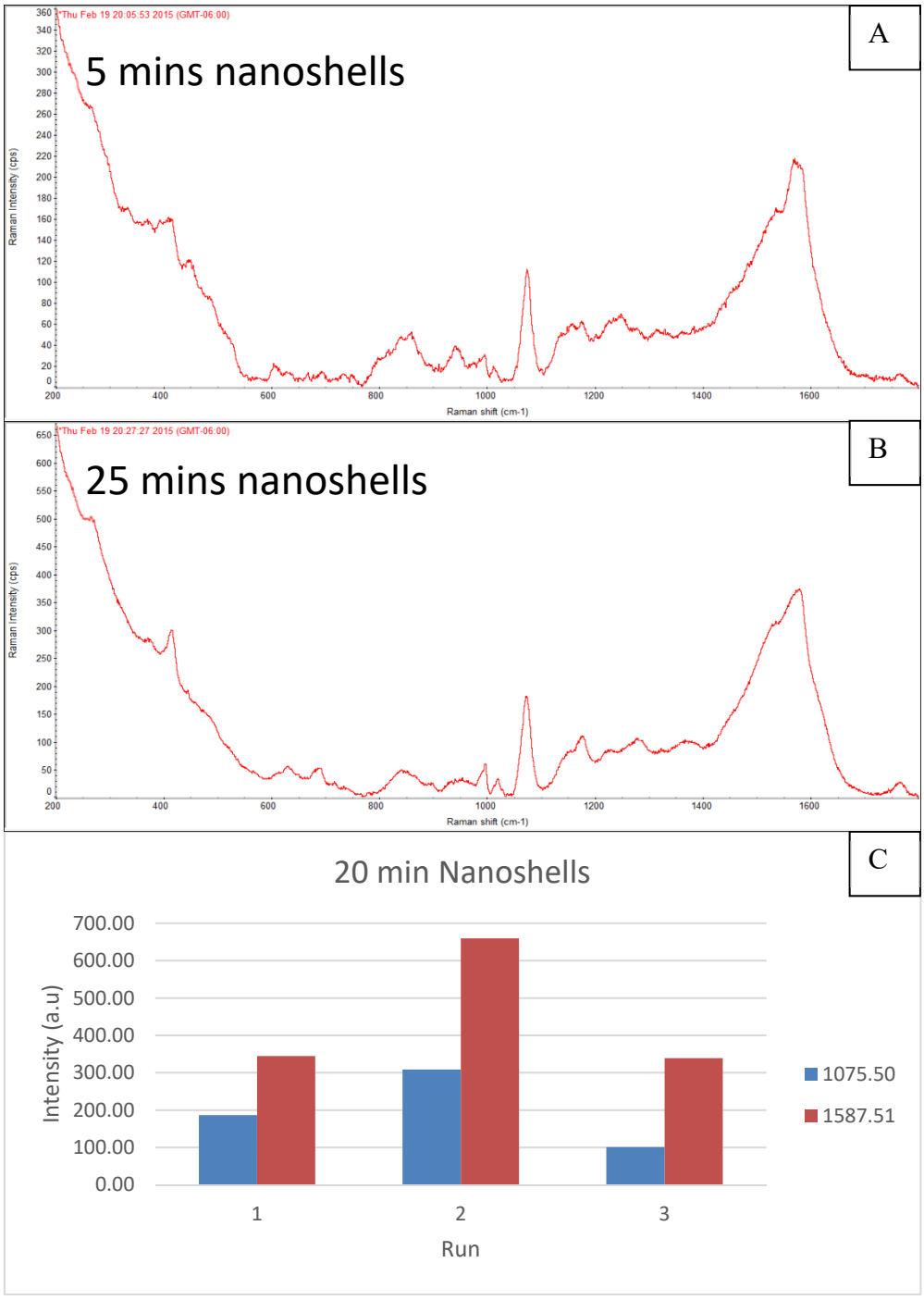

Figure 41: Nanoshells in the Micro-to-Nanochannel Over Time. a and b) Shows SERS spectra of nanoshells in the micro-to-nanochannel at 5mins and 25mins respectively. c) Shows the 3 separate SERS scans intensities for the 2 main MBA peaks run in the micro-to-nanochannel

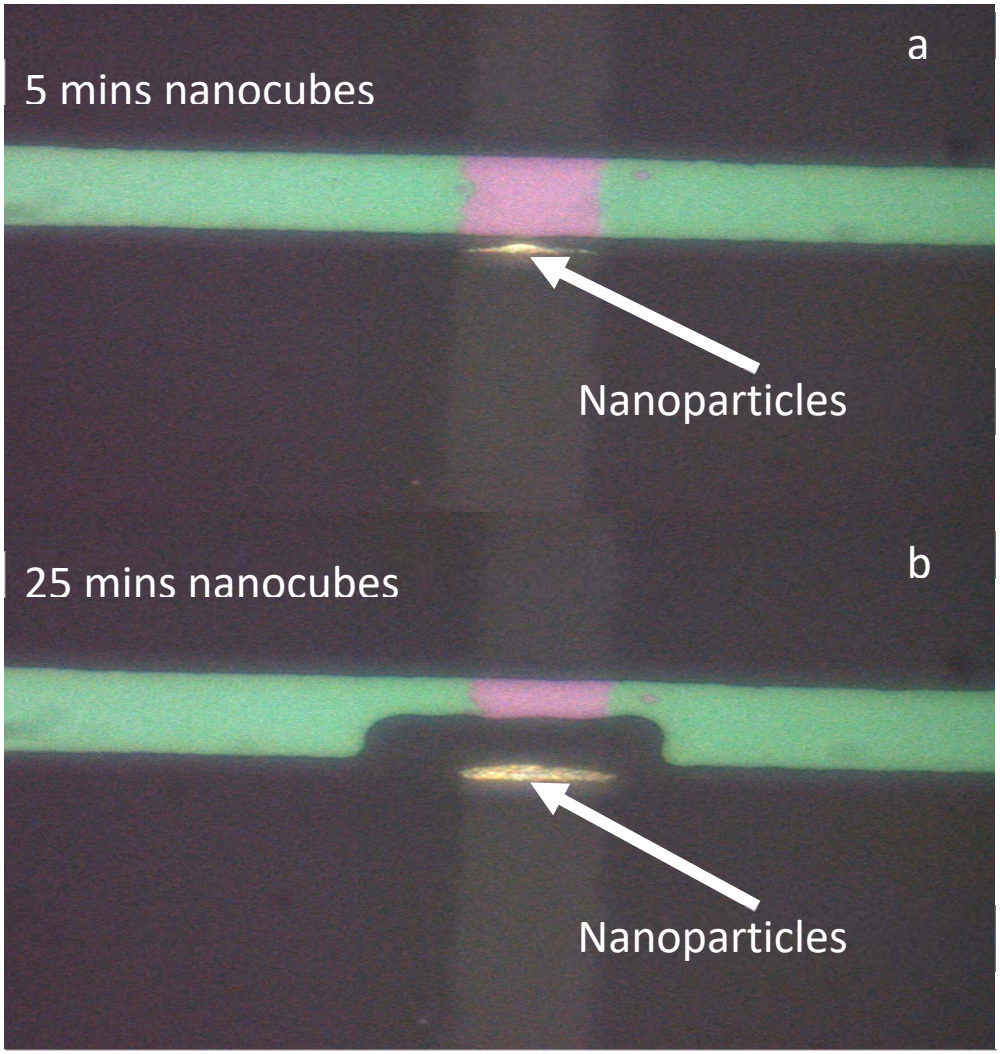

Figure 42: Nanocubes at the Entrance of Micro-to-Nanochannel Over Time. Pictures of nanocubes at the entrance to the micro-to-nanochannel at 5mins and 25mins. Reprinted with permission from B.M. Walton, et al. 2016.

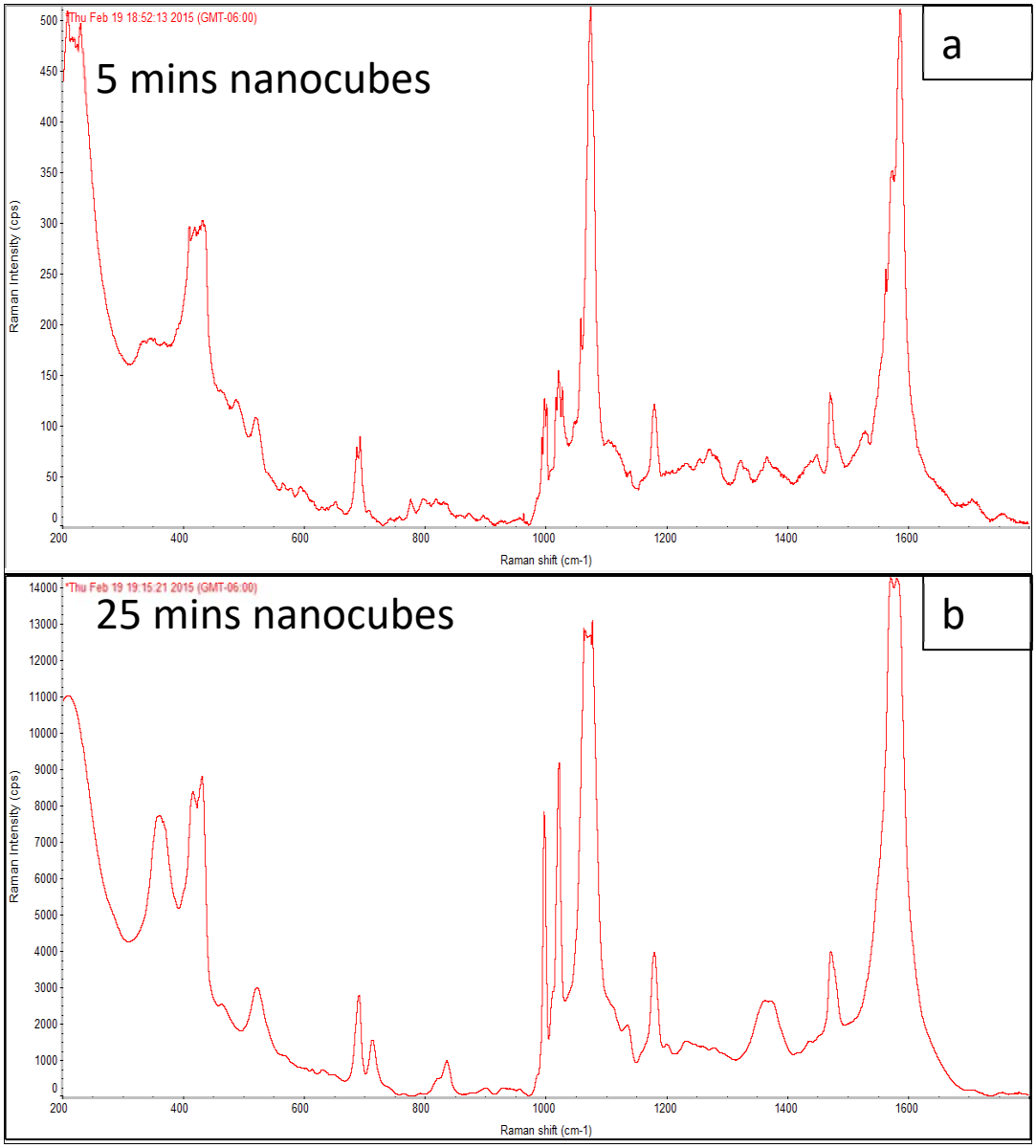

Figure 43: Nanocubes in the Micro-to-Nanochannel Over Time. a and b) Shows SERS spectra of nanocubes in the micro-to-nanochannel at 5mins and 25mins respectively.

APPENDIX C

OTHER FUNCTIONALIZATION PROTOCOLS

The other functionalization protocols are described below, except FTIR spectra were not collected except for the third protocol, which showed no amide bond formation. Protocol 2 and 4 were not selected due to lack of reproducibility after characterization analyze of the Zetasizer, UV/VIS, and nanoparticle tracking analysis (NTA). Protocol 2 involved adding MBA and PEG at the same time to the nanoparticles, then adding citrulline to bind to the PEG on the nanoparticles. Initially, the nanoparticles were centrifuged for 30 minutes, then the supernatant was taken out as in the previous protocol. The nanoparticles were then resuspended in a 1:1 ratio of ethanol mimicking the initial volume of nanoparticles. Separately, 1kda PEG was dissolved in HEPES buffer to a final concentration of 5 mM. Also, MBA was dissolved in DI water and diluted down to 22.3 μM. MBA and PEG are then mixed together both of which are at the same volume of the initial volume of the nanoparticles. The MBA/PEG solution is then slowly added to the nanoparticles using a stir plate. From the introduction of HEPES into the PEG til, the introduction of citrulline has to be done within 3 hours to minimize hydrolyze. The nanoparticles remain on the shake plate for 2 hours. Another wash step is then performed by filling the centrifuge tube with DI water and centrifuge them 30 minutes to remove any MBA/PEG not bonded to the surface of the nanoparticles. After taking out the supernatant, the nanoparticles are resuspended in HEPES buffer at 7.3 pH. A 250 mM concentration of citrulline is then added in a 1:1

ratio to the nanoparticles using a stir plate. Lastly, after waiting an hour, the functionalized nanoparticles are centrifuged for 30 minutes and then resuspended in PBS pH 7.4.

Protocol 3, which was the second most promising behind protocol 1, involves conjugating PEG with citrulline first, then binding it to the nanoparticles with MBA. To begin the process, the nanoparticles are centrifuged down for 30 minutes taking out the supernatant as with the other protocols. The nanoparticles are then resuspended in a 1:1:1 ratio of ethanol and 22.3 μM MBA solution, making sure to adjust the pH between 7.6-7.9, then wait 1 hour with the nanoparticles on a shake plate. The nanoparticles were then centrifuged again for 30 minutes and the supernatant was removed. DI water was then added and the pH was adjusted to be between 7.6-7.9. The nanoparticles then spent 24 hours on a shake plate. Following the 24 hours on the shake plate the nanoparticles are centrifuged to remove any access molecules.

APPENDIX D

MST GRAPHS OF THE INITIAL CITRULLINE APTAMERS[13] [14]

Below are the MST graphs of the initial citrulline aptamers. As seen in the below graphs, these initial aptamers were slightly more sensitive to citrulline, which is seen via their lower K_D values, but not specific enough for our purposes.

[13]Reprinted with permission from "Use of a micro-to nanochannel for the characterization of surface-enhanced Raman spectroscopy signals from unique functionalized nanoparticles" by Brian M. Walton et. al., 2016. Vol. 9715, Copyright 2016. Society of Photo Optical Instrumentation Engineers.

[14]Reprinted with permission from "Comparing Surface Enhanced Raman Spectroscopy from Colloidal Gold Nanoparticles and Nanocages" by B. M. Walton and G.L. Cote, 2015. Vol. 9332, Copyright 2015. Optical Diagnostics and Sensing XV: Toward Point-of-Care Diagnostics.

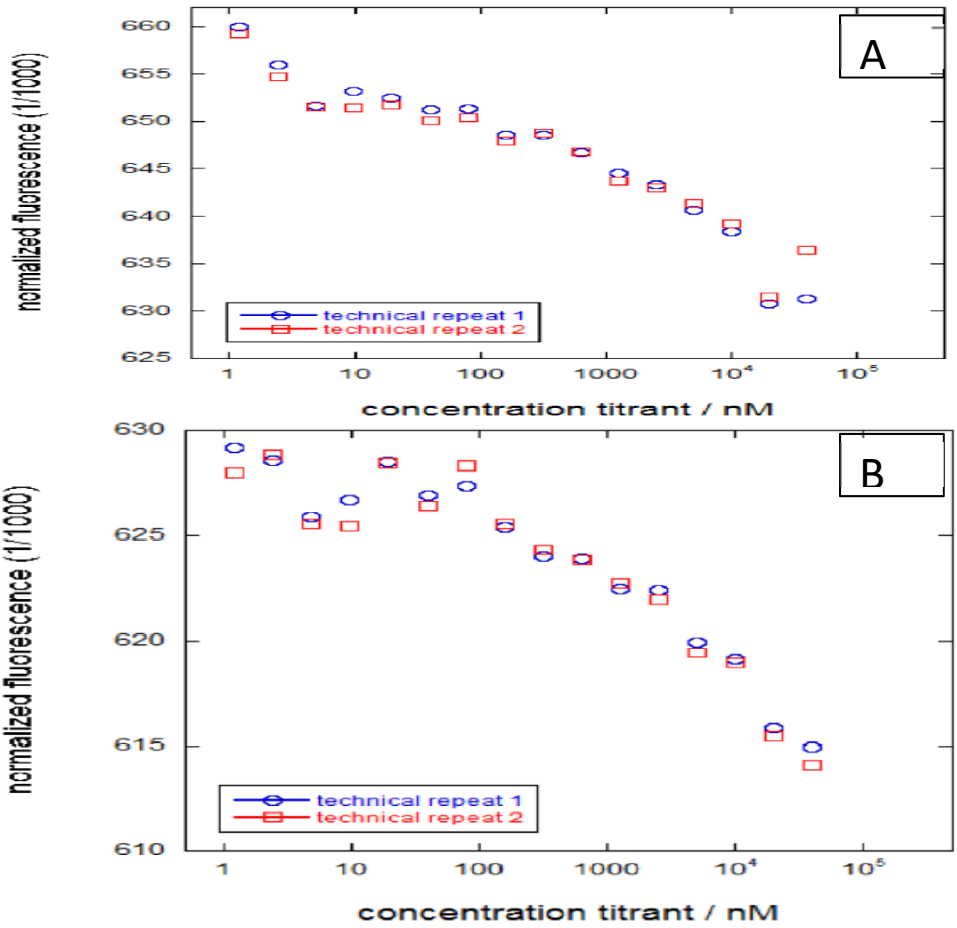

Figure 44: MST Data for Aptamers Over Time. a) Shows the MST data for first of 3 initial aptamers made for citrulline. b) Shows MST data for the second of 3 aptamers made for citrulline by basepair.

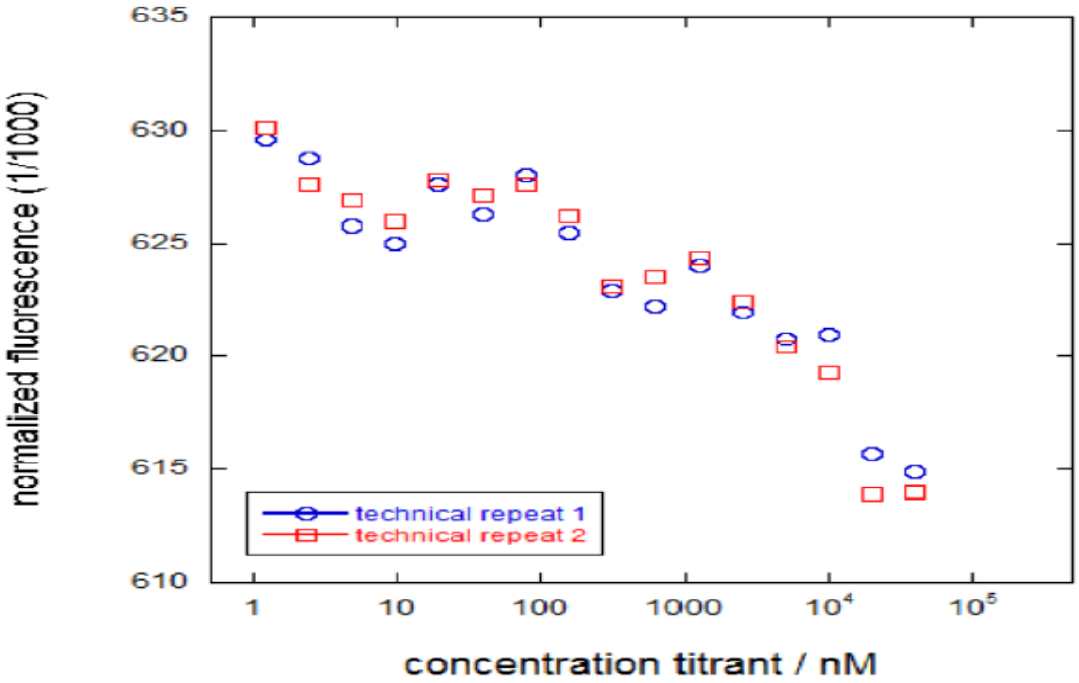

Figure 45: MST Data for Initial Third Aptamer Basepair for Citrulline. MST data for the initial third aptamer basepair made for citrulline.